Title
PV ≠ nRT: The role of the Distinct Thalamic Reticular Cell Types in Modulating Normal and Pathological Cortical Rhythms

Author
Clemente, Alexandra

Publication Date
2017

Peer reviewed|Thesis/dissertation

PV ≠ nRT: The Role of the Distinct Thalamic Reticular Cell Types in Modulating Normal and Pathological Cortical Rhythms

by

Alexandra Clemente

DISSERTATION

Submitted in partial satisfaction of the requirements for the degree of

DOCTOR OF PHILOSOPHY

in

Neuroscience

in the

GRADUATE DIVISION

of the

UNIVERSITY OF CALIFORNIA, SAN FRANCISCO

Acknowledgements

I believe in credit when and where credit is due and there are many that deserve credit for the document presented here. For specific acknowledgements on a chapter by chapter bases, please refer to the Author Contributions section in this document.

First and foremost, my family. One of my biggest sticking points with publishing my initial paper was that both my last names (my father's and mother's) be included, because both my parents deserve the credit and reward of any work conducted by my person. Even while circumstances beyond their control force them to live in a country that collapses around them, they are still the rock solid foundation I am based on. To my father who injected with me with the necessary calm and foresight that allowed me to not completely collapse. To my mother who provided that comforting support I needed to recharge and run back into the battlefield. To my other half, my twin sister, who with her characteristic feistiness suggested we just sue everyone, always my biggest advocate. My PhD is as much a testament to my work as it is of their support.

Second, my work family. It is in emergencies where camaraderie gets tested. I couldn't have done it without my Pazettes. Be it in aiding in the experiments, the writing, the editing, making sure I was not taking too many TUMS or that I had time to go to Zumba; they were there during the preparation and publishing of my first author paper. To our fearless leader, Jeanne. I am proud and thankful to be in the trenches of thalamic physiology with the best team I could've possibly imagined.

To the infrastructure and people that populate it both at the Gladstone Institutes and UCSF that made this work and things that I did outside of this work possible. To Pat and Lucita for basically being the Neuroscience program. Thank you to my thesis committee for helping both me and Jeanne as we tread through our first adventure together.

To my friends and other colleagues that had to deal with me in those months. People inside and outside of UCSF. Friends I've known for more than 20 years. The amazing group of people I do Zumba

with. Thank you for holding me up, the same way one props up a tent with sticks. Your understanding, check-ins to make sure I was ok, compassion, and patience reminds me there is so much more to my life than science. Thanks for being there to comfort me in my failures and celebrate my successes.

I would be remiss if I didn't give a special shout-out to Vikram. Thank you for feeding me, patting my head when I wanted to throw my phone across a room, literally pulling me up when I collapsed, and making sure I was covered with a blanket when I just wanted to remain collapsed. You are an honorary author of this work, even if you can't fully articulate what it is I do other than deli-slice mouse brains.

I would like to dedicate this work to four people. To my maternal grandmother, Dolores Alfonzo, who led by example and taught me that a woman can be anything she sets her mind to be. To my paternal grandmother, Georgina Rincon, an incredible example of devotion to family. To my uncle German Clemente, who taught me that kindness and compassion are the key to love and understanding. Finally, to my maternal grandfather, Ricardo Perez, who, in our last conversation days before his untimely passing, told me how excited he was to come to my thesis seminar. Thank you for sharing this journey with me.

Author Contributions

For Chapter 1: Taken from the chapter "Thalamic Models of Seizures In Vitro", from *Models of Seizures and Epilepsy*, 2nd edition, edited by Dr. Asla Pitkänen, Dr. Paul Buckmaster, Dr. Aristea S. Galanopoulou and Dr. Solomon M. Moshe. The book chapter was written in collaboration with Frances Cho, Stephanie Holden, and Jeanne T. Paz.

For Chapter 2: Conceptualization, A.C.P. and J.T.P**.; Investigation, A.C.P**., S.R.M., B.H., A.U., S.B., L.A., C.D.; **Data analysis: A.C.P,** S.R.M., B.H., F.S.C., M.W., A.U., J.T.P. **Writing – Original Draft, A.C.P.**, and J.T.P.; **Writing – Review and Editing, A.C.P.,** S.R.M., F.S.C., S.S.H., B.H., L.A. and J.T.P**., Funding Acquisition, A.C.P** and J.T.P.; Resources, L.E.F. and K.D (provided INTERSCT mice); Supervision: J.T.P. This chapter was published in Cell Reports on June 6th, 2017.

For Chapter 3: Concept Development and Experimental design: SRM and JTP; Surgeries, chronic implants and thalamic recordings: SRM, JTP; Cerebellar implants, recordings and stimulations: SRM, OR, JTP; in vivo and slice network oscillation experiments: SRM; **patch-clamp recordings: ACP**; **Data analysis:** SRM, EB, BH, **ACP**, OR, FH, BD, JTP; Histology: SRM, AC; Human EEG acquisition: MRC, MCC; Computational modeling: BD; **Writing:** SRM, **ACP**, BD, JTP. KY provided the DS mice. This chapter is in preparation for submission to a peer-reviewed journal.

For Chapter 4: Writing: ACP. Editing: JTP.

Abstract

The thalamus is usually regarded as the gateway sensory information must cross to reach the cortex, the higher cognitive processing plant of the brain. This gateway is guarded by the *nucleus Reticularis Thalami* (nRT). The nRT is a group of inhibitory neurons that through synaptic connections to the thalamic relay nuclei, temper and control the information stream from thalamus to cortex. The nRT is known to play important roles in sickness and in health. In Chapter 2, we deconstruct the nRT to its various cell types and study their role in health. Traditionally, the nRT was described as a relatively homogenous structure: containing mostly Parvalbumin (PV) expressing neurons that have Transient-type (T-type) Calcium currents that confer onto them a burst firing mode. Recent work has suggested that not all nRT neurons are created equal. There have been studies suggesting that nRT cells have different molecular, electrophysiological, and circuit properties. In other areas of the brain, many of these differences between inhibitory neurons can be correlated with expression of markers such as PV and Somatostatin (SOM). We found this to hold true in the nRT as well. PV-expressing neurons are the bursting cells that are preferentially connected to somatosensory circuits and primed to be involved in generating the physiological sleep-spindle and pathological seizure activities. SOM-expressing neurons are non-bursting cells preferentially connected to limbic circuits, and seem to be less involved in sleep-spindles and seizures. In Chapter 3, we explore the role of the nRT neurons in an animal model of a human chronic neuropsychiatric disorder. Dravet syndrome (DS) is an incurable form of childhood epilepsy associated with severe seizures, autism, sleep disorders, and sudden death. DS is brought about by a loss-of-function mutation in the sodium channel gene *SCN1A. SCN1A* is highly expressed in nRT neurons. We found that the bursting nRT neurons had prolonged post-hyperpolarization rebound bursting activity, caused by a decrease in the small conductance calcium-activated potassium (SK) current. This increased bursting in nRT neurons caused intra-thalamic circuit hyperexcitability, which may cause the epileptic events observed in these mice. Increasing SK current through the SK agonist EBIO allowed us to normalize the bursting activity in nRT cells, reduce the intra-thalamic circuit hyperexcitability, and consequentially, reduce the

seizure activity. Understanding the guardians of the gateway in sickness and in health ultimately help us understand how the brain transfers and processes information.

Table of Contents

List of Figures

List of Tables

Chapter 1 : General Introduction

The thalamus is a subcortical structure that mediates attention, perception, consciousness, and rhythm generation (Jones, 1985). The rhythmogenic properties of the thalamus, which has extensive, reciprocal connections with the cortex, emerge from the thalamocortical and intrathalamic circuits. Disruptions in these properties, or maladaptive rhythmogenesis, underlie seizures and epilepsy.

The thalamocortical loop between the thalamus and cortex is composed of reciprocally connected excitatory thalamocortical (TC) and corticothalamic (CT) pathways. Glutamatergic TC neurons of the relay nuclei have reciprocal connections with (1) glutamatergic CT neurons in functionally-related areas of the cortex, and (2) inhibitory GABAergic neurons in the *nucleus Reticularis Thalami* (nRT). The nRT also receives glutamatergic projections from the cortex (Destexhe et al., 1998; Cruikshank et al., 2010) (Figure 1). Through these connections, the thalamus generates and propagates rhythmic activity to the cortex.

Cortical and TC neurons excite nRT neurons, which leads to the inhibition of TC neurons. This is followed by post-inhibitory rebound bursts of action potentials in TC neurons (mediated by T-type Ca^{2+} channels), which in turn re-excite nRT neurons. This alternation of nRT and TC neuron bursting generates rhythmic activity of ~10 Hz spindles, which can be seen in electroencephalography (EEG) recordings of normal individuals during non-REM sleep (Huguenard and McCormick et al., 2007). These sleep spindles, one of the most well-described thalamocortical rhythms, are intermittent 10–15 Hz oscillations lasting 1–3 seconds (reviewed by Beenhakker and Huguenard, 2009). Because TC neurons can then propagate this oscillatory activity to cortical neurons, spindle activity is relatively generalized. For example, simultaneous recordings in the thalamus and cortex of cats revealed a high correlation between thalamic activity and cortical spindles (Andersen et al., 1967). Also, in vitro thalamic slice preparations can sustain robust spindle-like network activity (Jacobsen et al., 2001). These data support that the thalamus generates and propagates rhythmic activity to the cortex to mediate network oscillations associated with normal functions (e.g., sleep).

Dysfunction within the thalamocortical loop can promote aberrant network oscillations associated with epilepsy. Seizures associated with thalamocortical dysfunction are generally linked to idiopathic generalized epilepsies (IGEs) (Blumenfeld, 2003), including childhood absence epilepsy, a common IGE subtype characterized by absence seizures. However, other IGE subtypes can also include myoclonic jerks and/or generalized tonic-clonic seizures (reviewed by Crunelli and Leresche, 2002). Absence seizures seen across different IGE subtypes are characterized by a hallmark activity: synchronized ~3-10 Hz spike-wave cortical discharges (SWDs) (reviewed by Beenhakker and Huguenard, 2009 and Paz and Huguenard, 2015).

There is evidence that the circuit generating sleep spindles also underlies the generation of SWDs observed in absence seizures (Huguenard and McCormick, 2007). Indeed, the cortex and thalamus oscillate together during spindles (Andersen et al., 1967) and SWDs (Williams, 1953; Beenhakker and Huguenard, 2009), and spindles can be pharmacologically transformed into SWDs (von Krosigk et al., 1993). In addition, both sleep spindles and SWDs can be recorded in *in vitro* thalamic slices prepared from ferrets (Sanchez-Vives et al., 1997). Furthermore, mice lacking the β3 subunit of the $GABA_B$ receptor, which are prone to absence-like seizures, showed reduced intra-nRT inhibition, which promotes hypersynchrony among nRT neurons (Figure2) (Huntsman et al., 1999; Sohal et al., 2000).

These findings support the idea that sleep spindles and SWDs emerge from similar circuit mechanisms, highlighting the role of the thalamus in genetically developed epilepsies.

Based on these features, the thalamus is ideally suited to aid in the generalization of network oscillations, such as spindles—a hallmark of early stages of sleep—and seizure-like activity to other brain regions (reviewed by Beenhakker and Huguenard, 2009). However, whether the thalamus is necessary to initiate and maintain certain types of seizures, such as childhood absence seizures, remains unclear (Polack et al., 2009; Pinault et al., 1998; Pinault et al., 2003).

With recent advances and increased accessibility of genetic tools, we now have powerful methods to elucidate cellular and circuit mechanisms of epilepsy, which will be key for developing new therapeutic strategies. Here, we will focus on the potential of optogenetic tools to provide further insight into how

thalamic networks are involved in epilepsy. Indeed, recent studies identified critical "choke points," potentially outside of the site of seizure initiation, that may be specific and effective targets for anti-epilepsy treatments (reviewed by Paz and Huguenard, 2015a and 2015b). Once these synaptic and circuit components are thoroughly characterized in vitro, they can be targeted in vivo to control and prevent seizures.

The optogenetic approach relies on genetic expression of microbial opsins that can be activated by illumination to manipulate cells with spatial and temporal specificity in the brain in vitro and in vivo (reviewed by Deisseroth, 2015; Tye and Deisseroth, 2012), as well as in the spinal cord and peripheral nervous system (reviewed by Montgomery et al., 2016). A variety of opsins are available—and rapidly expanding—that can control different aspects of cellular activity or signaling. The most commonly used opsins include Channelrhodopsin 2 (ChR2), which enables researchers to elicit action potentials time-locked to light pulses, and Halorhodopsin (NpHR), a chloride pump that hyperpolarizes the membrane and inhibits firing of action potentials. These opsins can be expressed in specific cell types using viral transduction in wild-type or Cre-recombinase mouse lines. There are also transgenic mouse lines that constitutively express opsins.

Expressing opsins in specific cell types allow us to activate these cells by delivering light with an optical fiber, which requires careful consideration of temporal parameters (e.g., pulse frequency, pattern) for the question at hand (reviewed by Deisseroth, 2015; Tye and Deisseroth, 2012).

Optogenetic tools enable (1) cell- or circuit-specific targeting and (2) real-time manipulation with high spatiotemporal resolution and specificity. These tools can be well-integrated with conventional electrophysiological and pharmacological techniques, especially because they take advantage of the underlying connectivity of the target region. These features support and enhance the information we collect from slice physiology experiments (reviewed by Paz and Huguenard, 2015a and 2015b). Optogenetic tools have been widely implemented in epilepsy research (1) to locate maladaptive synaptic nodes of circuit dysfunction (Paz et al., 2011), and (2) to determine which cells can be targeted to interrupt seizures in vivo in real-time in absence epilepsy (Kros et al., 2015), temporal lobe epilepsy (Krook-Magnuson et al., 2013;

Krook-Magnuson et al., 2014), and post-stroke epilepsy (Paz et al., 2013). The general applications and limitations of closed-loop optogenetics are reviewed in (Paz and Huguenard 2015a) and (Grosenick et al., 2015).

Recent studies identified critical "choke points," potentially outside of the site of seizure initiation that may represent specific and effective targets for anti-epilepsy treatments (reviewed by Paz and Huguenard, 2015a and 2015b). Once we identify and thoroughly characterize critical synaptic and circuit components in vitro, we can target them in vivo with bioengineering and gene therapy approaches to control and prevent seizures. Thus, by elucidating the cellular and circuit mechanisms of thalamic involvement in epilepsy, particularly using in vitro approaches, we can work toward developing therapeutic strategies for this as well as other related devastating conditions.

References

Andersen, P., Andersson, S. a, & Lomo, T. (1967). Nature of thalamo-cortical relations during spontaneous barbiturate spindle activity. The Journal of Physiology, *192*(2), 283–307.

Beenhakker, M.P., and Huguenard, J.R. (2009). Neurons that Fire Together Also Conspire Together: Is Normal Sleep Circuitry Hijacked to Generate Epilepsy? Neuron *62*, 612–632.

Blumenfeld, H. (2003). From molecules to networks: cortical/subcortical interactions in the pathophysiology of idiopathic generalized epilepsy. Epilepsia, *44 Suppl 2*, 7–15.

Cruikshank, S. J., Urabe, H., Nurmikko, A. V., & Connors, B. W. (2010). Pathway-Specific Feedforward Circuits between Thalamus and Neocortex Revealed by Selective Optical Stimulation of Axons. Neuron, *65*(2), 230–245.

Crunelli, V., & Leresche, N. (2002). Childhood Absence Epilepsy: Genes, Channels, Neurons and Networks. Nature Reviews Neuroscience, *3*(5), 371–382. Deisseroth, K. (2015). Optogenetics : 10 years of microbial opsins in neuroscience. Nature Neuroscience, *18*(9), 1213–1225.

Destexhe, a, Contreras, D., & Steriade, M. (1998). Mechanisms underlying the synchronizing action of corticothalamic feedback through inhibition of thalamic relay cells. Journal of Neurophysiology, *79*(2), 999–1016.

Grosenick, L., Marshel, J. H., & Deisseroth, K. (2015). Closed-loop and activity-guided optogenetic control. Neuron, *86*(1), 106–139.

Huguenard, J. R., & McCormick, D. A. (2007). Thalamic synchrony and dynamic regulation of global forebrain oscillations. Trends in Neurosciences, *30*(7), 350–356.

Huntsman, M.M., Porcello, D.M., Homanics, G.E., DeLorey, T.M., and Huguenard, J.R. (1999). Reciprocal Inhibitory Connections and Network Synchrony in the Mammalian Thalamus. Science *283*, 541.

Jacobsen, R. B., Ulrich, D., & Huguenard, J. R. (2001). GABA(B) and NMDA receptors contribute to spindle-like oscillations in rat thalamus in vitro. Journal of Neurophysiology, *86*(3), 1365–1375.

Jones, E. G. (1985). The Thalamus, 935.

Krook-Magnuson, E., Armstrong, C., Oijala, M., & Soltesz, I. (2013). On-demand optogenetic control of spontaneous seizures in temporal lobe epilepsy. Nature Communications, *4*,

Krook-Magnuson, E., Szabo, G. G., Armstrong, C., Oijala, M., & Soltesz, I. (2014). Cerebellar Directed Optogenetic Intervention Inhibits Spontaneous Hippocampal Seizures in a Mouse Model of Temporal Lobe Epilepsy 1 , 2. eNeuro, *1*(1).

Kros, L., Rooda, O. H. J. E., Spanke, J. K., Alva, P., Dongen, M. N. Van, Karapatis, A., … Hoebeek, F. E. (2015). Cerebellar Output Controls Generalized Spike-and-Wave Discharge Occurrence. Annals of Neurology, *77*(6), 1027–1049.

Montgomery, K. L., Iyer, S. M., Christensen, A. J., Deisseroth, K., & Delp, S. L. (2016). Beyond the brain : Optogenetic control in the spinal cord and peripheral nervous system. Science Translational Medicine, *8*(337).

Paz, J. T., & Huguenard, J. R. (2015). Optogenetics and epilepsy: Past, present and future. Epilepsy Currents, *15*(1), 34–38.

Paz, J.T., and Huguenard, J.R. (2015). Microcircuits and their interactions in epilepsy: is the focus out of focus? Nat Neurosci *18*, 351–359.

Paz, J.T., Davidson, T., Freschette, E., Delord, B., Prada, I., Peng, K., Deisseroth, K., and Huguenard, J.R. (2013). Closed-loop optogenetic control of thalamus as a new tool to interrupt seizures after cortical injury. Nat. Neurosci. *16*, 64–70.

Pinault, D., and Descheˆnes, M. (1998). Projection and Innervation Patterns of Individual Thalamic Reticular Axons in the Thalamus of the Adult Rat: A Three-dimensional, Graphic, and Morphometric Analysis. J. Comp. Neurol. *2*, 180–203.

Pinault, D. (2003). Cellular interactions in the rat somatosensory thalamocortical system during normal and epileptic 5-9 Hz oscillations. The Journal of Physiology, *552*(Pt 3), 881–905.

Polack, P. O., Mahon, S., Chavez, M., & Charpier, S. (2009). Inactivation of the somatosensory cortex prevents paroxysmal oscillations in cortical and related thalamic neurons in a genetic model of absence epilepsy. Cerebral Cortex, *19*(9), 2078–2091.

Sanchez-Vives, M. V., & McCormick, D. A. (1997). Functional properties of perigeniculate inhibition of dorsal lateral geniculate nucleus thalamocortical neurons in vitro. The Journal of Neuroscience : The Official Journal of the Society for Neuroscience, *17*(22), 8880–8893.

Sohal, V.S., Huntsman, M.M., and Huguenard, J.R. (2000). Reciprocal Inhibitory Connections Regulate the Spatiotemporal Properties of Intrathalamic Oscillations. J. Neurosci. *20*, 1735

Sohal, V.S., and Huguenard, J.R. (2003). Inhibitory Interconnections Control Burst Pattern and Emergent Network Synchrony in Reticular Thalamus. J. Neurosci. *23*, 8978.

Tye, K. M., & Deisseroth, K. (2012). Optogenetic investigation of neural circuits underlying brain disease in animal models. Nature Reviews Neuroscience, *13*(4), 251–266.

von Krosigk, M., Bal, T., & McCormick, D. a. (1993). Cellular mechanisms of a synchronized oscillation in the thalamus. Science (New York, N.Y.), *261*(5119), 361–364.

Williams, D. (1953). A Study of Thalamic and Cortical Rhythms in Petit Mal. Brain, *76*(1947), 50–69

Figures

CT: corticothalamic cells
TC: thalamocortical cells

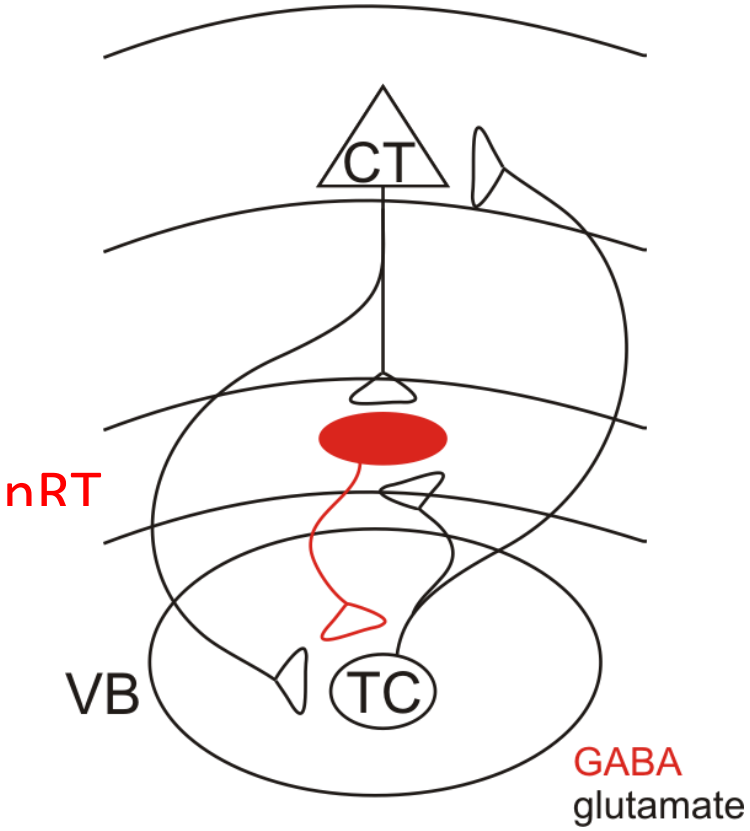

nRT: reticular thalamus
VB: ventrobasal thalamus
VB = VPL + VPM

Figure 1.1.Diagram of the thalamocortical circuit

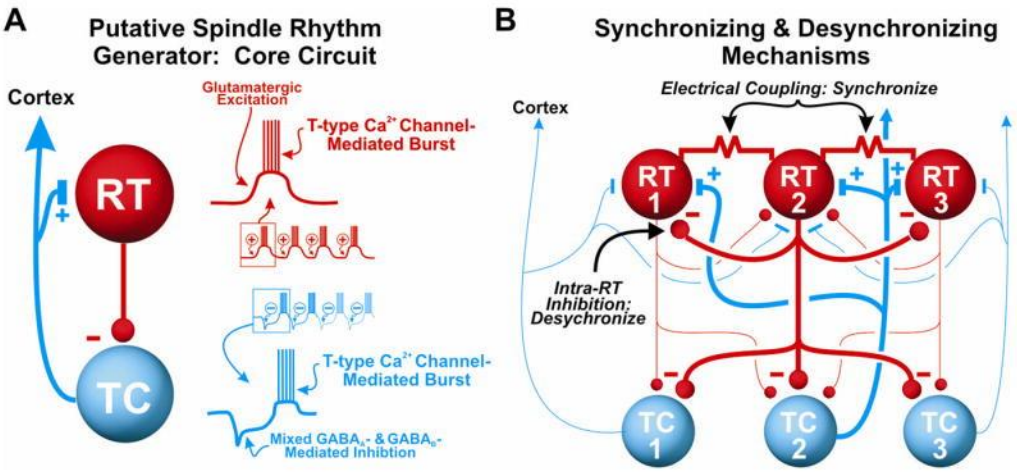

Figure 1.2. Schematic representation of nRT-TC circuitry present in thalamic brain slices. Adapted from Beenhakker and Huguenard, Neuron 2009

A) Putative spindle generator. *Anatomy* **(left)**. Shown is one pair of reciprocally-connected TC and reticular thalamic (RT) neurons. RT neurons are GABAergic and inhibit TC neurons via $GABA_A$ and $GABA_B$ postsynaptic receptors. TC neurons are glutamatergic and excite nRT neurons (and cortical neurons). Not shown are the corticothalamic inputs to that are proposed to activate spindle rhythm generator. *Oscillations* **(right)**. Following nRT-mediated inhibition, TC neurons generate post-inhibitory rebound action potential bursts. These TC burst are responsible for recurrent excitation of RT neurons and activation of the subsequent cycle of the oscillation. Both RT and TC bursting activity is mediated by T-type Ca^{2+} channel activity. Plus signs (+) refer to glutamatergic excitation while minus signs (-) refer to GABAergic inhibition.

B) Mechanisms that contribute to the synchronization and desynchronization of nRT neuron activity. Electrical coupling among RT neurons is hypothesized to synchronize their activity. RT-to-RT neuron inhibition (i.e. *intra-RT inhibition*) is proposed to desynchronize RT neuron activity through a burst-shunting mechanism (Sohal and Huguenard, 2003). For example, if RT_2 fires slightly before RT_1 & RT_3, then RT_1 & RT_3 will not fire bursts of activity. Moreover, if the inhibition is sufficiently strong, then recurrent excitation by TC neurons will be ineffective at triggering a subsequent burst

in RT_1 & RT_3. Also shown is the convergence/divergence of RT-to-TC and TC-to-RT connectivity. Line thickness/synapse size does not represent functional difference in connection strength.

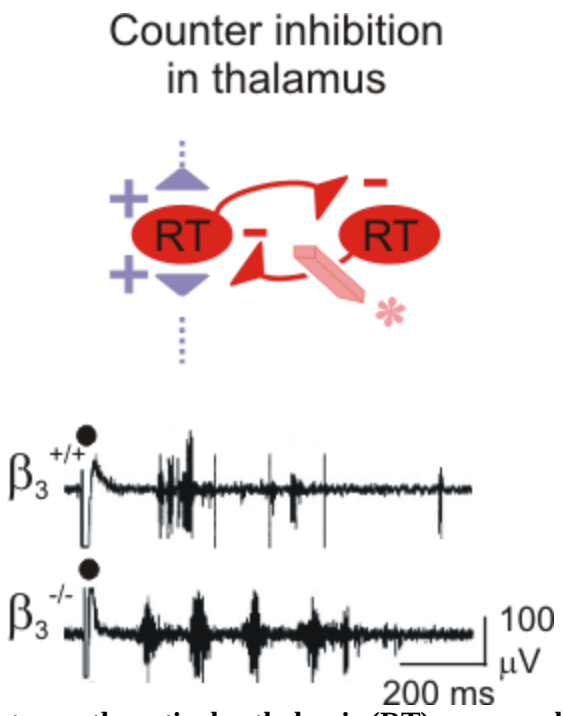

Figure 1.3. Inhibition between the reticular thalamic (RT) neurons desynchronizes thalamic network oscillations. Adapted from Paz and Huguenard, 2015.

Loss of RT-RT counter-inhibition (eraser*) in a $\beta3^{-/-}$ mouse enhances intra-thalamic network synchrony measured with multiunit recordings in thalamic slices.

Chapter 2 : Distinct thalamic reticular cell types differentially modulate normal and pathological cortical rhythms

Summary

Integrative brain functions depend on widely distributed, rhythmically coordinated computations. Through its long-ranging connections with cortex and most senses, the thalamus orchestrates the flow of cognitive and sensory information. Essential in this process, the *nucleus Reticularis Thalami* (nRT) gates different information streams through its extensive inhibition onto other thalamic nuclei; however, we lack an understanding of how different inhibitory neuron subpopulations in nRT function as gatekeepers. We dissociated the connectivity, physiology, and circuit functions of neurons within rodent nRT, based on parvalbumin (PV) and somatostatin (SOM) expression, and validated the existence of such populations in human nRT. We found that PV but not SOM cells are rhythmogenic, and that PV and SOM neurons are connected to and modulate distinct thalamocortical circuits. Notably, PV but not SOM neurons modulate somatosensory behavior and disrupt seizures. These results provide a conceptual framework for how nRT may gate incoming information to modulate brain-wide rhythms.

Introduction

The nucleus reticularis thalami (nRT) is the "guardian of the gateway" in the thalamocortical circuit, given its role in modulating interactions between the cerebral cortex and thalamus (Crick, 1984; Halassa and Acsády, 2016). The nRT modulates thalamocortical oscillations that underlie functions like such as attention, sensation, sleep, and consciousness (Calabrò et al., 2015; Crick, 1984; Steriade, 2005). Disruptions in this circuit correlate with neurological (Paz et al., 2010; Slaght et al., 2002) and psychiatric disorders (Ferrarelli and Tononi, 2011; Zhang et al., 2010).

The nRT contains inhibitory neurons that release gamma-aminobutyric acid (GABA). It is the main source of inhibition for the excitatory relay thalamus in rodents (Gentet and Ulrich, 2003; Houser et al., 1980). The nRT has been thought to include mainly parvalbumin-expressing neurons (PV) (Csillik et al., 2005; Hou et al., 2016; Jones and Hendry, 1989) but somatostatin-positive cells (SOM) were recently found in rodent nRT (Ahrens et al., 2015; Wells et al., 2016). These cells have not been detailed in humans. PV and SOM neurons have distinct functions in the cortex and hippocampus (reviewed by Kim et al., 2016), while little is known about whether they mediate different functions of the nRT. Further, the existence of functionally distinct neuron types within the nRT has been suggested (Halassa et al., 2014; Lee et al., 2007) but not associated with molecular markers.

nRT neurons can orchestrate brain-wide network activity (Crick, 1984; Halassa and Acsády, 2016). Brief optogenetic stimulation of nRT neurons *in vivo* induces spindles in the cortex during non-rapid eye movement sleep (Halassa et al., 2011), while sustained stimulation increases delta band power similar to slow-wave sleep (Lewis et al., 2015). Variations in anatomical connections between nRT and thalamic relay cells differentially modulate cortical oscillatory activity and attention (Halassa et al., 2014; Macdonald et al., 1998), but it remains unknown whether these different functions are mediated by cellular substrates that can be distinguished by molecular markers.

Because the nRT does not project directly back onto the cortex, nRT modulation of specific cortical regions depends on its topographical organization and connections with thalamic relay nuclei (Crabtree,

1992; Lam and Sherman, 2011). However, it remains unknown whether the different cell types in the nRT (i.e. PV and SOM cells) project to distinct thalamocortical relay nuclei to produce different functions *in vivo*.

We hypothesize that the nRT's multiple functions are mediated by PV and SOM neurons that are anatomically connected to different circuits. Here, we deconstruct nRT PV and SOM neuron populations by assessing their intrinsic electric and synaptic membrane properties, pre- and post-synaptic connectivity, and functions within the thalamocortical circuit during normal and pathological behaviors.

Results

PV and SOM Neurons Segregate Differentially within the nRT

We evaluated the location of PV and SOM neurons across the anterior-posterior (Figure 1A), medial-lateral, and dorsal-ventral axes of the nRT (Figure 1B) with genetic and immunohistochemical approaches. For validation of specificity and selectivity of Cre lines, see Supplemental Methods and Figure 8. PV and SOM cells were located across the entire anterior-posterior axis of the nRT. High-resolution confocal images distinguished singly labeled PV and SOM cells within the somatosensory nRT (Figures 1C–D), identifying a previously undescribed population of SOM neurons in the nRT that do not express PV. We divided the somatosensory nRT into tiers based on their projection patterns onto thalamic relay nuclei as described by (Lam and Sherman, 2011; Pinault and Descheˆnes, 1998) (Figure 1B & E). The distribution of SOM neurons was significantly different only in the medio-lateral axis of the somatosensory nRT. The number of singly labeled SOM cells was significantly lower than PV cells only in the central tier of the middle sector of the nRT (Figures 1E and 1B). Only a minority of neurons displayed both neurochemical markers (10–20%) in the somatosensory nRT (Figure 1E).

PV and SOM Neurons Exhibit Different Intrinsic Membrane Excitability

The electrophysiological properties of neurons vary depending on their location in the nRT (Lee et al., 2007). Not all nRT cells have the classic rebound bursting mediated by low-threshold, transient Ca^{2+}-dependent depolarizations, called low-threshold calcium spikes (LTS) (Contreras et al., 1992; Jahnsen and Llinás, 1984). We sampled neurons across anterior-posterior, medial-lateral, and dorsal-ventral axes of the somatosensory nRT (Figure 9).

Passive and active membrane properties. To assess the electrophysiological properties of PV and SOM neurons between postnatal day 30 and 50 (P30–P50), we crossed PV-Cre and SOM-Cre mice with Ai32 mice expressing Cre-dependent channelrhodopsin-2 (ChR2). We identified cells via whole-cell patch clamping based on their opsin expression (Figure 9). We measured membrane potential changes in response

to a series of intracellular square current pulses (Figures 2A and 2F) and found that the input resistance (*R*in) and membrane time constant (τm) were similar in PV and SOM neurons (Table 1; Figure 2A). The membrane resting potential (Vm) and capacitance (*C*m) were also similar (Table 1), supporting that PV and SOM neurons have similar passive membrane properties. Also, PV and SOM neurons showed similar mean frequency-current *(F-I)* slope and rheobase [i.e., the minimal current intensity required to trigger an action potential (AP)] (Table S1; Figures 2E–2F)).

Low-threshold calcium spikes. In all nRT PV neurons (14 of 14 cells), a hyperpolarization to -95 mV or more was followed by a rebound of excitation characterized by a LTS crowned by a burst of APs. Of 14 PV neurons, 12 displayed repetitive rebound bursts and 2 produced single bursts (Figure 2A). Of 16 SOM neurons, 12 evoked a weak LTS after the same hyperpolarizing steps, and 4 did not evoke an LTS at all (Figure 2A).

We assessed the firing properties of these post-inhibitory rebound bursts. After similar responses to membrane potential hyperpolarizations, the maximal number of rebound bursts was threefold higher in PV than SOM neurons (Figure 2B). Also, the number of APs within the first burst and the intra-burst frequency of APs within the first burst were higher in PV than SOM neurons (Figure 2C–2D). Thus, SOM cells have weaker post-inhibitory rebound bursts than PV neurons.

T-type calcium current. Next, we studied if differences in LTS and post-inhibitory rebound bursting were controlled by T-type calcium currents (Figure 2G–K). The peak T-current density was higher in PV neurons (Figure 2H) compared to SOM neurons with LTS burst. The voltage-dependence of the steady-state inactivation (SSI) of T-currents was similar in PV and SOM neurons (Figure 2J)—similar half-maximal SSI voltages (*V50%*) and decay time constants (Figures 2I and 2K)—suggesting that PV and SOM neurons have similar biophysical properties of T-currents. The differences in T-currents between PV and SOM neurons did not depend on the specific location of the neuron within the dorsal-ventral, anterior-posterior, or medio-lateral axes. Thus, small T-current produces the weaker post-inhibitory rebound LTS bursting in SOM neurons, suggesting that SOM neurons contain fewer and/or more dendritically located T-type calcium channels.

To further validate PV-Cre, we used "INTRSECT" mice (Fenno et al., 2014) in which we selectively expressed ChR2 with the combinatorial virus (Cre-On, Flp-Off) in PVCre/SOMFlp (PV*) mice. This approach expressed ChR2 in PV neurons that do not express SOM. We examined the electrophysiological properties of neurons and found that PV* and PV neurons have similar intrinsic membrane properties, including post-inhibitory rebound bursting and T-currents (Figure 13A–D).

***Spontaneous synaptic activity*.** PV and SOM neurons had similar spontaneous excitatory and inhibitory postsynaptic currents (sEPSCs and sIPSCs) (Figure 10; Table S2).

PV and SOM Neurons of the nRT Project to Distinct Thalamocortical Relay Nuclei

To determine the post-synaptic targets of PV and SOM neurons, we injected virus containing enhanced Yellow Fluorescent Protein (eYFP) (Figures 3A,C,E) or ChR2-eYFP (Figures 3B,D,F) in the nRT of PV-Cre and SOM-Cre mice. nRT axons robustly expressed ChR2-eYFP 2–4 weeks post-injection, so we could activate axonal terminals while patching from thalamocortical relay cells in different nuclei. By evoking IPSCs, we verified that the projections observed with eYFP were functional. The major targets of PV neurons were the ventroposteromedial relay thalamic nuclei (VPM), ventroposterolateral (VPL) (Figure 3A,B left), and PO (Figure 3C,D left; see also Figure 11B). The major targets of SOM neurons were the intralaminar (IL) thalamocortical nuclei, in particular the parafascicular nucleus (PF) (Figure 3E,F right; see also Figure 11A), and to a lesser extent, the ventroposterolateral (VPL) (Figure 3A,B right) and the ventromedial (VM) thalamocortical relay nuclei. At high magnification, we saw axonal boutons and varicosities in the targeted structures (Figure 3 insets). The eIPSCs were recorded with kynurenic acid (2 mM) to block glutamatergic transmission and were abolished by the GABAA receptor blocker picrotoxin (data not shown). Patched cells were not directly activated, supporting that the opsin was not expressed in thalamocortical cells.

Optical stimulation was specific to nRT cells. We validated that the virus specifically targeted the nRT by serially sectioning the brain and noting the eYFP somatic expression in both PV-Cre and SOM-Cre mice (Figure 11). We observed the same targets with different viral volumes (see Supplemental

Information, Experimental Procedures).

PV and SOM Neurons in the Human nRT

The development and organization of the primate thalamus, particularly the organization of the GABAergic system, are different from rodents (Jones, 2007). A whole brain study found SOM immunoreactivity in the human thalamus but provided no direct evidence of cell bodies or axons (Bouras et al., 1987), and the co-localization of SOM and PV neurons had not been examined. We immunostained postmortem human thalami (Figure 4) and found SOM neurons at both anterior (Figure 4A) and posterior levels (not shown), and at dorsal and ventral positions. We also found varicose SOM axons in human thalamic sections containing the higher-order thalamocortical relays, including the IL (Figure 4E), mediodorsal, anteroventral, ventral anterior, and midline nuclei (Figure 4D). Notably, we discovered a distinct SOM+PV- subpopulation in human nRT, similar to mice.

Optical Activation of nRT PV but Not SOM Neurons Generates Oscillations in nRT-VB Microcircuit

Because PV neurons exhibit stronger intrinsic oscillatory properties than SOM neurons, we hypothesized that PV neurons are more likely to initiate network oscillations within the nRT-ventrobasal (VB) thalamic microcircuit. We used horizontal thalamic slices that conserve the connectivity between the nRT and VB thalamus (VB = VPM + VPL), in which we could assess nRT-VB intra-thalamic network oscillations independent of other structures (e.g., cortex) (Huntsman et al., 1999; Paz et al., 2011a, 2013; Makinson et al., 2017).

We measured intra-thalamic oscillations evoked by a single optical stimulation of PV or SOM neurons in slices prepared from PV-Cre or SOM-Cre mice expressing ChR2 (Figure 5). With a 16-channel linear array, we recorded multi-unit (MU) activity within the nRT and VB thalamus (Figure 5A). Optical activation of PV neurons consistently evoked rhythmic oscillatory bursting activity in VB (Figure 5B), similar to previous work using electrical stimulations of the internal capsule (Huntsman et al., 1999; Makinson et al., 2017; Paz et al., 2011a, 2013; Barthó et al., 2014). Activation of SOM cells in the nRT

evoked firing in VPL but not in VPM (Figure 5B). The number of active channels in VB (with a circuit oscillation evoked by an optical stimulation of nRT) and evoked bursts was higher in PV- than SOM-stimulated slices (Figure 5C,D). Evoked oscillatory firing in VB resulted from circuit oscillations in nRT-VB-nRT loops rather than direct activation of VB cells with light, because the light did not induce direct firing in VB channels (Figure 5B) and the VB neurons did not express ChR2 (see above). Optical activation of either PV or SOM cells also evoked a similar instantaneous firing in the nRT (Figures 5B,E), suggesting that weaker VB firing in SOM-stimulated slices is not due to weaker activation of SOM compared with PV neurons.

These findings support that PV neurons are the main oscillation generators in the nRT-VB somatosensory circuit because PV nRT neurons can generate circuit oscillations in the nRT–VPL/VPM–nRT loop, while SOM nRT neurons can generate circuit oscillations in VB only via the nRT–VPL–nRT loop.

Retrograde Synaptic Labeling Unveils Distinct Inputs to PV and SOM nRT Neurons

To learn whether nRT PV and SOM cells receive projections from distinct brain regions, we used a modified rabies, trans-synaptic tracing strategy (Wall et al., 2010, 2013) in PV or SOM Cre–expressing mouse lines. The first injection contained Cre-dependent adeno-associated viruses (AAV) expressing the avian tumor virus receptor A (TVA) tagged with mCherry and the rabies glycoprotein (RG). The second contained a modified rabies virus (EnvA) and was injected 21 days after the first injection (Figure 6A), which allowed rabies to infect cells in a Cre-dependent manner and be retrogradely trafficked to label inputs onto nRT neurons (Wall et al., 2010, 2013). We report the proportions of input cells in Figure 6B, because our helper virus did not allow us to simultaneously visualize starter and input cells. Inputs were normalized across each animal to prevent mice with many labeled inputs from biasing total input proportion. Only inputs that were detected in at least three mice were included in the analysis. For SOM-Cre (n=3) and PV-Cre (n=5) animals, we detected 150±46 and 307±40 total input cells, respectively ($p>0.5$, Mann-Whitney test).

We found distinct populations of afferent neurons targeting PV and SOM neurons in the nRT

(Figures 6B–C). When targeting SOM nRT cells, presynaptic cells were labeled in VPL and anterior thalamic nuclei (AN) (Figure 6B). SOM cells also received input from extrathalamic sources, including the central amygdala (CeA) and basal ganglia [the external segment of globus pallidus (GPe)] (Figure 6C). When targeting PV nRT cells, we saw presynaptic labeling mainly in the VPM and S1 cortex (Figures 6B–C). We found a small number of input cells in GPe and none in CeA or AN when targeting PV cells (Figure 6C). We also found input cells in the nRT when targeting both PV and SOM cells, with SOM cells having significantly more input cells (Figure 6C), suggesting that dendro-denritic or axo-dendritic intra-nRT connections exist preferentially onto SOM cells.

These projections are not exhaustive (Jones, 2007), because the virus may not have infected *all* nRT cells across the medial-lateral, dorsal-ventral, and anterior-posterior axes. However, our results show that within the same nRT regions, SOM and PV neurons are targeted by different brain regions. Importantly, the starter cells infected with the TVA-mCherry virus were located specifically in the nRT (Figure 12). A subpopulation of VPM cells expresses PV, and larger volume injections in nRT led to viral expression in VPM (see Supplemental Methods), but this did not change the input cell location that was mainly restricted to S1BF.

PV Cells More Robustly Induce Sigma Oscillations in the S1 Cortex During Free Behavior

As PV and SOM neurons segregate into different input-output circuits, we asked whether they could differentially control cortical states during free behavior. We designed devices containing multiple electro-corticogram (ECoG) screws in the cortex and a chronic multi-site optrode in the nRT (Figure 7A). A single, unilateral 20 ms-long optical activation of PV neurons evoked higher frequency and more robust oscillations than SOM neurons, mainly in the 7–15 Hz sigma range (Figures 7B–E). Such stimulations of nRT were previously shown to produce 7–15 Hz sleep spindles in the cortex (Halassa et al., 2011), but the cellular subtype of the nRT spindle generator remained unknown.

We also determined if we could reproduce the major effects of PV activation on the ECoG in PV-Cre mice by activating only PV* cells in the nRT. Using the INTRSECT approach (Fenno et al., 2014), we

selectively activated PV* cells in the nRT, which induced sigma-range oscillations in the S1 cortex (Figure 13 F-I) similar to that seen in PV-Cre mice.

PV but Not SOM Cells Affect Somatosensory-Related Whisker Behavior

Because PV cells more robustly modulate VPM and S1 cortical areas (Figures 5, 7), and because VPM is preferentially involved in whisker-related sensation, we hypothesized that PV cells would be preferentially involved in whisker-related behavior. With the adhesive-tape task (Bouet et al., 2009; Fleming et al., 2013), we tested whether disrupting the output of PV or SOM cells onto thalamocortical nuclei would alter somatosensory behavior. In PV-Cre-Ai32 and SOM-Cre-Ai32 mice, we placed adhesive tape on the left whiskers and manipulated the activity of PV or SOM cells in the right nRT that is functionally related to left-whisker perception. We manipulated the activity of ChR2-expressing PV or SOM cells with an optogenetic approach that has been established to disrupt thalamocortical output onto the cerebral cortex in a behavioral context (Reinhold et al., 2015). Activating PV but not SOM cells induced abnormal grooming of the whisker pad area that outlasted the optical stimulation protocol. Indeed, PV-targeted mice continued scratching the whisker pad area even after the tape was removed (Figure 7L, M). No such behavior was induced with light alone (Figure 7M), suggesting that manipulating nRT PV but not SOM neurons alters sensory perception in the mice during the task.

Optogenetic Targeting of PV but Not SOM Cells Instantaneously Disrupts Seizures

Given that nRT PV activation generates more robust oscillations in the cerebral cortex, we asked whether targeting these cells during seizures could effectively disrupt generalized cortical oscillations. We used low doses of pentylenetetrazol (PTZ), a well-established model of pharmacologically-induced generalized seizures mainly involving thalamocortical circuits (Beenhakker and Huguenard, 2009; Malafosee, 1994). We then used an optogenetic approach that can selectively modulate PV or SOM nRT neurons during free behavior. Such optogenetic manipulations have been used to silence relay thalamocortical output and assess

their effect on cortical states (Lewis et al., 2015). We found that a unilateral optical stimulation of nRT PV cells readily disrupted bilateral generalized seizures (Figure 7G,I,J,K) in PV-Cre mice injected with ChR2. We validated this result in PV* mice, in which targeting the PV+SOM- population immediately aborted ongoing seizures (Figure 13J-I). In contrast, activation of nRT SOM cells in SOM-Cre mice injected with ChR2 had much more stochastic effects on ongoing seizures (Figure 7H,I,J,K). The differences between PV and SOM mice did not result from differences in behavioral states (see Methods).

Discussion

The distinct effects of PV and SOM neurons on circuits have been extensively studied in other brain structures (Kim et al., 2016; Phillips and Hasenstaub, 2016; Wilson et al., 2012), but not in the nRT. Our study is the first to assign cellular and circuit properties to nuron populations of the nRT that can be differentially targeted with distinct molecular markers. We also provide the first evidence that singly labeled PV and SOM neurons co-exist in the human nRT. In mice, we found that PV and SOM neurons have distinct electrophysiological properties, segregate into different anatomical locations across the nRT, and participate in predominantly non-overlapping anatomical pathways that distinctly modulate thalamocortical circuits both *in vitro* and *in vivo.*

Who are the best pacemakers for thalamocortical thythmogenesis? The nRT needs LTS-mediated burst firing to generate spindle oscillatory activity in the thalamocortical circuit (Bazhenov et al., 2000; Beenhakker and Huguenard, 2009; Deschenes et al., 1984; Steriade et al., 1987). The nRT-VB loop is a key node of thalamocortical rhythm generation, because thalamocortical VB cells also fire LTS-mediated rebound bursts after hyperpolarization induced by nRT GABAergic inputs (Jahnsen and Llinás, 1984). We found that PV, but not SOM neurons, have larger T-currents, are rhythmogenic and recruit more robust oscillatory spindle-like activity in the cortex, suggesting that PV neurons are the main spindle rhythm generators in thalamocortical circuits. We also found that unilateral optogenetic targeting of PV nRT cells disrupts generalized seizures, supporting that PV nRT cells are preferentially involved in rhythmogenic thalamocortical circuits and could be "choke points" for seizure disruption (Paz and Huguenard, 2015). In contrast, targeting SOM cells can either interrupt or enhance seizures, suggesting a more nuanced effect on seizure rhythms. We propose that the PV nRT – VPM loop is the main pacemaking circuit in the somatosensory thalamus, in part because PV cells can fire more powerful rebound bursts and have more robust reciprocal connectivity with VPM neurons that are wired to oscillate in the sigma range. We propose that SOM nRT projections to the relay thalamus generate different global forebrain activity, which requires

further studies.

Potential Roles of Biased Inputs-Outputs of PV and SOM nRT Neurons

Our major finding is that PV and SOM cells are embedded in distinct circuits: PV nRT cells are mainly embedded in sensory circuits that involve inputs and outputs from specific thalamic nuclei (mainly VPM), whereas SOM nRT cells are mainly embedded in circuits that involve non-specific thalamocortical relay nuclei (AN, IL, PF thalami) that have broader projections onto many cortical regions, including PFC (Saalmann, 2014). In previous work (Crabtree, 1992), somatosensory and intralaminar thalamic nuclei shared nRT input. Our results suggest that this input is mostly mediated by SOM neurons, because SOM but not PV neurons project onto the intralaminar nuclei in addition to VPL. Validating this hypothesis will require *in vivo* intracellular or juxtacellular biocytin labeling of SOM cells and a 3D reconstruction of their axonal projections. Although previous studies showed that S1 cortex and VPM thalamus are the main excitatory afferents to nRT (Crabtree, 1992; Lam and Sherman, 2011), our results identify that PV neurons—the cellular substrate in nRT—receive these inputs. Thus, PV cells in the somatosensory nRT could be the main recipients of top-down cortical modulation of the thalamus and the main gatekeepers of somatosensory processing. Our finding that specifically manipulating PV cells induces excessive grooming after the tape was removed from the mouse's whiskers suggests that PV neurons are the main cellular substrates in the nRT involved in whisker-related sensory perception and memory. We propose that SOM nRT neurons are less involved in whisker-sensory related behaviors, supporting a lack of projections onto VPM, which modulates the S1 barrel cortex. This result will motivate future studies on how SOM neurons affect behavior.

The cerebral cortex is thought to be the main excitatory afferent of the nRT (Williamson et al., 1993; Liu and Jones, 1999). Thus, our finding that, at least in the somatosensory nRT, S1 cortex exclusively targets PV and not SOM neurons, whereas subcortical structures preferentially target SOM cells, is novel. Our work suggests that the cortex is not the main modulator of a major subset of nRT neurons, and it urges the need to revise the framework of input analysis in the somatosensory corticothalamo-cortical circuits by

including our findings that PV and SOM nRT cells differentially modulate information processing in these circuits.

What are the implications of preferential targeting of SOM nRT cells by limbic subcortical structures*?* Although studies have shown that the basal nucleus (BM/BL) and cortical nuclei (Co) of the amygdala project onto the nRT in non-human primates (Zikopoulos and Barbas, 2012), our study is the first to show a projection from the CeA to the nRT in mice. nRT SOM cells receive inputs from CeA and AN that are involved in selective attention (Holland et al., 2000) and emotional-attention interactions (Sun et al., 2015), respectively. Based on these inputs, we speculate that nRT SOM cells are the cellular substrates that impart emotional salience to attention. Furthermore, because SOM cells in the somatosensory nRT mainly receive projections from subcortical structures and target non-specific intralaminar thalamic nuclei that modulate the PFC (Saalmann, 2014), we propose that SOM cells are preferentially involved in the bottom-up limbic modulation of cortical circuits. Altogether, these inputs-outputs position the nRT SOM cells as the cellular targets to probe the limbic nature of nRT-mediated behavior.

What are the implications of preferential targeting of SOM nRT cells by GPe? Previous animal studies found that projections from the basal ganglia onto the nRT originate in the substantia nigra pars reticulata and GPe (Asanuma, 1989; Cornwall et al.,1990; Gandia et al., 1993; Hazrati and Parent, 1991; Jones, 2007). Our finding that GPe preferentially projects onto SOM cells in nRT suggests that SOM nRT cells could be central to communication between the basal ganglia and the thalamocortical relay nuclei. Thus, the GPe-SOM-TC pathway may affect behavioral switching and reward prediction (Gittis et al., 2014).

Technical Considerations

We studied PV and SOM neurons as they are the most abundantly expressed markers in rodent nRT (Lein et al., 2007). Future studies may include other neuron markers, such as neuropeptide Y (Brill et al., 2007), cholecystokinin (Cox et al., 1997), and vasoactive intestinal peptide (Burgunder et al., 1999).

The structure of the nRT does not support selective viral targeting, so we used multiple approaches

to ensure targeting specificity. We showed that 1) in both AAV-eYFP and transynaptic rabies studies, our viral approach sufficiently targeted most cells in the nRT; 2) with large viral volumes, the virus spread to VB in PV-Cre mice but did not affect the results or data interpretation; and 3) the major electrophysiological features *in vitro,* and the major circuit oscillation and seizure disruption properties *in vivo,* were similar in transgenic PV-CrexAi32 and virally targeted PV-Cre and PV*ConFoff mice. Thus, our results are not specific to one Cre line and do not result from non-specific targeting of brain regions other than the nRT.

nRT in Disease—A tale of two pathways?

Aberrant activity of the nRT affects many neurological and neuropsychiatric disorders (Paz et al., 2010; Slaght et al., 2002; Steriade, 2005; Ahrens et al., 2015; Ferrarelli and Tononi, 2011;Wells et al., 2016). We propose that PV cells generate rhythms that regulate sensory thalamocortical information processing, whereas SOM cells might gate limbic information and create informational salience. Within this framework, disruption of PV and SOM cells could lead to disorders with excessive rhythmogenesis (e.g., seizures) and psychiatric disorders (e.g., attention deficit disorder, schizophrenia), respectively. Our finding that pure, non-overlapping PV+SOM- and SOM+PV- cells co-exist in the human nRT supports these asymmetric roles.

Is There More than One Way to Pay Attention?

We propose that PV and SOM cells in the nRT might be differentially involved in top-down versus bottom-up thalamocortical information processing. Future work will evaluate whether these cell types interact within the nRT to integrate the different information needed for attention, consciousness, and perception. Also, the nRT—with its densely packed and perhaps interconnected PV and SOM cells—could be an ideal target to study the high co-morbidity between neurological and psychiatric disorders.

Finally, our results suggest that PV and SOM cells may mutually inhibit each other, providing another mechanism to tune what information the nRT, and in turn the thalamus, controls (Crick, 1984; Sohal et al., 2000).

Integrative brain functions require the flexible distribution of neuraly encoded information across large-scale brain circuits. Through its cellular subtypes, the nRT could differentially tune incoming information to coordinate brain-wide rhythms.

Experimental Procedures

Animals

We performed all experiments per protocols approved by the Institutional Animal Care and Use Committee at the University of California, San Francisco and Gladstone Institutes. Precautions were taken to minimize stress and the number of animals used in all experiments. Adult (P30-P200) male and female mice were used. Somatostatin (SOM)-Cre mice (SOM-IRES-Cre, IMSR_JAX:013044; mixed C57BL/6;129S4), Parvalbumin (PV)-Cre mice (PV-Cre, IMSR_JAX: 017320; C57BL/6 congenic), Rosa26-tdTomato reporter mice (Ai14, IMSR_JAX:007914; congenic C57BL/6 generously provided by Dr. Ken Nakamura, Gladstone Institutes); Rosa26-ChR2(H134R)-EYFP reporter mice (Ai32, IMSR_JAX:012569; mixed C57BL/6;129S4), C57BL/6J mice (wild-type, IMSR_JAX:000664), and PV-Cre/SOM-Flp mice (PV-p2A-Cre, SOM-IRES-Flp (Fenno et al., 2014) were used.

Surgery

We performed stereotaxic injections of viruses into nRT as described (Paz et al., 2011, 2013). We targeted nRT with stereotaxic coordinates ranging from 1.3–1.6 mm posterior to Bregma and 2.0–2.1 mm lateral to the midline at two different injection depths (2.6 and 3.0 mm) ventral to the cortical surface. To determine the effects of PV or SOM neuron activation on cortical rhythms and behavior, we used PV-Ai32 and SOM-Ai32 mice, as well as PV-Cre, SOM-Cre, and PV-Cre/SOM-Flp mice previously injected with virus encoding ChR2, for simultaneous ECoG and thalamic LFP/MU recording combined with optical stimulation in nRT as described (Paz et al. 2011, Paz et al., 2013).

Immunostaining, Microscopy, and Image Analysis

Immunohistochemistry on mouse brain sections was performed as described (Paz et al., 2010). Primary antibodies were PV (1:2000, mouse, Sigma, P3088, AB_47732) or SOM (1:1000, mouse, Peninsula Labs, AB_2302603) and corresponding fluorescent secondaries (see Supplemental Experimental Procedures).

For human tissue staining, we used control human thalamic tissues (n=3) from two male subjects (55- and 77-years-old) and one female subject (77-years-old) who all died from causes not linked to brain diseases and who had no history of neurological disorders. All procedures were approved by the Regional and Institutional Committee of Science and Research Ethics of Scientific Council of Health (ETT TUKEB 31443/2011/EKU (518/PI/11)). Antibodies used targeted PV (1:2000, rabbit, Swant, Marly, Switzerland, code PV25, AB_10000344) or SOM (1:500, rat, Merck Millipore, code MAB 354, AB_2255365). PV immunolabeling was visualized with fluorescent secondaries, and SOM immunolabeling was visualized and enhanced using a biotinylated secondary and the nickel-intensified DAB (DAB-Ni) chromogen. See Supplemental Experimental Procedures for detailed image acquisition parameters.

Whole-cell patching and thalamic oscillation recordings in slices

Acute slice electrophysiology for both whole-cell patching and thalamic oscillation recordings were done as described (Paz et al., 2010, 2011b). For thalamic oscillation recordings, we used a linear 16-channel multi-electrode array (Neuronexus) spanning nRT and VB. Evoked oscillations were elicited by activating PV or SOM neurons of the nRT by delivering 450 nm blue light (0.8–5 mW, 100 ms duration every 10 s) to the nRT via a 200 μm optical fiber (Thorlabs). See Supplemental Experimental Procedures for detailed electrophysiological parameters.

***In Vivo* Electrophysiology, Seizure Interruption, and Somatosensory Behavior**

Electrophysiological recordings in freely-behaving mice were performed as described (Paz et al., 2013). We recorded ECoG and thalamic LFP/MU signals using an RZ5 (TDT). ECoG and thalamic LFP was sampled at 1221 Hz and thalamic extracellular MU was sampled at 24 kHz. To evoke cortical rhythms, we delivered 8–20 mW of 450 nm power (measured at the end of the ferrule, before connection to the implanted optical fiber) to the optical fiber implanted in nRT.

We used a low dose of the proconvulsant pentylenetetrazol (PTZ, 35–60 mg/kg) injected intraperitoneally to induce pharmacological seizures in mice previously instrumented for simultaneous

ECoG recordings and thalamic optical stimulation. Experimenters visually monitored ECoG and thalamic LFP/MUA signal for spike-and-wave seizures and brief generalized spiking seizure episodes (<10 s). During seizures that were >1 s in length, experimenters triggered optical stimulation (4 s, 450 nm, 25–35 mW of power measured from the tip of the ferrule, before connection to the implanted optical fiber).

To assess whisker-related somatosensory behaviors, the same mice were subjected to a modification of the adhesive removal task behavior involving the front paws and whisker pad (Bouet et al., 2009) with and without optical manipulation of nRT.

Statistical Analyses

All numerical values are given as means and error bars are standard error of the mean (SEM) unless stated otherwise. Parametric and non-parametric tests were chosen as appropriate and were reported in figure legends. Data analysis was performed with MATLAB (SCR_001622), Origin 9.0 (Microcal Software, SCR_002815), GraphPad Prism 6 (SCR_002798), R-project, and SigmaPlot (SCR_003210). (*$p<0.05$, **$p<0.01$, ***$p<0.001$).

Detailed experimental procedures and statistical analyses for each experiment can be found in Supplemental Experimental Procedures.

Experimental Model Details

We performed all experiments per protocols approved by the Institutional Animal Care and Use Committee at the University of California, San Francisco and Gladstone Institutes. Precautions were taken to minimize stress and the number of animals used in each set of experiments. Animals were separately housed after surgical implants.

Somatostatin (SOM)-Cre mice (SOM-IRES-Cre, IMSR_JAX:013044; mixed C57BL/6;129S4), Parvalbumin (PV)-Cre mice (PV-Cre, IMSR_JAX: 017320; C57BL/6 congenic), Rosa26-tdTomato reporter mice (Ai14, IMSR_JAX:007914; congenic C57BL/6 generously provided by Dr. Ken Nakamura,

Gladstone Institutes); Rosa26-ChR2(H134R)-EYFP reporter mice (Ai32, IMSR_JAX:012569; mixed C57BL/6;129S4), C57BL/6J mice (wild-type, IMSR_JAX:000664), and PV-Cre/SOM-Flp mice (PV-p2A-Cre, SOM-IRES-Flp (Fenno et al., 2014).), were housed in the Research Animal Facility at the Gladstone Institutes. Both male and female mice were used for these experiments.

Viral injections

Stereotaxic viral injections were carried out as described (Paz et al., 2011, 2013).

For eYFP tracing studies (Figure 3) (UNC Joint Vector Laboratories, SCR_002448), a total of 200-500 nl of concentrated virus (2×10^{12} genome copies per milliliter) carrying genes for eYFP alone (rAAV5/EF1a-EYFP for PV-Cre or SOM-Cre) were injected in nRT. Different injections volumes were found to have comparable projection patterns. Images shown are for mice containing a total of 500 nl.

For optogenetic experiments, both *in vivo* (Figure 7) and *in vitro* (Figure 3) a total of 400 nl of concentrated virus (2×10^{12} genome copies per milliliter) carrying genes for ChR2 (rAAV5/EF1a-DIO-ChR2-EYFP for PV-Cre or SOM-Cre mice; rAAV5/hSyn-Con/Foff-hChR(H134R)-eYFP (INTRSECT virus) for PV-Cre/SOM-Flp mice) was used.

The virus was injected stereotaxically unilaterally into the right nRT of P30-P60 mice. For the PV-Cre, SOM-Cre mice, and PV-Cre/SOM-Flp mice, the stereotaxic coordinates of the injections were 1.3–1.6 mm posterior to Bregma, 2.0–2.1 mm lateral to the midline. Two injections, each containing half the total volume (100-250 nl), were made at 2.6 and 3.0 mm ventral to the cortical surface. We allowed the viruses to express for anywhere between 3 weeks and 3 months, depending on the nature of the experiment.

For trans-synaptic labeling (Figure 6), 200-400 nl (two 100 nl or 200 nl injections) of a 1:1 mixture of AAV CAG-FLEx-RG and AAV CAG-FLEx-TVA-mCherry were first injected using the same coordinates to target nRT as above, followed by a second injection 2 weeks later of 200 nl (two 100 nl injections) of

pseudotyped RV (ΔG-GFP+EnvA). To avoid viral spreading into neighboring areas, we used a smaller amount of virus for trans-synaptic labeling than we did for optogenetic and anterograde tracing experiments. Animals were kept alive for 7 days after RV injection to allow trans-synaptic spreading and sufficient GFP labeling in presynaptic cells. No additional labeling was required to observe GFP or mCherry signal.

Immunostaining, Microscopy, and Image Analysis

Mice were anesthetized with a lethal dose of ketamine (300 mg/kg) and xylazine (30 mg/kg) and perfused with 4% paraformaldehyde in 1X PBS. Serial coronal sections (50 μm thick) were cut on a Leica SM2000R Sliding Microtome. Sections were incubated with antibodies directed against PV (1:2000, mouse, Sigma, P3088, AB_47732) or SOM (1:1000, mouse, Peninsula Labs, AB_2302603) overnight at 4°C. After wash, sections were incubated with Alexa Fluor–conjugated secondary antibodies (1:300, Thermo Fisher Scientific, A-11029) for 2 h at room temperature. Sections were mounted in an antifade medium (Vectashield). To measure the proportion of PV+SOM-, PV-SOM+, and PV+SOM+ cells, we used immunostaining for PV as a corollary for PV expression and the tdTomato reporter as a corollary for SOM expression on sections obtained from the SOM-Ai14 mice.

For the analysis shown in Figure 1, confocal imaging was performed using a confocal laser scanning microscope (LSM880, Zeiss) equipped with a Plan Apochromat 20x/“0.75” NA or 63x/1.4 NA oil immersion objective lens. A multi-line Argon laser was used for 488 nm excitation of the AlexaFluor488 and a 561 nm HeNe laser for excitation of tdTomato. Slices used for imaging corresponded to a Bregma location of approximately -1.3 posterior from Bregma, ± 0.2 mm. A series of 20x images were taken of the head, middle, and tail sections of nRT from 2 slices per mouse (n=4 mice) using a Z-stack to capture the entirety of the labeled cell population within the focal plane. These images were used for cell counting. Cells were counted as either green only (PV+), red only (SOM+) or both green and red (PV+ SOM+, referred to as “coexpressing” in Figure 1) using Bitplane Imaris (SCR_007370). The nRT was outlined

using the PV signal and confirmed using the mouse brain atlas (Franklin and Paxinos, 2007). A separate set of 63x images using a Z-stack were also taken to more clearly show non-overlapping populations. Bitplane Imaris (SCR_007370) was used to render a 3D image of each region from nRT. For the 63x image, processing and figure preparations were performed using a combination of Bitplane Imaris (3D rendering of Z-stacks) and Fiji (http://fiji.sc/wiki/index.php/Fiji). For Figure 6, images were taken with a Biorevo BZ-9000 Keyence microscope at 20x-40x. Input cells were quantified by measuring the total number of green cells in the observed brain nuclei. Ratios were taken by dividing input cells per nuclei over total cells counted.

Immunostaining of Human Tissue

Control human thalamic tissues (n=3) were obtained from two males (55- and 77-years-old) and one female (77-years-old) subjects who died from causes not linked to brain diseases. None of them had a history of neurological disorders. The three subjects were processed for autopsy in Saint Borbála Hospital, Tatabánya, Department of Pathology. Informed consent was obtained for the use of brain tissue and for access to medical records for research purposes. Tissue was obtained and used in a manner compliant with the Declaration of Helsinki. All procedures were approved by the Regional and Institutional Committee of Science and Research Ethics of Scientific Council of Health (ETT TUKEB 31443/2011/EKU (518/PI/11)). Brains were removed 4–5 h after death. The internal carotid and the vertebral arteries were cannulated, and the brains were perfused first with physiological saline (using a volume of 1.5 L in 30 min) containing heparin (5 ml), followed by a fixative solution containing 4% paraformaldehyde, 0.05% glutaraldehyde and 0.2% picric acid (vol/vol) in 0.1 M PB, pH 7.4 (4–5 l in 1.5–2 h). The thalamus was removed from the brains after perfusion, and was postfixed overnight in the same fixative solution, except for glutaraldehyde, which was excluded.

Postmortem formalin fixed human thalami were cut on a vibratome with section thickness of 50 µm. The sections were incubated with 10% normal goat serum followed by the overnight incubation with the mixture of rabbit anti-parvalbumin (1:2000; Swant, Marly, Switzerland, code PV25, AB_10000344) and rat anti-somatostatin (1:500; Merck Millipore, code MAB 354, AB_2255365). Parvalbumin was visualized with the fluorescent dye Alexa488 conjugated goat anti-rabbit (1:500; Molecular Probes, Leiden, The Netherlands, code A-11001). Whereas somatostatin with biotinylated-SP (long spacer) goat anti-rat (1:300; Jackson Immuno Research, Newmarket, Suffolk, UK, code 112-065-167) and by avidin-biotinylated horseradish peroxidase complex (1:300; ABC, Vector, code PK-6200). This immunoreaction was visualized using nickel intensified DAB (DAB-Ni) as the chromogen.

Slice preparation

Mice were euthanized with 4% isoflurane, perfused with ice-cold sucrose cutting solution containing 234 mM sucrose, 2.5 mM KCl, 1.25 mM NaH_2PO_4, 10 mM $MgSO_4$, 0.5 mM CaCl2, 26 mM $NaHCO_3$, and 11 mM glucose, equilibrated with 95% O_2 and 5% CO_2, pH 7.4, and decapitated. We prepared 250 µm-thick horizontal thalamic slices containing VB thalamus and nRT with a Leica VT1200 microtome (Leica Microsystems). We incubated the slices, initially at 32 °C for 1 h and then at 24–26 °C, in artificial cerebro-spinal fluid (ACSF) containing 126 mM NaCl, 2.5 mM KCl, 1.25 mM NaH_2PO_4, 2 mM $MgCl_2$, 2 mM $CaCl_2$, 26 mM $NaHCO_3$, and 10 mM glucose, equilibrated with 95% O_2 and 5% CO_2, pH 7.4. The thalamic slice preparation was performed as described (Paz et al., 2011, 2013).

Patch-clamp electrophysiology from thalamic slices

Recordings were performed as previously described (Paz et al., 2011, 2013). We visually identified nRT and thalamocortical neurons by differential contrast optics with a Zeiss (Oberkochen) Axioskop microscope and an infrared video camera. Recording electrodes made of borosilicate glass had a resistance of 2.5–4 MΩ when filled with intracellular solution. Access resistance was monitored in all the recordings, and cells were included for analysis only if the access resistance was <25 MΩ. Cells were filled with 0.2–0.5%

biocytin (Sigma-Aldrich), and whole slices were fixed and processed using standard avidin–biotin peroxidase (Horikawa and Armstrong, 1988). We corrected the potentials for -15 mV liquid junction potential. Intrinsic and bursting properties and spontaneous and evoked inhibitory post-synaptic currents (IPSCs) were recorded in the presence of kynurenic acid (2 mM, Sigma). For IPSCs, the internal solution contained 135 mM CsCl, 10 mM HEPES, 10 mM EGTA, 5 mM QX-314 (lidocaine N-ethyl bromide), and 2 $MgCl_2$, pH adjusted to 7.3 with CsOH (290 mOsm). Excitatory post-synaptic currents (EPSCs) were recorded in the presence of picrotoxin (50 µM, Tocris). For EPSCs and current-clamp recordings, the internal solution contained 120 mM potassium gluconate, 11 mM KCl, 1 mM $MgCl_2$, 1 mM $CaCl_2$, 10 mM HEPES, and 1 mM EGTA, pH adjusted to 7.4 with KOH (290 mOsm). Immunofluorescence was assessed with a Biorevo BZ-9000 Keyence microscope.

Extracellular thalamic oscillations

Horizontal slices (400 µm) containing the VB and nRT were placed in a humidified, oxygenated interface chamber and perfused at a rate of 2 mL/min at 34°C with oxygenated ACSF prepared as described above and supplemented with 300 µM glutamine for cellular metabolic support. Extracellular MU recordings were obtained with a 16-channel multi-electrode array (Neuronexus) placed in the nRT and VB. Signals were amplified at 10,000x and band-pass filtered between 100 Hz and 6 kHz using the RZ5 from Tucker-Davis Technologies (TDT, SCR_006495). PV and SOM neurons of the nRT were locally activated by a 450 nm blue light optical pulse (0.8–5 mW, 100 ms duration every 10 s) delivered to the nRT via a 200 µm optical fiber (Thorlabs). Sweeps were repeated 10–30 times in a single recording. Position of recording probe was visually checked for each recording to confirm position of electrodes in nRT and VB.

***In vivo* data acquisition during free behavior**

We designed devices containing multiple screws for acquisition of electrocorticogram (ECoG) signal, along with local field potential (LFP) and multi-unit (MU) signal recoded from tungsten electrode wires that were

positioned approximately 300 µm from the tip of an optic fiber (200 µm core, ThorLabs) (Paz et al., 2013). Cortical screws were implanted in S1 (-0.5 mm posterior from Bregma, ± 3.25 mm lateral), in V1 (-2.9 mm posterior from Bregma, ± 3.25 mm lateral), or in lieu of two V1 channels, in PFC (0.5 mm anterior to Bregma, 0 mm lateral). For manipulation of nRT, optrodes were implanted at -1.3 mm posterior from Bregma, 2.1 mm lateral, and 2.5 mm deep. Mice were allowed to recover for at least one week before recording. ECoG signals were recorded using RZ5 (TDT) and sampled at 1221 Hz, and thalamic extracellular MU signals were sampled at 24 kHz. A video camera that was synchronized to the signal acquisition was used to continuously monitor the animals. Each recording trial lasted 30–60 min. To control for circadian rhythms, we housed our animals using a regular light/dark cycle, and performed recordings between roughly 11:00 AM and 4:00 PM.

***In vivo* optogenetics**

We simultaneously passed a fiber optic with an inline rotating joint (Doric) through a concentric channel in the electrical commutator, and connected it to the 200 µm core fiber optic in each animal's headpiece while recording ECoG/MU. The fiber optic was connected to a 450 nm wavelength laser control box, which was triggered externally using the RZ5 (TDT). The tip of the fiber rested 300 µm from the most dorsal tungsten electrode on each optrode to allow maximal activation of the nRT without physically obstructing the electrodes. We used 8–20 mW of 450 nm blue light, measured at the end of the optical fiber before connecting to the animals. nRT cells were stimulated using 20 ms light pulses, delivered every 10 seconds.

Optogenetic disruption of Seizures

We used a low dose of the proconvulsant pentylenetetrazol (PTZ, 35 – 60 mg/kg) injected intraperitoneally to induce pharmacological seizures in mice who were previously instrumented for simultaneous ECoG recordings and thalamic optical stimulation as described above. After injection, mice were placed in their home cage and left to behave freely. Experimenters visually monitored ECoG and thalamic LFP/MUA

signal for spike-and-wave seizures and brief generalized spiking seizure episodes (< 10 s). During seizures that were > 1 s in length, experimenters manually triggered the optical stimulation (4 s, 450 nm, 25 – 35 mW measured at the end of the optical fiber before connecting to the animals). Trials were considered to be valid if the experimenter triggered the light during an ongoing seizure. A custom Matlab script was used to identify valid stimulation trials off-line after data collection. The number of trials per mouse ranged from 3 - 23, with the majority of mice having at least 5 trials sampled per mouse.

Optogenetic manipulation of Somatosensory Behavior

To assess somatosensory-related behaviors, we used the same mice who were instrumented for optical stimulation experiments in a modification of the adhesive removal task behavior involving the front paws and whisker pad (Bouet et al., 2009). Briefly, on the test day, we restrained the mice and applied a piece of zinc oxide tape (5 mm x 10 mm) to the left whisker pad area as shown in Figure 7M. Mice were immediately returned to their home cage, and we recorded the contact time (time to touch the tape), removal time (time to remove tape) and grooming time (time spent grooming facial area after tape was removed) per trial. Each mouse was subjected to three trials spread over ~20 minute per condition. Mice were handled for 1-2 days to habituate to the experimenter, and then subjected to a baseline test day to reduce novelty associated with the task. We then performed successive test days of sham (no optical stimulation), light stimulation (10 s light stimulation upon attachment of tape to the whisker pad), sham (no optical stimulation) and a light alone trial (no tape used). Light stimulation used 450 nm of blue light, 15 mW measured at the end of the optical fiber before connecting to the animals. An experimenter measured time spent grooming off-line using video scoring. Responses across trials were averaged per condition. Trials were excluded if the tape fell off prior to the mouse being returned to their home cage.

QUANTIFICATION AND STATISTICAL ANALYSIS

All numerical values are given as means and error bars are Standard Error of the Mean (SEM) unless stated otherwise. Parametric and non-parametric tests were chosen as appropriate. Data analysis was performed

with MATLAB (SCR_001622), Origin 9.0 (Microcal Software, SCR_002815), GraphPad Prism 6 (SCR_002798), R-project, and SigmaPlot (SCR_003210).

Image analysis and cell quantification

For cell quantification, a single image of either the head, middle, or tail of nRT was analyzed for labeled cell counts (Figure 1E). A combination of automated cell-counting algorithms was applied using the "shape" feature of Imaris to count all labeled somas in either the red or the green channel. To determine the fraction of cells that were double-labeled, an additional mean intensity filter for the green channel was applied to the red channel to identify populations that were double-labeled. Note, PV labeling that was clearly perisomatic was used to identify cells that were double-labeled. The remaining PV label that was punctate that presumably corresponded to fibers and other unidentified cellular compartments was not considered to be cellular labeling because the origin of the labeling was not clear. Final cell counts were expressed as a relative proportion of each group, with the total cell counts corresponding to counts from the "red" plus "green condition data are represented as mean and error bars are standard error of the mean. Data were analyzed using Mann-Whitney test, with alpha = 0.05 (*$p<0.05$, **$p<0.01$, ***$p<0.001$, ****$p<0.0001$). For Figure 1E, a total of 4 mice were used for analysis (n = 2 slices per mouse, 1 image per nRT region).

Comparison of electrophysiological properties between PV and SOM nRT cells

For recordings of 14 PV cells and 16 SOM cells, spikes over -20 mV during 0.6 sec stimulations of 20 to 400 pA were counted automatically using custom R-Project code. Spiking frequency was computed as the spike count divided by the stimulus duration (Figure 2E). Data for half-maximal voltage ($V_{50\%}$) was taken from the Boltzmann function (Figure 2K; 11 PV cells from four mice and 10 bursting SOM cells from eight

mice). Data from Figure 2B-D & H-K were compared using a Mann-Whitney test, with alpha = 0.05. (*p<0.05, **p<0.01, ***p<0.001).

Curves of spikes per second vs. current and their quantiles were plotted using R-Project's ggplot package. The reported rheobase averages and SEMs were computed based on the current which first caused at least one spike during the stimulus per recording (Table S1). The slope averages were computed from the average least squared regression of individual curves over supports which were greater than each recording's computed rheobase. The slope SEMs were computed similarly. Both p-values were computed using the R-Project's aov built-in function. Data from Tables S1 and S2 were analyzed using t-tests (with pooled variances when the equal variance test passed) or Mann-Whitney otherwise with alpha = 0.05 (*p<0.05, **p<0.01, ***p<0.001, ****p<0.0001).

Cumulative probability distributions and KS-Test p-values (Figure 10 B-C) were generated using the bootstrap method with 1000 iterations. sIPSC interval CDFs and p-values were generated from 17 PV and 10 SOM cells (three mice for each group) using 30 sweeps from each cell per iteration. All other sIPSC variables were generated from 12 PV and 8 SOM cells (n = 3 SOM mice, n = 5 PV mice) using 30 sweeps from each cell per iteration. sEPSC interval CDFs and p-values were generated from 14 PV and 10 SOM cells using 80 sweeps from each cell per iteration. All other sEPSC variables were generated from 11 PV and 10 SOM cells using 80 sweeps from each cell per iteration. The probability distributions were similar in SOM and PV neurons (p>0.1 for all the parameters; Table S2).

Comparison of thalamic circuit oscillations in thalamic slices

Quantification of number of active channels in VB that presented an evoked oscillatory response (Figure 5C) and number of total evoked bursts recorded in all VB channels (Figure 5D) was obtained from five sweeps of each recording (n = 4 slices from three PV mice, n = 5 slices from three SOM mice). All data were compared using a Mann-Whitney test, with alpha = 0.05. (*p<0.05, **p<0.01, ***p<0.001).

Analysis of cortical modulation by selective optical activation of nRT during free behavior

ECoG analysis: For induction trials, the number of oscillation cycles per recording was determined through visual observation of the mean EEG trace across all stimuli. Only oscillations evident above background noise and between 5-15 Hz were counted, and the difference between groups was analyzed using a Mann-Whitney rank sum test ($p<0.05$). Line length was extracted for the 500 ms following each 20 ms light stimulus. Raw data sampled at 24 kHz was bandpass filtered between 7-15 Hz and z-scored, then the line length was calculated as the sum of absolute differences between samples. Differences between cumulative probability distributions were quantified using the two-sample Kolmogorov-Smirnov (KS) test. CDFs were generated using data from all individual stimulus trials for each group (PVxAi32 = 2309 trials, SOMxAi32 = 2003 trials, PV-Cre = 400 trials, SOM-Cre = 1000 trials, PV+SOM- = 1400 trials).

For disruption trials, PreStim was defined as 2 s before stimulus onset, and PostStim was defined as 2 s after light stimulus, excluding the initial 200 ms of the response to avoid the large stimulus evoked transient. We calculated relative changes in root-mean-squared (RMS) power from PreStim → Stim and repeated this analysis for each condition to statistically evaluate the effect of the light on the ECoG across the different mouse groups (Figure 7). Summary CDFs for the change in RMS power were generated using data from the ipsilateral somatosensory cortex (S1) including all valid trials for each group (PV-Cre = 40 trials, SOM-Cre = 51 trials, PV+SOM- = 47 trials).

Analysis of Somatosensory Behavior

Responses were averaged across trials per condition per mouse. Responses for evoked grooming were analyzed using a two-way mixed model ANOVA with genotype (PV-Cre x Ai32 or SOM-Cre x Ai32) as one factor and treatment (sham1, light, sham2, light alone – no tape) as the repeated measures factor. Posthoc multiple comparison tests (Sidak's) were used to determine whether treatment conditions were

significantly different from Sham1 within groups. Alpha was set to 0.05 and adjusted for 6 comparisons (*$p<0.05$).

References

Ahrens, S., Jaramillo, S., Yu, K., Ghosh, S., Hwang, G.-R., Paik, R., Lai, C., He, M., Huang, Z.J., and Li, B. (2015). ErbB4 regulation of a thalamic reticular nucleus circuit for sensory selection. Nat Neurosci *18*, 104–111.

Asanuma, C. (1989). Axonal arborizations of a magnocellular basal nucleus input and their relation to the neurons in the thalamic reticular nucleus of rats. Proc. Natl. Acad. Sci. U. S. A. *86*, 4746–4750.

Barthó, P., Slézia, A., Mátyás, F., Faradzs-Zade, L., Ulbert, I., Harris, K.D., and Acsády, L. (2014). Ongoing Network State Controls the Length of Sleep Spindles via Inhibitory Activity. Neuron *82*, 1367–1379.

Bazhenov, M., Timofeev, I., Steriade, M., and Sejnowski, T. (2000). Spiking-Bursting Activity in the Thalamic Reticular Nucleus Initiates Sequences of Spindle Oscillations in Thalamic Networks. J. Neurophysiol. *84*, 1076.

Beenhakker, M.P., and Huguenard, J.R. (2009). Neurons that Fire Together Also Conspire Together: Is Normal Sleep Circuitry Hijacked to Generate Epilepsy? Neuron *62*, 612–632.

Bouet, V., Boulouard, M., Toutain, J., Divoux, D., Bernaudin, M., Schumann-Bard, P., and Freret, T. (2009). The adhesive removal test: a sensitive method to assess sensorimotor deficits in mice. Nat Protoc. *4*, 1560–1564.

Brill, J., Kwakye, G., and Huguenard, J.R. (2007). NPY signaling through Y1 receptors modulates thalamic oscillations. NPY COHORTS Hum. Dis. 8th Int. NPY Meet. 2006 *28*, 250–256.

Burgunder, J.-M., Heyberger, B., and Lauterburg, T. (1999). Thalamic reticular nucleus parcellation delineated by VIP and TRH gene expression in the rat. J. Chem. Neuroanat. *17*, 147–152.

Calabrò, R.S., Cacciola, A., Bramanti, P., and Milardi, D. (2015). Neural correlates of consciousness: what we know and what we have to learn! Neurol. Sci. *36*, 505–513.

Contreras, D., Curro Dossi, R., and Steriade, M. (1992). Bursting and tonic discharges in two classes of reticular thalamic neurons. J. Neurophysiol. *68*, 973.

Cornwall, J., Cooper, J., and Phillipson, O. (1990). Projections to the rostral reticular thalamic nucleus in the rat. Exp. Brain Res. *80*, 157–171.

Cox, C.L., Huguenard, J.R., and Prince, D.A. (1997). Peptidergic Modulation of Intrathalamic Circuit Activity In Vitro: Actions of Cholecystokinin. J. Neurosci. *17*, 70.

Crabtree, J.W. (1992). The Somatotopic Organization Within the Cat's Thalamic Reticular Nucleus. Eur. J. Neurosci. *4*, 1352–1361.

Crick, F. (1984). Function of the thalamic reticular complex: the searchlight hypothesis. Proc. Natl. Acad. Sci. *81*, 4586–4590.

Csillik, B., Mihály, A., Krisztin-Péva, B., Chadaide, Z., Samsam, M., Knyihár-Csillik, E., and Fenyo, R. (2005). GABAergic parvalbumin-immunoreactive large calyciform presynaptic complexes in the reticular nucleus of the rat thalamus. J. Chem. Neuroanat. *30*, 17–26.

Dang-Vu, T.T., McKinney, S.M., Buxton, O.M., Solet, J.M., and Ellenbogen, J.M. (2010). Spontaneous brain rhythms predict sleep stability in the face of noise. Curr. Biol. *20*, R626–

R627.

Deschenes, M., Paradis, M., Roy, J.P., and Steriade, M. (1984). Electrophysiology of neurons of lateral thalamic nuclei in cat: resting properties and burst discharges. J. Neurophysiol. *51*, 1196.

Fenno, L.E., Mattis, J., Ramakrishnan, C., Hyun, M., Lee, S.Y., He, M., Tucciarone, J., Selimbeyoglu, A., Berndt, A., Grosenick, L., et al. (2014). Targeting cells with single vectors using multiple-feature Boolean logic. Nat Meth *11*, 763–772.

Ferrarelli, F., and Tononi, G. (2011). The Thalamic Reticular Nucleus and Schizophrenia. Schizophr. Bull. *37*, 306–315.

Fleming, S.M., Ekhator, O.R., and Ghisays, V. (2013). Assessment of Sensorimotor Function in Mouse Models of Parkinson's Disease. e50303.

Gandia, J., De las Heras, S., and Gimenez-Amaya, J. (1993). Afferent projections to the reticular thalamic nucleus from the globus pallidus and the substantia nigra in the rat. Brain Res. Bull. *4*, 351–358.

Gentet, L.J., and Ulrich, D. (2003). Strong, reliable and precise synaptic connections between thalamic relay cells and neurones of the nucleus reticularis in juvenile rats. J. Physiol. *546*, 801–811.

Gittis, A.H., Berke, J.D., Bevan, M.D., Chan, C.S., Mallet, N., Morrow, M.M., and Schmidt, R. (2014). New Roles for the External Globus Pallidus in Basal Ganglia Circuits and Behavior. J. Neurosci. *34*, 15178.

Halassa, M.M., and Acsády, L. (2016). Thalamic Inhibition: Diverse Sources, Diverse Scales. Trends Neurosci. *39*, 680–693.

Halassa, M.M., Siegle, J.H., Ritt, J.T., Ting, J.T., Feng, G., and Moore, C.I. (2011). Selective optical drive of thalamic reticular nucleus generates thalamic bursts and cortical spindles. Nat Neurosci *14*, 1118–1120.

Halassa, M.M., Chen, Z., Wimmer, R.D., Brunetti, P.M., Zhao, S., Zikopoulos, B., Wang, F., Brown, E.N., and Wilson, M.A. (2014). State-Dependent Architecture of Thalamic Reticular Subnetworks. Cell *158*, 808–821.

Hazrati, L.-N., and Parent, A. (1991). Projection from the external pallidum to the reticular thalamic nucleus in the squirrel monkey. Brain Res. *550*, 142–146.

Hou, G., Smith, A.G., and Zhang, Z.-W. (2016). Lack of Intrinsic GABAergic Connections in the Thalamic Reticular Nucleus of the Mouse. J. Neurosci. *36*, 7246.

Houser, C.R., Vaughn, J.E., Barber, R.P., and Roberts, E. (1980). GABA neurons are the major cell type of the nucleus reticularis thalami. Brain Res. *200*, 341–354.

Huntsman, M.M., Porcello, D.M., Homanics, G.E., DeLorey, T.M., and Huguenard, J.R. (1999). Reciprocal Inhibitory Connections and Network Synchrony in the Mammalian Thalamus. Science *283*, 541.

Jahnsen, H., and Llinás, R. (1984). Electrophysiological properties of guinea-pig thalamic neurones: an in vitro study. J. Physiol. *349*, 205–226.

Jones, E.G. (2007). The Thalamus 2 Volume Set (Cambridge University Press).

Jones, E.G., and Hendry, S.H.C. (1989). Differential Calcium Binding Protein Immunoreactivity Distinguishes Classes of Relay Neurons in Monkey Thalamic Nuclei. Eur. J. Neurosci. *1*, 222–246.

Kim, D., Jeong, H., Lee, J., Ghim, J.-W., Her, E.S., Lee, S.-H., and Jung, M.W. (2016). Distinct Roles of Parvalbumin- and Somatostatin-Expressing Interneurons in Working Memory. Neuron *92*, 902–915.

Lam, Y.-W., and Sherman, S.M. (2011). Functional Organization of the Thalamic Input to the Thalamic Reticular Nucleus. J. Neurosci. *31*, 6791.

Lee, S.-H., Govindaiah, G., and Cox, C.L. (2007). Heterogeneity of firing properties among rat thalamic reticular nucleus neurons. J. Physiol. *582*, 195–208.

Lein, E.S., Hawrylycz, M.J., Ao, N., Ayres, M., Bensinger, A., Bernard, A., Boe, A.F., Boguski, M.S., Brockway, K.S., Byrnes, E.J., et al. (2007). Genome-wide atlas of gene expression in the adult mouse brain. Nature *445*, 168–176.

Lewis, L.D., Voigts, J., Flores, F.J., Schmitt, L.I., Wilson, M.A., Halassa, M.M., and Brown, E.N. (2015). Thalamic reticular nucleus induces fast and local modulation of arousal state. eLife *4*, e08760.

Liu, X.-B., and Jones, E.G. (1999). Predominance of corticothalamic synaptic inputs to thalamic reticular nucleus neurons in the rat. J. Comp. Neurol. *414*, 67–79.

Macdonald, K.D., Fifkova, E., Jones, M.S., and Barth, D.S. (1998). Focal Stimulation of the Thalamic Reticular Nucleus Induces Focal Gamma Waves in Cortex. J. Neurophysiol. *79*, 474.

Makinson, C.D., Tanaka, B.S., Sorokin, J.M., Wong, J.C., Christian, C.A., Goldin, A.L., Escayg, A., and Huguenard, J.R. (2017). Regulation of Thalamic and Cortical Network Synchrony by Scn8a. Neuron *93*, 1165–1179.e6.

Malafosee, A. (1994). Thalamocortical rhythm generation in vitro. In Idiopathic Generalized Epilepsies: Clinical, Experimental and Genetic Aspects, (Libbey, John & Company, Limited), p. 129.

Paz, J.T., and Huguenard, J.R. (2015). Microcircuits and their interactions in epilepsy: is the focus out of focus? Nat Neurosci *18*, 351–359.

Paz, J.T., Christian, C.A., Parada, I., Prince, D.A., and Huguenard, J.R. (2010). Focal Cortical Infarcts Alter Intrinsic Excitability and Synaptic Excitation in the Reticular Thalamic Nucleus. J. Neurosci. *30*, 5465.

Paz, J.T., Bryant, A.S., Peng, K., Fenno, L., Yizhar, O., Frankel, W.N., Deisseroth, K., and Huguenard, J.R. (2011b). A new mode of corticothalamic transmission revealed in the Gria4(-/-) model of absence epilepsy. Nat. Neurosci. *14*, 1167–1173.

Paz, J.T., Davidson, T., Freschette, E., Delord, B., Prada, I., Peng, K., Deisseroth, K., and Huguenard, J.R. (2013). Closed-loop optogenetic control of thalamus as a new tool to interrupt seizures after cortical injury. Nat. Neurosci. *16*, 64–70.

Phillips, E.A., and Hasenstaub, A.R. (2016). Asymmetric effects of activating and inactivating cortical interneurons. eLife *5*, e18383.

Pinault, D., and Deschˆnes, M. (1998). Projection and Innervation Patterns of Individual Thalamic Reticular Axons in the Thalamus of the Adult Rat: A Three-dimensional, Graphic, and Morphometric Analysis. J. Comp. Neurol. *2*, 180–203.

Reinhold, K., Lien, A.D., and Scanziani, M. (2015). Distinct recurrent versus afferent dynamics in cortical visual processing. Nat Neurosci *18*, 1789–1797.

Saalmann, Y.B. (2014). Intralaminar and medial thalamic influence on cortical synchrony, information transmission and cognition. Front. Syst. Neurosci. *8*, 83.

Sherman, S.M. (2001a). A wake-up call from the thalamus. Nat Neurosci *4*, 344–346.

Sherman, S.M. (2001b). Tonic and burst firing: dual modes of thalamocortical relay. Trends Neurosci. *24*, 122–126.

Slaght, S.J., Leresche, N., Deniau, J.-M., Crunelli, V., and Charpier, S. (2002). Activity of Thalamic Reticular Neurons during Spontaneous Genetically Determined Spike and Wave Discharges. J. Neurosci. *22*, 2323.

Sohal, V.S., Huntsman, M.M., and Huguenard, J.R. (2000). Reciprocal Inhibitory Connections Regulate the Spatiotemporal Properties of Intrathalamic Oscillations. J. Neurosci. *20*, 1735.

Sohal, V.S., Zhang, F., Yizhar, O., and Deisseroth, K. (2009). Parvalbumin neurons and gamma rhythms enhance cortical circuit performance. Nature *459*, 698–702.

Steriade, M. (2005). Sleep, epilepsy and thalamic reticular inhibitory neurons. INMEDTINS Spec. Issue Mult. Facets GABAergic Synap. *28*, 317–324.

Steriade, M., Domich, L., Oakson, G., and Deschenes, M. (1987). The deafferented reticular thalamic nucleus generates spindle rhythmicity. J. Neurophysiol. *57*, 260.

Wall, N.R., Wickersham, I.R., Cetin, A., De La Parra, M., and Callaway, E.M. (2010). Monosynaptic circuit tracing in vivo through Cre-dependent targeting and complementation of modified rabies virus. Proc. Natl. Acad. Sci. *107*, 21848–21853.

Wall, N.R., De La Parra, M., Callaway, E.M., and Kreitzer, A.C. (2013). Differential innervation of direct- and indirect-pathway striatal projection neurons. Neuron *79*, 347–360.

Wells, M.F., Wimmer, R.D., Schmitt, L.I., Feng, G., and Halassa, M.M. (2016). Thalamic reticular impairment underlies attention deficit in Ptchd1Y/− mice. Nature *532*, 58–63.

Williamson, A.M., Ohara, P.T., and Ralston III, H.J. (1993). Electron microscopic evidence that cortical terminals make direct contact onto cells of the thalamic reticular nucleus in the monkey. Brain Res. *631*, 175–179.

Wilson, N.R., Runyan, C.A., Wang, F.L., and Sur, M. (2012). Division and subtraction by distinct cortical inhibitory networks in vivo. Nature *488*, 343–348.

Zhang, Z.-W., Zak, J.D., and Liu, H. (2010). MeCP2 Is Required for Normal Development of GABAergic Circuits in the Thalamus. J. Neurophysiol. *103*, 2470.

Zikopoulos, B., and Barbas, H. (2012). Pathways for Emotions and Attention Converge on the Thalamic Reticular Nucleus in Primates. J. Neurosci. *32*, 5338.

Figures

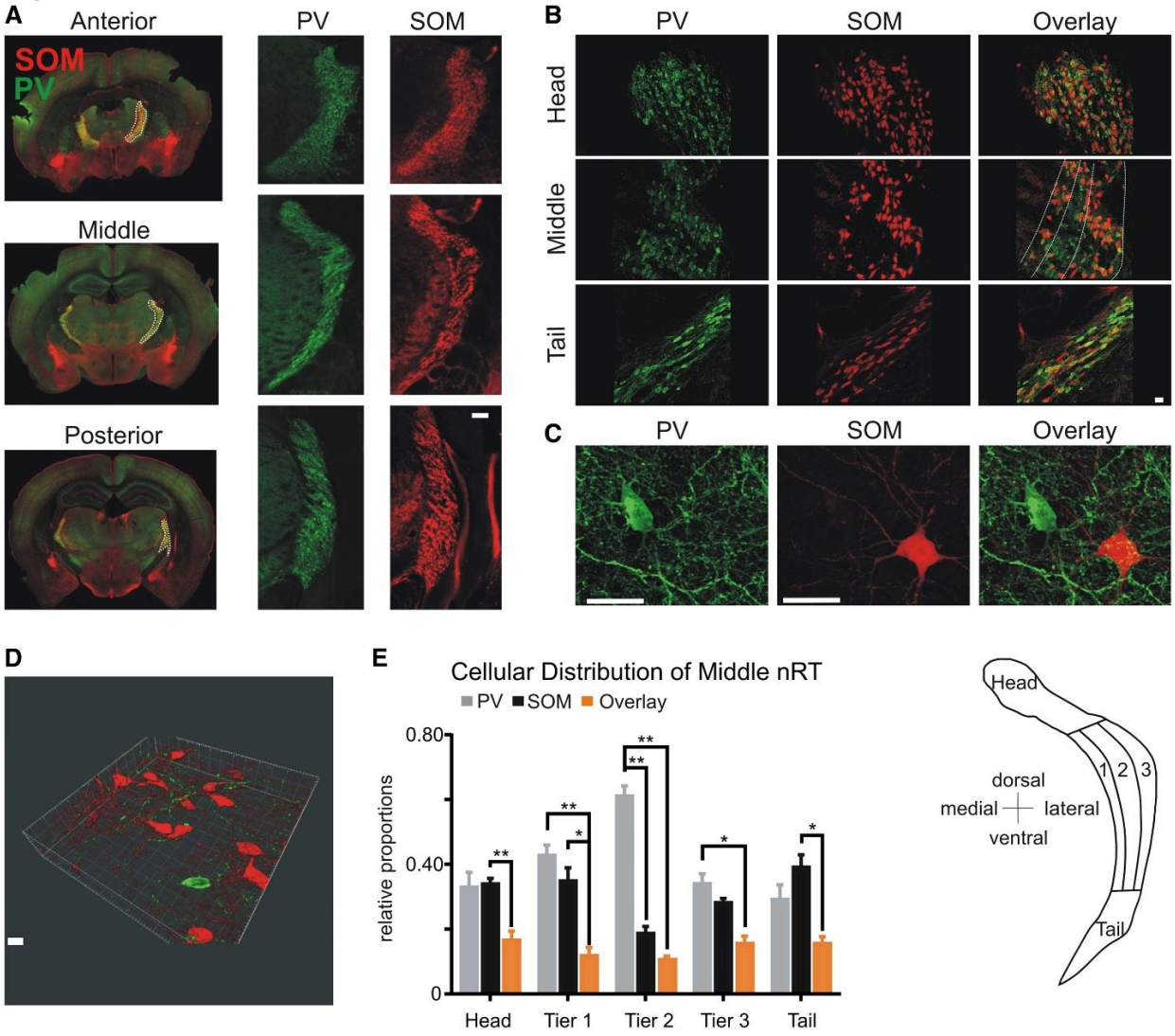

Figure 2.1. PV and SOM Neurons Segregate Differentially across nRT Boundaries

A) Representative composite images (individual images, 10×) of coronal brain sections from SOM-Ai14 (red) mice labeled with PV-antibody (green). The sections span anterior, middle, and posterior portions of the nRT. On the left are full coronal slices and the nRT outlined in white. On the right are higher-magnification images of the nRT. Scale bar, 500 μm.

B) Confocal images (20×) of the head, middle, and tail portions of the somatosensory nRT. Scale bar, 20 μm. The middle portion is divided into tiers by white lines.

C) High magnification confocal images showing examples of non-overlapping populations of individual neurons labeled for either PV (green) or SOM (red). Scale bar, 20 μm.

D) Confocal z stack (25 slices, depth: 9.32 μm, 0.37 μm interval) showing a population of non-overlapping red SOM cells and a single green PV cell. Scale bar, 20 μm.

E) Left, quantification of nRT neurons expressing markers for PV (gray), SOM (black), or both (overlay, orange).

The data represent mean ± SEM analyzed with a Mann-Whitney test and $\alpha = 0.05$ ($*p < 0.05$, $**p < 0.01$, and $***p < 0.001$). The analysis includes four mice (n = 2 slices per mouse, 1 image per nRT region). On the right are divisions of nRT into "head", "middle", and "tail". The middle was divided into tiers from most medial (1), central (2), and most lateral (3) according to Lam and Sherman (2011) and Pinault and Deschênes (1998). nRT, nuclear reticular thalamus

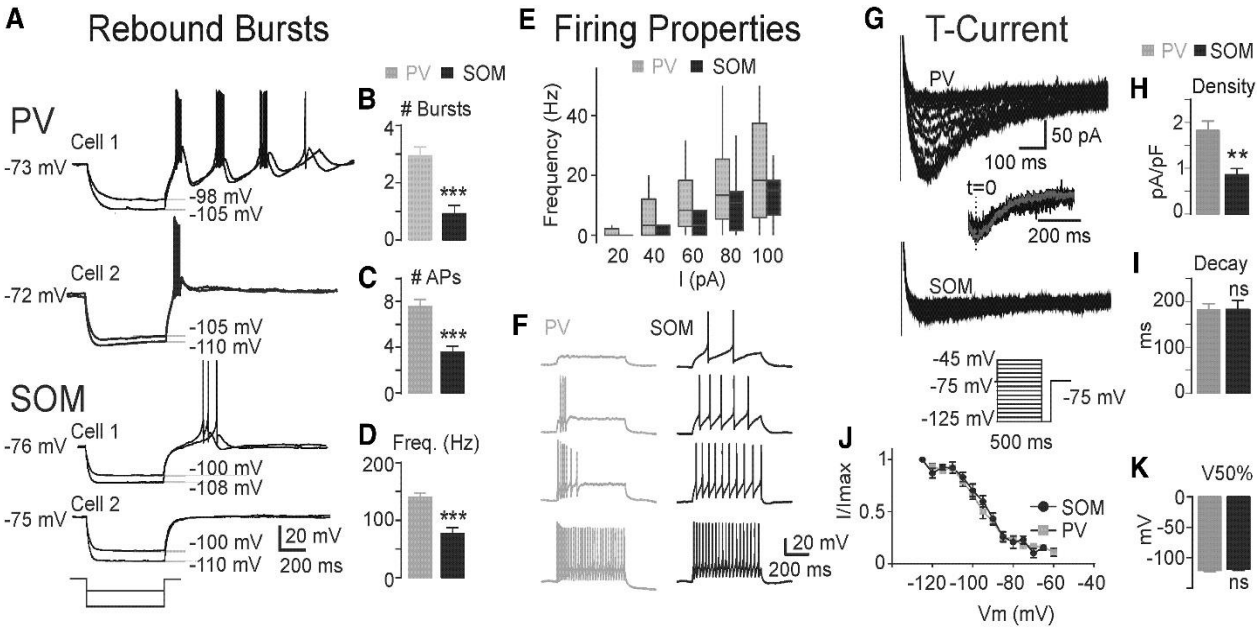

Figure 2.2. PV and SOM Neurons in nRT Exhibit Distinct Firing Properties

(A–D) Data from 14 PV cells from four mice and 16 SOM cells from eight mice.

A) Representative traces showing that PV (top two traces), but not SOM, neurons (bottom two traces) exhibit strong post-inhibitory rebound burst firing upon hyperpolarization induced by −120 and −80 pA current pulses.

B) Number of rebound LTS-type bursts. The data from 14 PV cells with burst and 12 SOM cells with burst are shown.

C) Number of action potentials on first rebound burst.

D) Frequency of action potentials on first rebound burst.

E) Average F-I curve obtained from 14 PV and 16 SOM cells.

F) Representative traces of tonic firing from a PV and a SOM cell. Injected currents: 60 pA, top trace; 80 pA, second trace from top; 100 pA, second trace from bottom; and 120 pA, bottom trace.

G) Representative traces showing T-type calcium current for PV and bursting SOM cells of the nRT. The inset shows the maximal T-currents normalized to the peak (t = 0) to show similar decay kinetics.

H) T-type current density, the maximal amplitude divided by the individual cell capacitance.

I) T-current decay time constant.

J) Normalized current amplitude plotted as a function of the pre-pulse membrane potential best-fitted with a Boltzmann function (R2 = 0.99 for both fits).

K) Half-maximal voltage (V50%) taken from Boltzmann function (data from 11 PV cells from four mice and ten bursting SOM cells from eight mice).

All of the data are represented as mean ± SEM, compared with a Mann-Whitney test and $\alpha = 0.05$ ($*p < 0.05$, $**p < 0.01$, and $***p < 0.001$). See also Figures 10 and 11 and Tables S1 and S2.

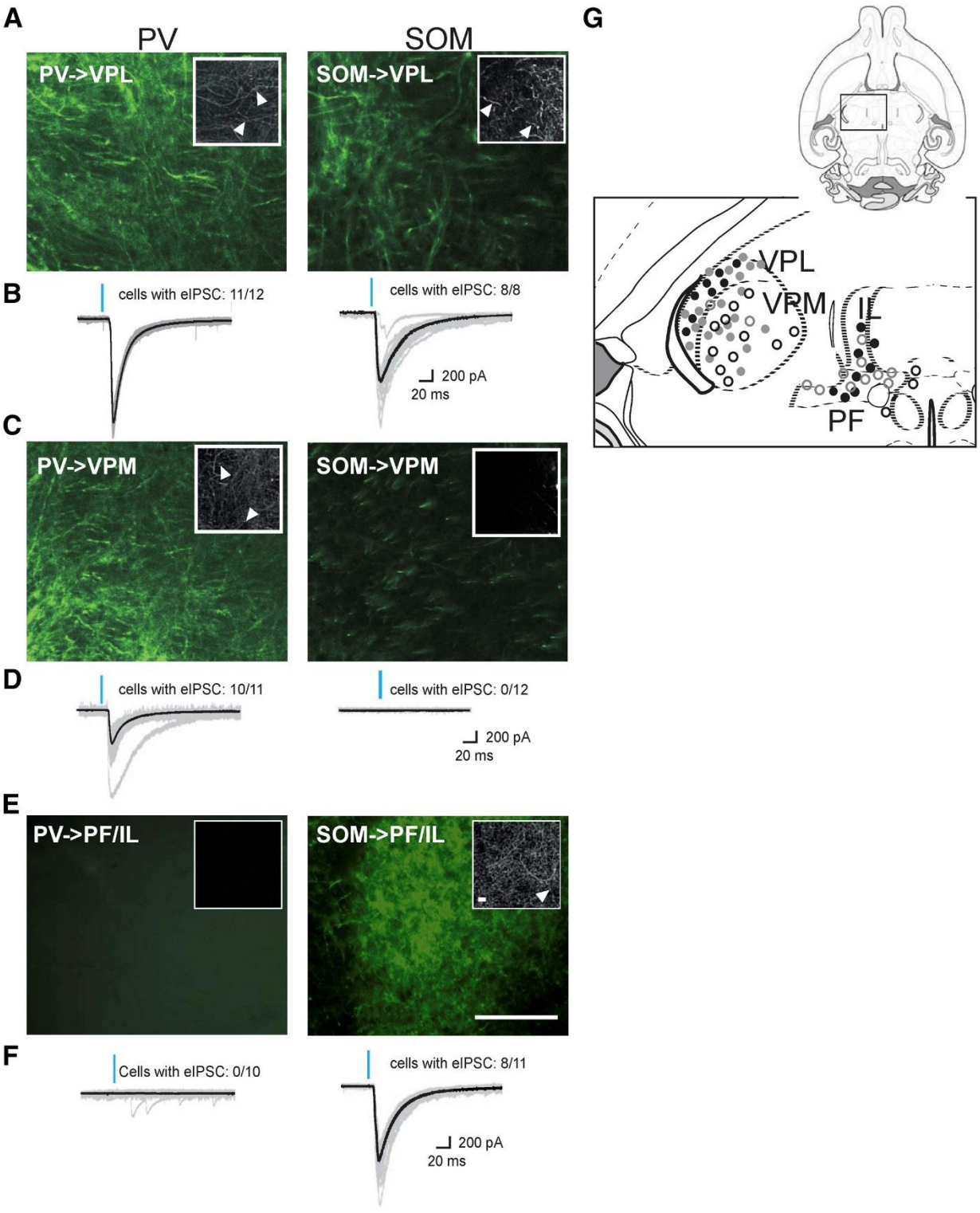

Figure 2.3. PV and SOM Neurons of the nRT Project to Distinct Thalamic Relay Nuclei

(A, C, and E) Examples of eYFP-labeled projections 4 weeks after eYFP injection into the middle nRT of PV-Cre (left) and SOM-Cre (right) mice observed at 20×. The inset shows 100× image showing axonal varicosities (white arrowhead).

(B, D, and F) Examples of evoked inhibitory post-synaptic currents (eIPSCs) recorded from thalamocortical relay cells 4 weeks after ChR2 injection into the middle nRT of PV-Cre (left) and SOM-Cre (right) mice (age of injection: P30). eIPSCs were evoked by placing optical fiber proximal to the patched cell and activating 450 nm laser for 5 ms.

A) Labeling showing eYFP expressing axons and axonal varicosities (inset) in VPL of both PV-Cre and SOM-Cre animals. The section imaged was located 1 mm posterior to bregma.
B) eIPSC were obtained from patching VPL cells in PV-Cre (cells with eIPSCs: 11/12) and SOM-Cre (cells with eIPSCs: 8/8) mice.
C) Labeling showing eYFP-expressing axons and axonal varicosities (inset) in VPM of PV-Cre, but not SOM-Cre, animals. The section imaged was located 1 mm posterior to bregma.
D) eIPSC was obtained from patching VPM cells in PV-Cre (10/11 cells), but not SOM-Cre (0/12 cells), animals.
E) Labeling showing eYFP expressing axons and axonal varicosities (inset) in PF/intralaminar of SOM-Cre, but not PV-Cre, animals. The section imaged was located 1 mm posterior to bregma.
F) eIPSC was obtained from patching PF/intralaminar cells in SOM-Cre (8/11), but not PV-Cre (0/10), animals.
G) Summary diagram showing location of recorded cells. Grey circles, cells from PV-Cre animals; black circles, cells from SOM-Cre animals; full circles, locations with eIPSCs; empty circles, locations without eIPSCs.

Depicted images represent the expression pattern observed in seven injected PV-Cre and seven SOM-Cre animals. eIPSC recordings were obtained from three PV-Cre and three SOM-Cre animals. Injections of the nRT all targeted “middle” nRT at 1.3 posterior from bregma. eIPSC, evoked inhibitory post-synaptic

currents; IL, intralaminar nuclei; PF, parafascicular; VPL, ventroposterolateral; VPM, ventroposteromedial. Large scale bar, 100 μm; inset scale bar, 10 μm. See also Figure 11.

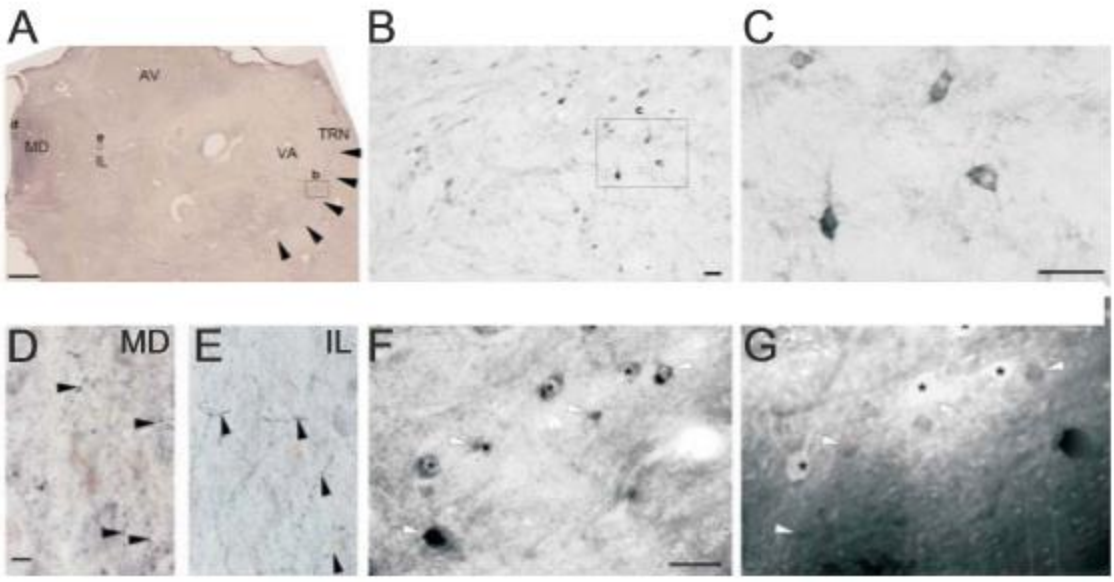

Figure 2.4. SOM cells in the Human nRT and SOM Projections to Higher-Order Thalamic Nuclei

A) Coronal section of the human thalamus at an anterior level (black arrowhead, nRT; small rectangles, position of the respective higher power images).

B) SOM cells in the human nRT. Note the more scattered distribution of the neurons relative to the rodent condition due to the larger number of crossing fiber bundles.

C) High-power images of SOM neurons displaying variable soma shape.

D–E) Varicose SOM axons in the higher-order mediodorsal (D) and intralaminar (E) nuclei (black arrowheads).

F–G) Some cells express only SOM (white arrowheads). SOM can co-localize with PV in certain nRT cells (asterisks). Scale bars: A, 1 mm; B, D–E, 50 µm; C, 25 µm; F–G, 20 µm. AV, anteroventral; IL, intralaminar; MD, midline; nRT, nuclear reticular thalamus; VA, ventral anterior thalamic nuclei.

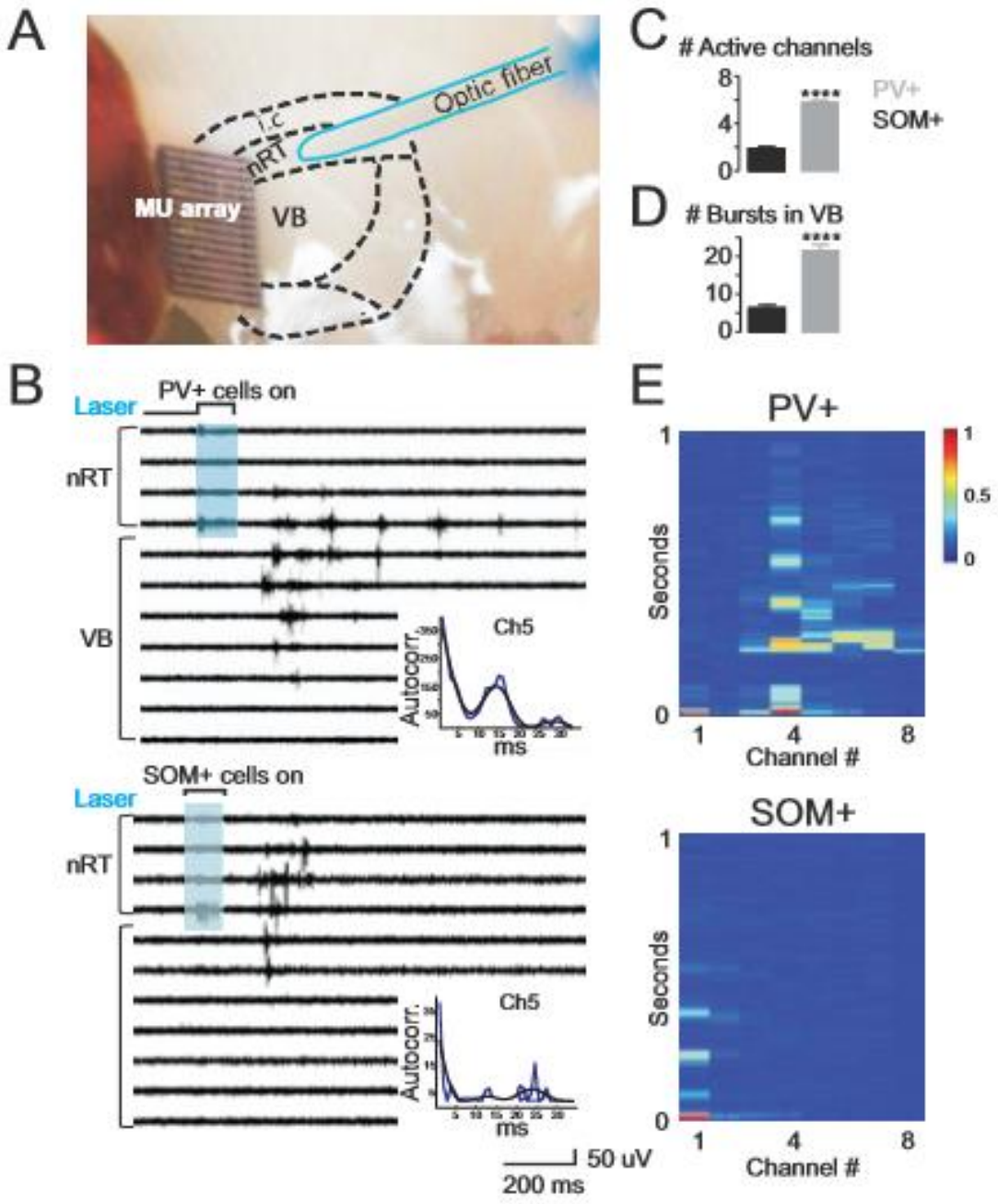

Figure 2.5. Thalamic Circuit Oscillations Evoked by Activation of PV or SOM Neurons in Thalamic Slices

A) Schematic of setup for thalamic oscillation experiments. Multiunit (MU) array is placed across the nRT, ventrobasal (VB) thalamus, and midline nuclei (Mid. Nuc.). A 200 µm optic fiber was placed on the nRT, identified by its direct proximity to the white tracts of the internal capsule (i.c).

B) Representative traces of thalamic oscillatory MU activity recorded in nRT and VB evoked by local optogenetic activation of nRT PV (top) or SOM (bottom) neurons in thalamic slices from P30–P40 PV-Cre and SOM-Cre mice. Instantaneous firing induced by optical stimulation was similar in PV and SOM mice (PV=385±73Hz, SOM=270±63Hz; $p>0.5$, Mann-Whitney test). Inset: autocorrolegrams derived from peristimulus time histograms for individual response observed in Ch5. Ch5 was chosen, because PV and SOM activation evoked a response in this channel for these slices. Blue line: autocorrelation calculated from data, Black line: smoothened autocorrelation to allow for easier visualization of oscillations.

C) Quantification of number of active channels in VB with an evoked oscillatory response. Location of nRT and VB was visually verified for each recording.

D) Number of total evoked bursts recorded in all VB channels. Data for C and D were analyzed from five sweeps obtained from four PV slices and five SOM slices from three animals per group.

E) Representative rate meters showing the spike firing rate (10 ms bins) obtained from recordings shown in panel B. For clarity, only 1 s-long recordings and eight channels are shown. Channel 1 and Channels 2–8 depict firing rates in nRT and VB, respectively. Note that in PV slices (top), the evoked firing lasts longer and is observed in more channels compared with SOM (bottom) slices. Scale for normalized instantaneous frequency showed to the right of top rate meter that was generated using 10 ms bins. All data represented as mean ± SEM, compared with a Mann-Whitney test and $\alpha=0.05$. ($*p<0.05$, $**p<0.01$, $***p<0.001$).

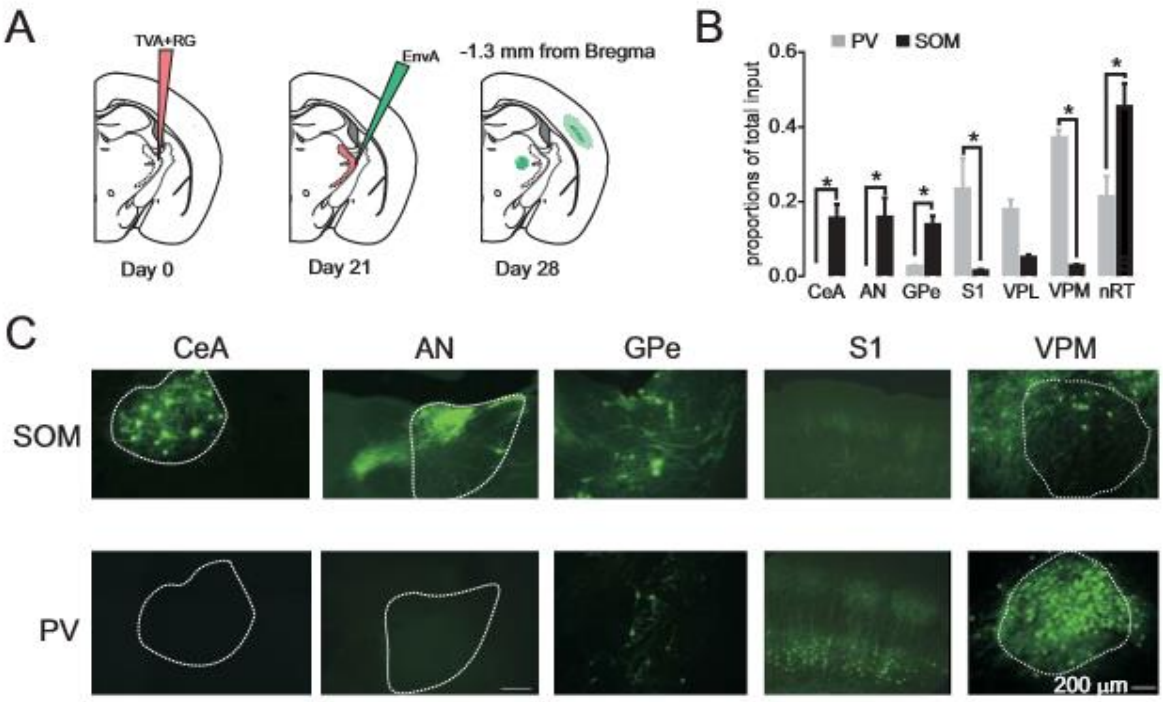

Figure 2.6. PV and SOM Cells Receive Inputs from Distinct Brain Regions

A) Experimental design. SOM-Cre or PV-Cre mice were injected in the middle nRT (1.3 mm posterior to Bregma) with AAV expressing TVA-mCherry and rabies glycoprotein (RG) in a Cre-dependent manner at Day 0, and then with monosynaptic rabies virus (EnvA) containing eGFP that only infects cells expressing TVA and spreads retrogradely to presynaptic cells at day 21. Mice were perfused, and presynaptic populations were labeled with eGFP at day 28.

B) Presynaptic projections at 0.8 mm posterior to Bregma onto SOM cells (left) and PV cells (right) at the anterior nuclei (AN) and somatosensory cortex (S1). Data are represented as mean ± SEM.

C) Top panels show composite images of coronal sections at -0.46mm (left) and -1.2mm (middle) and -1.8mm posterior to Bregma show presynaptic projections onto nRT PV cells in S1: somatosensory cortex, VPM: ventroposteromedial relay thalamus, GPe: globus pallidus, nRT, and CeA: central amygdala. Bottom panels show individual high-magnification images from these sections; scale 200 µm.

D) Top panels show composite images of coronal sections at -0.46mm (left) and and -1.4mm posterior to Bregma show presynaptic projections onto nRT SOM cells in GPe, nRT, and CeA. Bottom panels show individual high-magnification images from these sections; scale 200 μm. These results were observed consistently in three SOM-Cre and five PV-Cre mice. See also Figure 12.

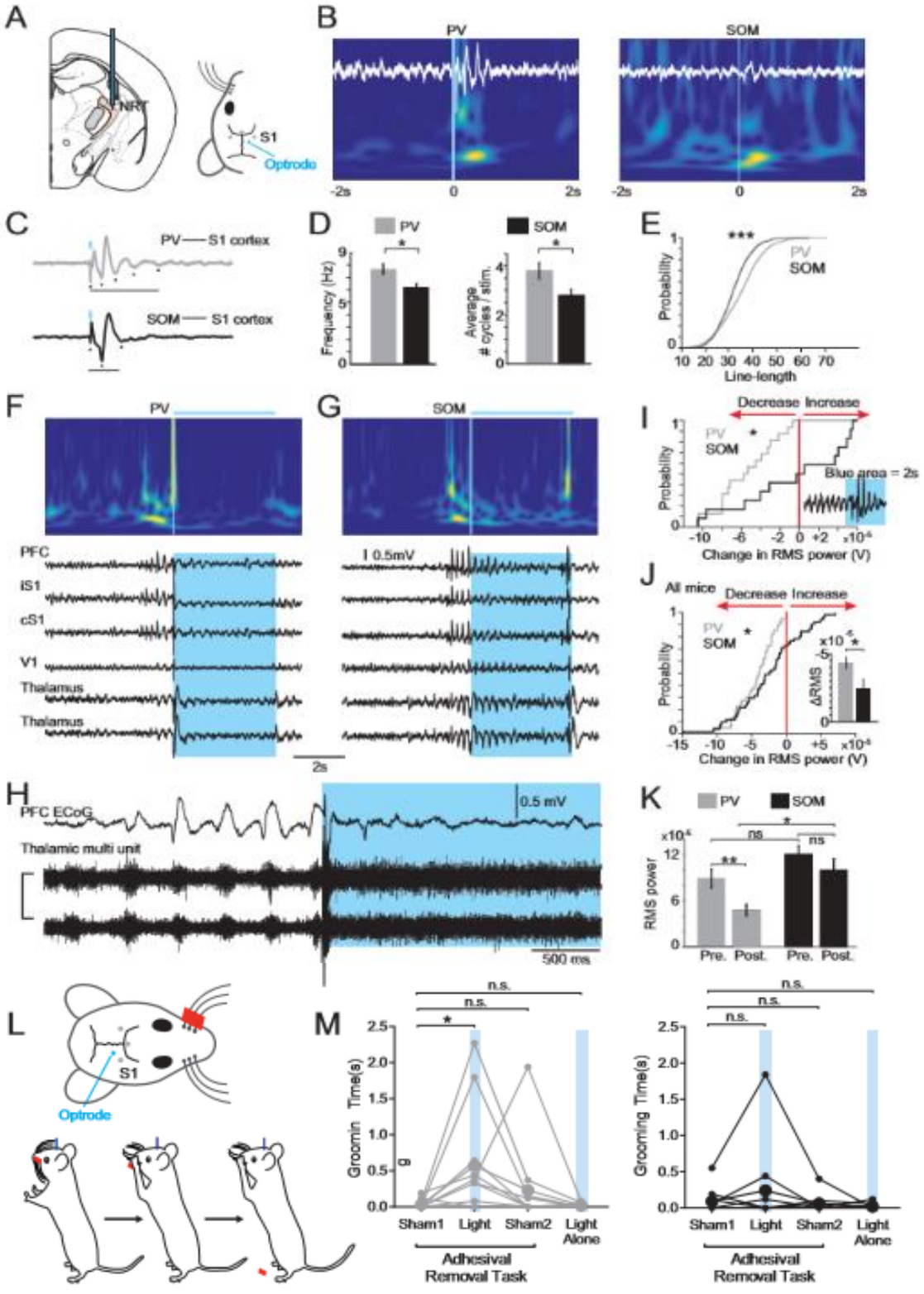

Figure 2.7. Selective Optical Activation of PV and SOM Cells in nRT Modulates Cortical Rhythms

(B–E, M) Data collected from PV-Cre x Ai32 and SOM-Cre x Ai32 mice, age > P30.

(F–K) Data collected from PV-Cre and SOM-Cre mice that expressed ChR2 via viral injections in nRT.

A) Diagram of recording and stimulation locations for *in vivo* experiments. *Left*: Approximate location of an optrode (i.e., optical fiber and two tungsten depth electrodes implanted unilaterally in the nRT. *Right:* Optrode and ECoG recording sites (S1, somatosensory cortex) and optrode on mouse skull.

B) Representative wavelet time-frequency spectrograms and associated single-trial ECoG traces from ipsilateral S1 in PV (*left*) and SOM (*right*) mice. Blue rectangles indicate stimulation of ChR2-expressing PV or SOM neurons (unilateral, single, 20 ms-long light pulse, 450 nm).

C) Representative ECoG traces from S1 cortex averaged per mouse (n=100–300 sweeps/trial). Blue line, stimulation of ChR2-expressing PV or SOM neurons (unilateral, single, 20 ms-long light pulse, 450 nm); black line, duration of oscillatory response in the ECoG.

D) Mean ± SEM of frequency (Hz) and average number of cycles per stimulation (i.e., ECoG spikes); averages from ~200 trials per n=10 PV-Cre and 10 SOM mice, respectively. Mann-Whitney Rank Sum test: *$p<0.05$.

E) Cumulative probability distribution of 7–15 Hz frequency in S1 ECoG, evoked by stimulation of nRT PV vs. SOM stimulation. ***$p<0.001$, two-sample KS test. (PV, 2309 events from n = 10 PV-Cre x Ai32 mice; SOM, 2003 events from n = 10 SOM-Cre x Ai32 mice).

F, G) Representative wavelet time-frequency spectrograms and associated single-trial ECoG traces of optical stimulation during ongoing spike-and-wave seizures in PV (F) and SOM (G) mice. PFC, iS1 (ipsilateral S1), cS1 (contralateral S1), and ipsilateral V1 ECoG example traces are shown, as well as LFP and MU signals from nRT. Blue boxes indicate 4 s epoch of blue light stimulation (450 nm, 15–35 mW).

H) Zoom of MU activity in the thalamus during ongoing spike-and-wave seizures in a PV- mouse. Blue-light mediated activation of ChR2 increases MU activity in thalamus that corresponds to decreased power in the ECoG (blue box).

I) Individual cumulative probability distribution plots of the change in RMS power (post–pre) from a PV (grey) and SOM (black) mouse for all seizure interruption trials within one mouse (PV trials = 16, SOM trials = 12). *Inset* shows an example trace from a SOM in nRT. Light stimulation enhanced an ongoing seizure. *p<0.05, two-sample KS test.

J) Population cumulative probability distribution plots of change in RMS power from PV (n = 4, grey) and SOM (n = 5, black) mice of all seizure interruption trials comparing RMS power 2 s before and after the stimulation. *p<0.05, two-sample KS test. *Inset*, mean ± SEM of change in RMS power shown in J. *p<0.05, Mann-Whitney Rank Sum.

K) RMS power 2 s before and after light stimulation for PV (grey) and SOM (black) mice. *p<0.05, Mann-Whitney Rank Sum Test, n.s. p>0.1.

M) Schematic of the adhesive removal task showing placement of tape contralateral to the optical stimulation of nRT and sequence of behavior during the task: 1) attachment of the tape to the left mystacial pad, 2) contact with tape, 3) and additional grooming of the mystacial area once tape is removed.

N) Comparison of time (s) spent grooming after removing adhesive during sham, light stimulation, or light alone (not during adhesive removal task) between PV (n = 10) and SOM (n = 11) mice. Analysis with a two-way mixed-model ANOVA shows a significant effect of treatment $F(3, 57) = 4.261$, $p = 0.0088$, and no significant effects for genotype or interaction between genotype and treatment. Post hoc multiple comparison tests (Sidak's, 6 comparisons per family) show a significant effect of treatment only in sham1 vs. light (*p<0.05) in the PV cohort. Note: PV and

SOM mice performed comparably for contact and response time across all treatment conditions (data not shown). See also Figure 13.

Supplemental Figures

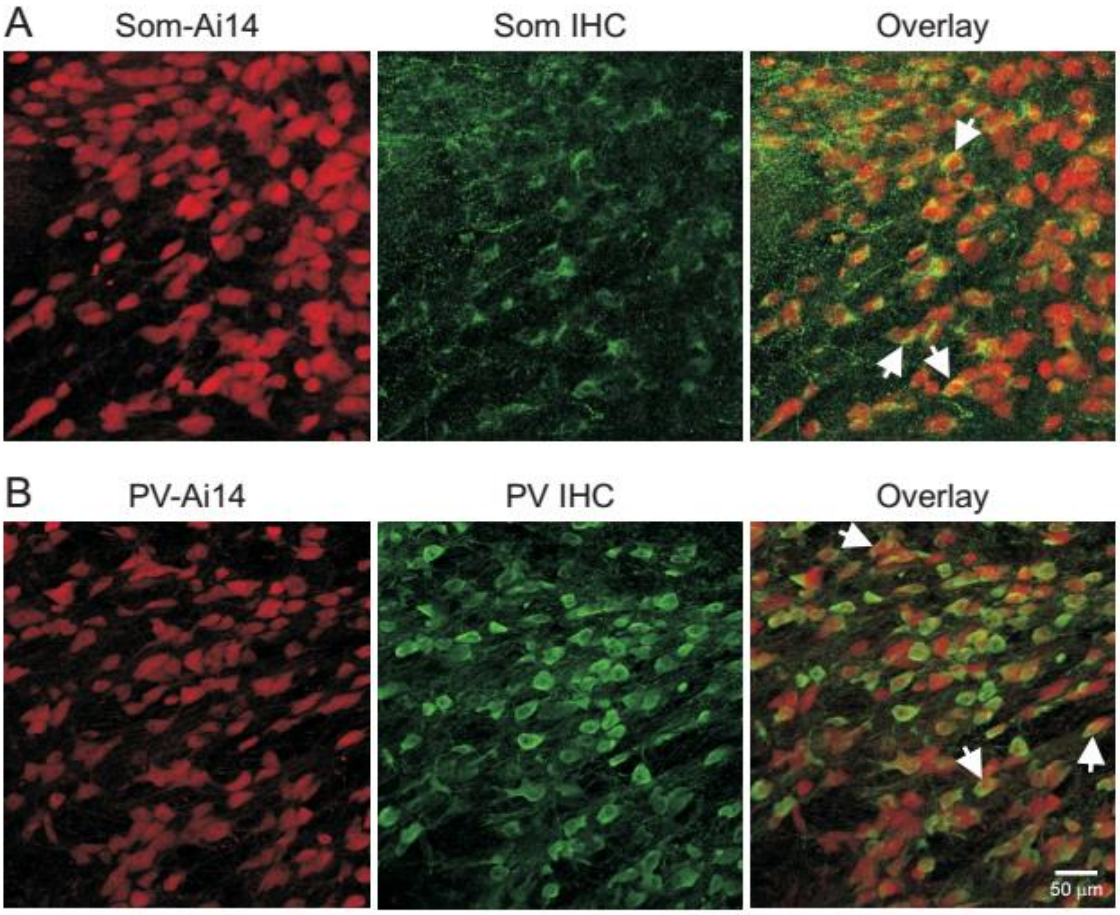

Figure 2.8. TdTomato from SOM and PV-Cre x Ai-14 animals colocalizes with somatostatin and parvalbumin in the nRT

A) Brain slice from a SOM-Cre x Ai14animal (left). Image of somatostatin stain in green (middle). Image overlaying red and green showing co-labeling of red and green (arrowheads). Scale bar, 50 µm. For the SOM-Cre animals, the percentage of Cre- targeted neurons that showed SOM immunofluorescence (specificity) was 90±1%, and the percentage of SOM-immunolabeled cells that were positive for Cre (efficiency) was 98±1%.

B) Brain slice from a PV-Cre x Ai14 animal (left). Image of parvalbumin stain in green (middle). Image overlaying red and green showing co-labeling of red and green (arrowheads). Scale bar, 50

μm. For the PV-Cre animals, the percentage of Cre-targeted neurons that showed PV immunofluorescence was 92± 3% and the percentage of PV-labeled cells that were positive for Cre was 97±1%.

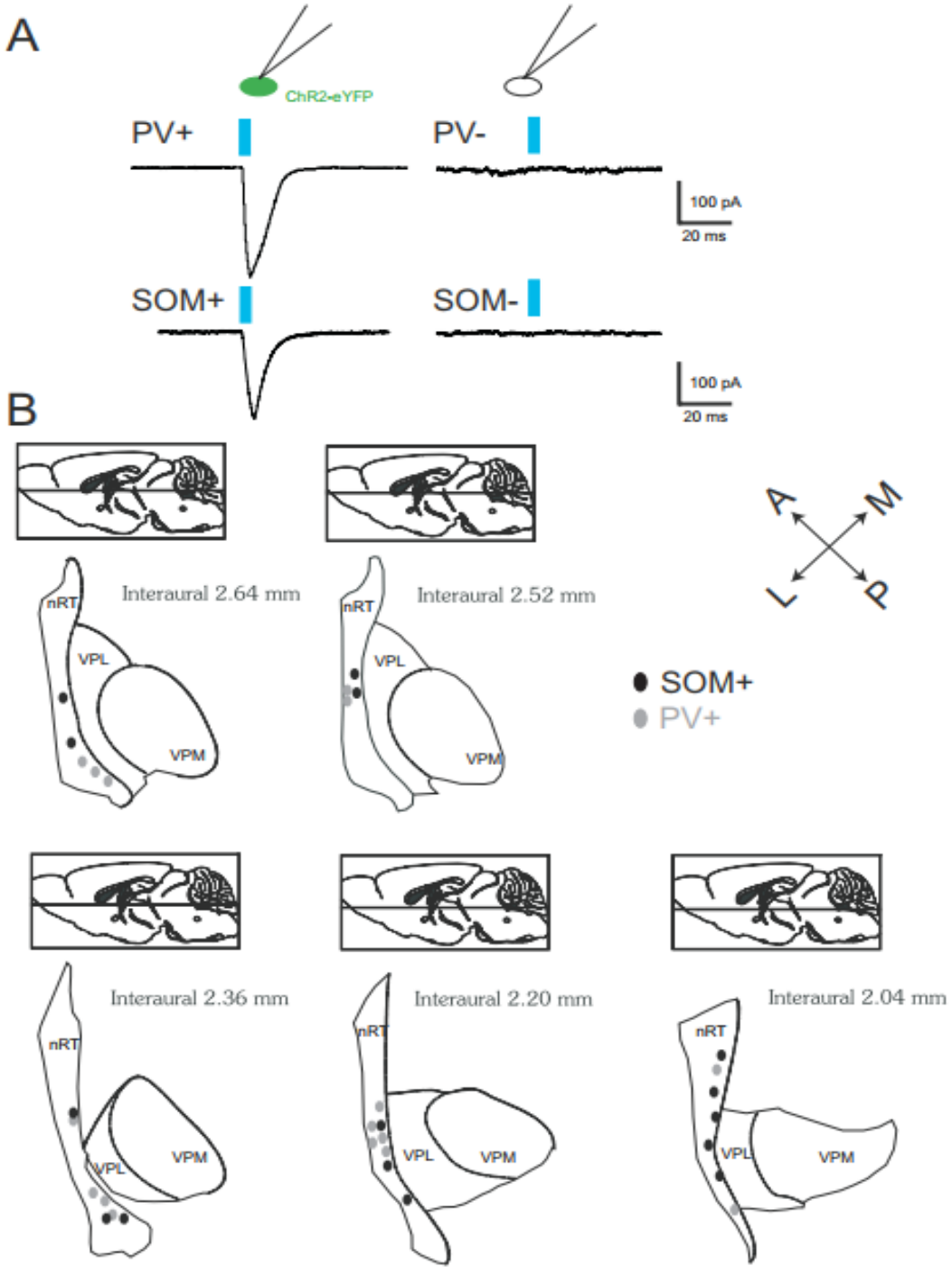

Figure 2.9. Identification of Recorded PV and SOM Neurons in nRT

A. PV or SOM cells were identified according to their activation with blue light (450 nm, see direct ChR2 current evoked with blue light in "+" but not "-" cells) in thalamic slices from PV-Cre x Ai32 and SOM-Cre x Ai32 mice, respectively.

B. Summary diagram showing the location of recorded cells in the SOM-Cre x Ai32 and PV-Cre x Ai32 animals used for intrinsic property analysis.

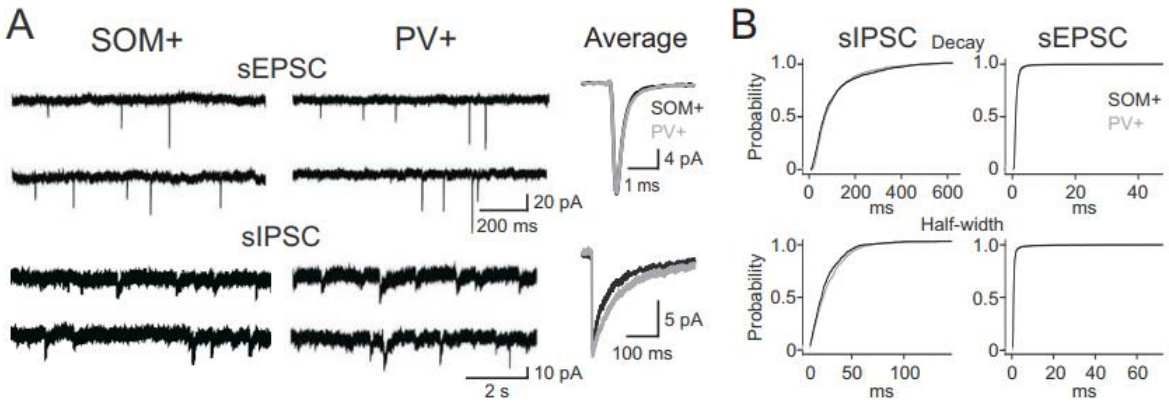

Figure 2.10. Spontaneous Excitatory and Inhibitory Synaptic Currents in PV and SOM

A) Left: Representative traces of spontaneous excitatory postsynaptic currents (sEPSC) (top) and spontaneous inhibitory postsynaptic currents (sIPSC) (bottom) in SOM (left) and PV cells (right). Right: Representative average sEPSC (top) and sIPSC (bottom) traces taken from single cell recordings.

B) Cumulative probability distributions for decay tau and half-width of sEPSCs (right) and sIPSCs (left). Cumulative probability distributions and KS-test p-values were generated using the bootstrap method with 1000 iterations from 17 PV and 10 SOM cells using 80 events/cell for sEPSCs per iteration (three mice for each group) and 30 events/cell for sIPSCs from 12 PV and 8 SOM cells (three mice for SOM group and five mice for PV group). The probability distributions were similar between SOM and PV neurons ($p>0.1$ for all the parameters).

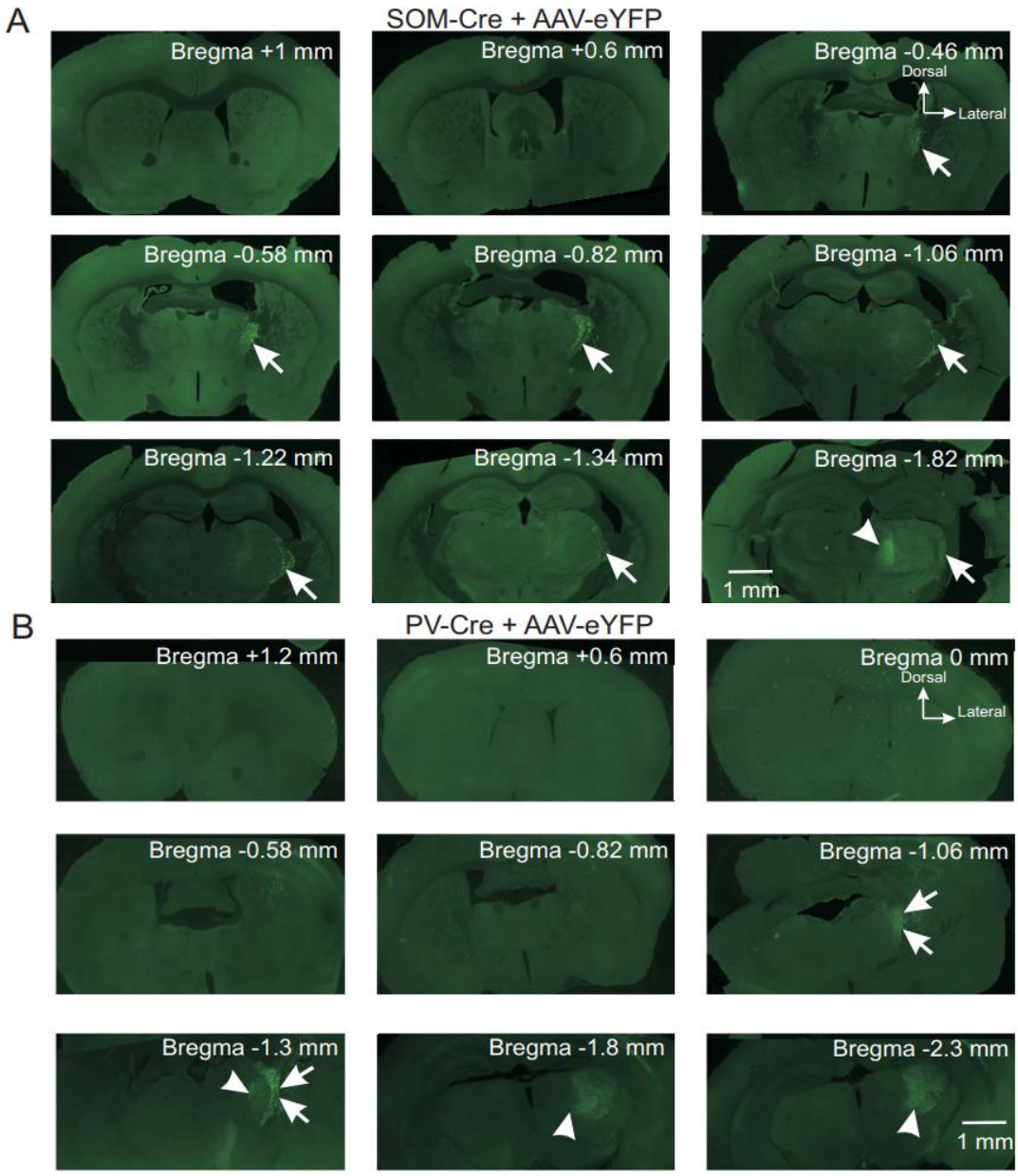

Figure 2.11. nRT Stereotaxic Injection of AAV-DIO-ChR2-eYFP in SOM- and PV-Cre Mice Results in Specific Expression of eYFP in nRT cells (arrows) and axons (arrowheads)

A) Images of coronal brain sections taken from a SOM-Cre mouse that received two 200 nl nRT stereotaxic injections of AAV-DIO-ChR2- eYFP (see Experimental Procedures for injection coordinates); mouse brain was perfused 4 weeks after viral injection in nRT.

B) Images of coronal brain sections taken from a PV-Cre mouse that received two 200 nl nRT stereotaxic injection of AAV-DIO-ChR2- eYFP; mouse brain was perfused 4 weeks after viral injection in nRT. Viruses were only injected in middle sections of the nRT (1.3 mm posterior to Bregma). Arrows indicate eYFP+ cell bodies, arrowheads indicate eYFP+ fibers. The depicted results were found in 4 PV-Cre and 4 SOM-Cre mice. In all mice, SOM eYFP+ fibers were observed mainly in intralaminar nuclei whereas the PV eYFP+ fibers were observed mainly in VB and Po. The images were rotated for easier comparison and the edges of the canvas filled.

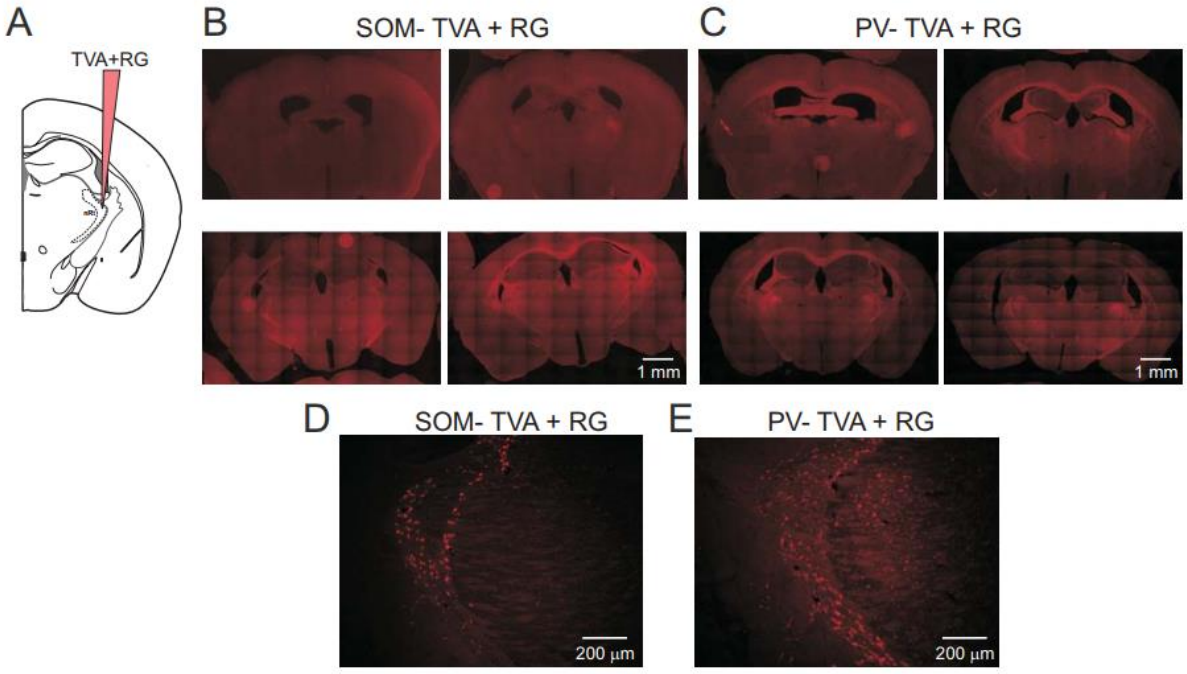

Figure 2.12. nRT Stereotaxic Injection of TVA-mCherry + RG viruses in SOM and PV Cre Mice Results in Specific Expression in nRT Cells and Axons

A) Experimental design: SOM-Cre or PV-Cre mice were injected in the middle nRT (1.3 mm posterior to Bregma, see Experimental Procedures for details) with AAV expressing TVA-mCherry and rabies glycoprotein (RG) in a Cre-dependent manner.

B) Representative images of coronal brain sections taken from a SOM-Cre mouse that received two 100 nl nRT stereotaxic injections of viral constructs containing TVA-Cherry + RG; mouse brains perfused 21 days after viral injection in nRT.

C) Representative images of coronal brain sections taken from a PV-Cre mouse that received double 100 nl nRT stereotaxic injection of viral constructs containing TVA-Cherry + RG; mouse brains perfused 4–6 weeks after viral injection in nRT.

D) Higher magnification image from the SOM-Cre mouse shows mCherry expression in nRT.

E) Higher magnification image from the PV-Cre mosue shows mCherry expression in nRT and a minor expression in VPM. Notably, the minor staining in VPM did not affect the results depicted

in Figure 6, given that in all mice the same major input region was found to be S1 Barrel cortex and VPM which are known to project onto nRT from numerous previous studies (see text for details). The viral constructs were only injected in middle sections of the nRT (1.3 mm posterior to Bregma).

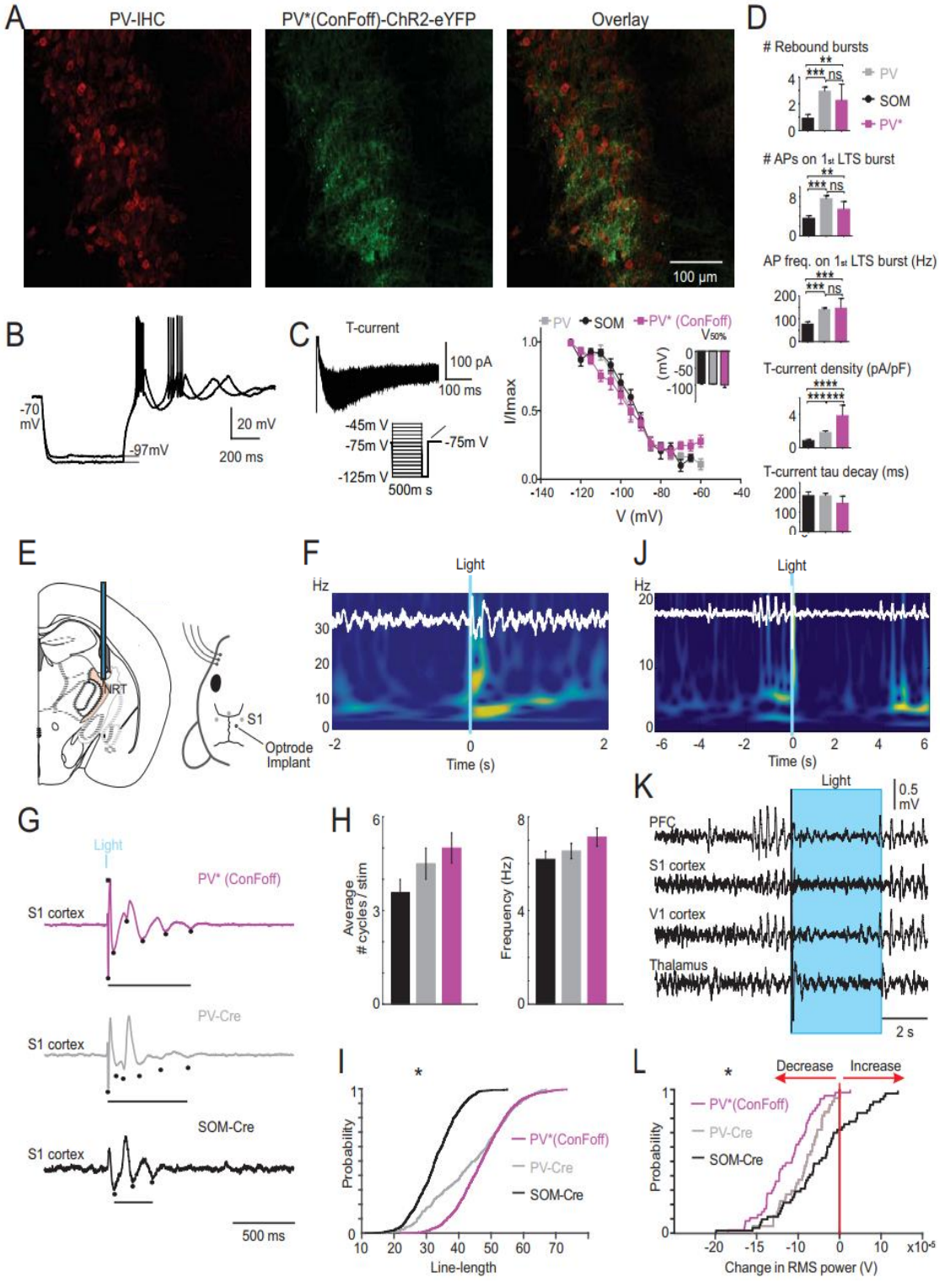

Figure 2.13. Validation of INTRSECT approach

A) Brain slice from a Cre/Flp animal that received two 200 nl nRT stereotaxic injections of CreON/FlpOFF-ChR2-eYFP (middle) and has been stained for parvalbumin in red (left). Image overlaying red and green showing colabeling of red and green image of somatostatin stain in green (middle). Scale bar, 25 µm.

B) Representative traces showing that PV* cells expressing ChR2, exhibit strong post-inhibitory rebound burst firing upon hyperpolarization, induced by -120 and -80 pA current pulses.

C) Left, Representative traces showing T-type calcium current obtained with the SSI protocol for PV* cells of the nRT, Right, Normalized current amplitude plotted as a function of the pre-pulse membrane potential that is best-fitted with a Boltzmann function (R2=0.99 for both fits). Inset, Half-maximal voltage (V50%) taken from Boltzmann function (data from 11 PV cells from 4 mice, 10 SOM cells from 8 mice and 9 PV* cells taken from 3 mice).

D) Comparison of intrinsic properties between PV-Cre, SOM-Cre, and PV* mice: number of rebound bursts, number of action potentials on first rebound burst, frequency of action potentials on first rebound burst, t-type current density, t-current decay time constant. All data in D are represented as mean ± SEM, compared using a Mann-Whitney test, with α=0.05. (*p<0.05, **p<0.01, ***p<0.001). Notably, the resting membrane potential was similar in PV and PV* cells (PV: -70.2 ± 2.7 mV, n= 12 cells from 4 mice; PV*: -73.4 ± 2.1 mV, n=10 cells from 3 mice; p=0.4; Mann Whitney test). The action potential properties were similar in PV and PV* cells including threshold (PV: -50.3 ± 0.9 mV, n= 12 cells from 4 mice; PV*: -52.4 ± 1.7 mV, n=10 cells from 3 mice; p=0..3, Mann Whitney test) and duration (PV: 1.4 ± 0.1 ms, n=12 cells from 4 mice; PV*: 1.4 ± 0.1, n=10 cells from 3 mice; p=0.9; Mann Whitney test). The quantification was not included in the figure for clarity.

E) Diagram of recording and stimulation locations for in vivo experiments. Left: Approximate location of an optrode (i.e., optical fiber and two tungsten depth electrodes implanted

unilaterally in the nRT. Right: Optrode and ECoG recording sites (S1 – somatosensory cortex) and optrode on mouse skull.

F) Representative wavelet time-frequency spectrograms and associated singletrial ECoG traces from ipsilateral S1 in PV* mice. Blue rectangles indicate stimulation of ChR2-expressing PV* neurons (unilateral, single, 20 ms-long light pulse, 450 nm).

G) Representative ECoG traces averaged per mouse (n=100–300 sweeps/trial) in PV* (purple), PV-Cre (grey), and SOM-Cre (black) mice. Blue line, stimulation of ChR2-expressing neurons (unilateral, single, 20 ms-long light pulse, 450 nm); black line, duration of the oscillatory response in the ECoG.

H) Mean ± SEM of cycle number and frequency (Hz) per evoked oscillation in S1 cortex (averages from 1400 trials per n=6 ConFoff mice, 400 trials per n=2 PVCre mice, 1000 trials per n=5 Som-Cre mice).

I) Cumulative probability distribution of the line-length of the 7–15 Hz frequency in S1 ECoG, evoked by stimulation of nRT (PV* vs. PV vs. SOM stimulation. ***p<.001, two-sample KS test).

J) Representative wavelet time-frequency spectrogram and associated single-trial ECoG traces showing optical stimulation during an ongoing spike-and-wave seizure recorded from PV* mice.

K) Corresponding and additional ECoG traces from the wavelet shown in J. ECoG traces from PFC, ipsilateral S1 cortex, and ipsilateral V1 cortex are shown, with LFP and MU from nRT. Blue box denotes duration of light stimulation.

L) Population cumulative probability distribution plots of change in RMS power (post-pre) from PV* (n = 6, purple), PV-Cre (n = 4, grey) and SOM-Cre (n = 5, black) mice for all seizure interruption trials comparing RMS power 2 s before and 2 s after the stimulation (PV vs. SOM, PV vs. PV*. *p<.05. PV* vs SOM, ***p<.001).

Table 2.1. Passive and active electric membrane properties of PV+ and SOM+ neurons in nRT.

Table 1: Passive and active electric membrane properties of PV+ and SOM+ neurons in nRT										
	Cm (pF)	**Vm (mV)**	**Ri (MOhms)**	**Tau (ms)**	**AP thr. (mV)**	**AP dur. (ms)**	**Rheobase**	**Slope**	**# Cells**	**# Mice**
PV+	64.1 ±6.12	-70.2 ± 2.7	496.3 ± 55.7	46.6 ± 4.4	-50.3 ± 0.9	1.44 ± 0.09	46.7 ± 8.6	0.38 ± 0.05	12	4
SOM+	59.3 ± 5.5	-71.4 ± 3.0	494.8 ± 64.2	38.1 ± 3.8	-51.4 ± 1.1	1.54 ± 0.09	67.1 ± 9.0	0.4 ± 0.04	18	8
p-value	0.74	0.92	0.69	0.07	0.82	0.94	p>0.05	p>0.05		

Data represented as mean ± SEM, compared using Mann-Whitney test with $\alpha = 0.05$

Table 2.2. Properties of spontaneous excitatory and inhibitory postsynaptic currents in PV+ and SOM+ cells

Table 2. Properties of spontaneous excitatory and inhibitory postsynaptic currents in PV+ and SOM+ cells									
		Rise (ms)	**Decay Tau (ms)**	**Half Width (ms)**	**Amplitude (pA)**	**Charge (C)**	**Interval (s)**	**# Cells**	**# Mice**
sIPSC	**PV+**	1.5 ± 0.1	92.4 ± 13.5	28.8 ± 1.3	14.1 ± 0.5	234 ± 13.5	2.7 ± 0.5	12	5
	SOM+	1.5 ± 0.1	90.6 ± 28.8	26.5 ± 0.8	15.8 ± 1.6	219 ± 17.6	2.7 ± 0.9	8	3
	p-value	0.53	0.95	0.45	0.71	0.8	0.64		
sEPSC	**PV+**	0.3 ± 0.01	16.6 ± 1.0	1.2 ± 0.1	22.3 ± 1.4	28.6 ± 1.95	0.4 ± 0.1	15	3
	SOM+	0.3 ± 0.01	13.9 ± 1.6	1.3 ± 0.2	19.7 ± 1.2	25.9 ± 1.78	0.5 ± 0.1	10	3
	p-value	0.89	0.17	0.68	0.21	0.24	0.68		

Data represented as mean ± SEM, compared using Mann-Whitney test with $\alpha = 0.05$

Chapter 3 : Potassium current deficit underlies thalamic hyperexcitability and seizures in *SCN1A*-Dravet syndrome

Summary

Dravet syndrome is an incurable, severe form of early-onset epilepsy associated with intractable seizures, developmental delay, autistic features, sleep disorders, and sudden unexpected death in epilepsy (SUDEP). Approximately 80% of patients with this syndrome have a loss-of-function mutation in one allele of the sodium channel gene *SCN1A*, which is mainly expressed in inhibitory neurons. The brain circuits causing seizures in these patients have not been identified, but runaway excitation is thought to result from reduced activity in inhibitory neurons. Here we show that runaway excitation results instead from enhanced activity in the inhibitory reticular thalamus, a region that regulates thalamocortical rhythms and contains intrinsically oscillatory neurons. In a well-established mouse model of the human *SCN1A* mutation, we found that reticular thalamic cells exhibited abnormally high pacemaker burst firing due to reduced SK current, which is conducted by a subfamily of calcium-activated potassium channels that normally limit firing. The thalamus was hyperexcitable in *Scn1a* mutant mice, as indicated by abnormally long evoked circuit oscillations. In vivo, we observed that seizures in *Scn1a* mutant mice exhibit the same EEG signatures as in humans with Dravet syndrome. These cellular abnormalities and seizures were all rescued by enhancing SK currents in the reticular thalamus. Further, optogenetically toggling between burst and tonic firing in thalamic neurons launched and aborted seizures, respectively. Finally, computational modeling and electrophysiology indicate that reticular thalamic hyperexcitability can cause abnormal bursting in relay-thalamocortical nuclei to promote cortical seizure expression. Together these correlational, loss-of-function, and gain-of-function results support a model in which the most common and intractable seizures in Dravet syndrome are caused by a hypoactive SK current that makes the reticular thalamus hyperexcitable. Our study identifies the SK current as a novel therapeutic target in Dravet syndrome.

Introduction

SCN1A gene encodes for the alpha subunit of the voltage-gated sodium channel Nav1.1, which is widely expressed in both the heart and the brain. *SCN1A* is key in regulating cardiac (Auerbach et al., 2013; Kalume et al., 2013) and brain rhythms and its mutations have dramatic consequences on human health. The *SCN1A* gene is one of the most commonly mutated genes associated with epilepsy, including Dravet syndrome (Claes et al., 2001, 2009) – hereafter referred to as DS. This epileptic encephalopathy is characterized by sudden death, autism, cognitive impairment, motor impairments, and sleep disorders. Reduced *Scn1a* in GABAergic cortical and hippocampal inhibitory neurons is thought to reduce action potential (AP) firing and thus network inhibition, leading to runaway excitation (altered excitatory/inhibitory balance) and deadly seizures (Cheah et al., 2012; Dutton et al., 2013; Ogiwara et al., 2007; Tai et al., 2014; Yu et al., 2006). Global knockout of *Scn1a* in parvalbumin and somatostatin neurons increases susceptibility to thermally-induced seizures, while selective knockout in either neuron subtype phenocopies distinct DS neuropsychiatric behavioral phenotypes (Rubinstein et al., 2015). However, the precise molecular and brain circuit mechanisms by which reduced *SCN1A* causes seizures is not known. Uncovering how *SCN1A* mutations hijack the brain function could open the door to developing novel therapeutic strategies.

SCN1A is particularly abundant in the GABAergic nucleus reticularis thalami (nRT) (Papale et al., 2013), known as the "guardian of the gateway" given its role in dynamically modulating interactions between the thalamus and the cerebral cortex (Crick, 1984; Halassa and Acsády, 2016). The *Scn1a*–expressing GABAergic neurons of the nRT are intrinsic oscillators that provide the main source of inhibition onto the excitatory relay thalamus (Gentet and Ulrich, 2003; Houser et al., 1980), positioning them to regulate thalamocortical oscillations, including seizures. Given the abundant expression of *Scn1a* in nRT and the fact that disruptions in nRT are known to correlate with neurological (Makinson et al., 2017; Paz et al., 2010; Slaght et al., 2002) and psychiatric disorders (Ferrarelli and Tononi, 2011; Zhang et al., 2010), we

tested the hypothesis that *Scn1a* deficiency in nRT neurons is causally involved in DS in a well-established mouse model containing a human *Scn1a* mutation (Ogiwara et al., 2007).

Results

Scn1a deficiency leads to thalamic microcircuit hyperexcitability

Interaction between nRT and thalamocortical relay neurons generates rhythmic circuit oscillations. Because nRT neurons express high levels of the *Scn1a* gene, (Papale et al., 2013), we first asked whether the intra-thalamic micro-circuit rhythmogenesis is altered in *Scn1a* DS mice. To address this question, we used horizontal thalamic slice preparations that conserve the connectivity between the nRT and the ventrobasal complex of the somatosensory thalamus (VB) which allow us to assess nRT-VB intra-thalamic network oscillations independent of other structures (i.e., cortex) (Huntsman et al., 1999).

Stimulation of the internal capsule consistently evoked rhythmic oscillatory bursting activity in VB (Figure 1b, left), in the spindle frequency range (~10 Hz), similar to previous studies using electrical stimulation to activate intra-thalamic oscillations (Huntsman et al., 1999; Paz et al., 2011b, 2013) or optogenetic activation *in vivo* (Barthó et al., 2014). Similar stimulations in *Scn1a* DS mice induced more bursts and longer circuit oscillations in the thalamus (Figure 1b, right, and d, e), with the frequency of the circuit oscillations being slower in *Scn1a* DS mice (Figure 1f). These findings show that the nRT-VB microcircuit is hyperexcitable in *Scn1a* DS mice. This finding is surprising given that nRT-VB oscillations require a robust firing in nRT neurons, which we initially expected to be lower in *Scn1a*-deficient mice, as suggested by previous studies (Kalume et al., 2015).

Scn1a deficiency leads to enhanced high-frequency burst firing in nRT neurons

The nRT-VB microcircuit loop regulates rhythm generation, because thalamocortical VB cells fire low-threshold-spike (LTS)-mediated rebound bursts after hyperpolarization induced by nRT GABAergic inputs (Jahnsen and Llinás, 1984). LTS-mediated burst firing confers properties needed for the nRT to generate spindle oscillatory activity in the normal thalamocortical circuit (Bazhenov et al., 2000; Beenhakker and

Huguenard, 2009; Deschenes et al., 1984; Steriade et al., 1987). It is also important for sensory processing (Dang-Vu et al., 2010; Sherman, 2001a, 2001b). To assess whether the nRT-VB thalamic circuit hyperexcitability in *Scn1a* DS mice might be explained by alterations in the electric membrane properties of nRT neurons, we performed patch-clamp whole-cell recordings of nRT neurons.

We measured membrane potential changes in response to a series of intracellular square current pulses (Figure 2a). Only PV-like bursting nRT cells (Clemente-Perez et al., 2017) were used for this study. After similar responses to membrane potential hyperpolarizations, the number of APs within the initial rebound burst was ~1.5x higher in nRT neurons from *Scn1a* DS mice compared with wild-type (WT) littermates (Figure 2a, b). These data show that *Scn1a* mutation paradoxically enhances the post-inhibitory rebound bursts. We next asked whether the prolonged rebound burst firing could result from enhanced T-type calcium currents that are known to underlie the post-inhibitory LTS and high-frequency burst firing in these cells (Jahnsen and Llinás, 1984). We recorded T-currents from *Scn1a* DS and WT mice using identical steady-state inactivation (SSI) protocols (Figure 5a). The peak T-current density, and the voltage-dependence and biophysical properties of the SSI T-type calcium currents were not altered in *Scn1a* DS nRT neurons (Figure 5b-e). These results show that the enhanced post-hyperpolarization firing in *Scn1a* DS nRT neurons is not due to a stronger T-current. As expected given the reduction in *Scn1a*, we observed that the AP threshold was significantly depolarized in DS mice and that the AP width was increased (Figure 5g) and the input resistance was enhanced (Figure 5f). *Furthermore,* the frequency and amplitude of spontaneous synaptic excitatory currents (sEPSCs) were similar between nRT neurons from *SCN1A* and WT mice (Figure 5h and 5i).

SK current deficit in nRT neurons underlies the enhanced cellular and circuit rhythmogenesis

Because burst firing in nRT neurons depends on interactions between T-type Ca^{2+} and small conductance calcium-activated (SK) K^+ channels (Cueni et al., 2008), we asked whether a deficit in SK function was

impaired in the *Scn1a* DS mice. Patch-clamp recordings showed that the density of SK currents in nRT neurons was reduced (Figure 2c, d). Further, quantitative PCR for a predominant SK subtype in nRT – SK2 (Wimmer et al., 2012) – showed that mRNA levels of a variant of the SK2 channel (*Kcnn2S*) was reduced in nRT and in hippocampus, but not S1 (somatosensory) cortical tissue isolated from DS mice (Figure 2d, Data Figure 6). Notably, in a rescue experiment, we find that enhancement of SK function using the SK agonist 1-Ethyl-2-benzimidazolinone (EBIO) (Cueni et al., 2008) is sufficient to normalize nRT bursting properties in *Scn1a* DS nRT neurons to WT levels (Figure 2e).

Using a biophysical model of a nRT neuron (Figure 2f), we found that reducing SK conductance was *sufficient* to account for the enhanced number of APs within the burst, as found in *Scn1a* DS nRT neurons (Figure 2g). This increase proved general, as the mean AP number in the entire DS parameter domain was larger, compared to that for WT (Figure 2h, see *Methods* for domain definitions).

We then assessed the impact of reduced SK conductance in the nRT neuron at the circuit level in a model including thalamocortical (TC) and nRT neurons (Figure 3a). We found that reduced SK phenocopied enhanced network oscillations (Figure 3b), with displayed longer duration (Figure 3c, d), increased number of bursts (Figure 3e, f) and lower oscillation frequency (Figure 3g, h) in the DS domain, quantitatively predicting those found experimentally in *Scn1a* DS thalamic circuits.

Mechanistically, the model evidenced that in the DS condition, the increased number of APs per burst in the nRT neuron produces deeper inhibition and thus a larger rebound in the TC neuron, which increased the excitatory TC→nRT feedback. Altogether, synaptic transmission was stronger in the circuit and thus more robust to noise, enabling more bursts and longer oscillations. Also, the model showed how longer nRT bursts and TC inhibitions explain the rather counterintuitive decrease in bursting frequency in DS mice. Remarkably, there was no requirement for modifying the fast sodium conductance in our model to account for experimental results. Thus, reduced SK function in nRT neurons makes the thalamus "epileptic" in that it enhances thalamic rhythmogenesis.

"Silent" non-convulsive seizures are a major phenotype in human and mouse DS.

We recorded seizures from human patients and *Scn1a* DS mice (Figure 4). We observed two major types of seizures in human patients and mice: non-convulsive seizures and generalized tonic clonic seizures (GTCS). The non-convulsive seizures are a major seizure type in patients with DS and are the most frequent seizure type in mice. They tend to be intractable and can progress in the so-called obtundation status resulting in a significant impairment of consciousness. However, non-convulsive seizures are under-recognized and understudied compared with convulsive seizures mainly because their inherent non-convulsive nature makes clinical diagnosis difficult (Dravet, 2011). Non-convulsive seizures occurred in average 10 ± 5 times per hour in mice and lasted 0.5-6 seconds (n=9 mice) and 7 ± 4 times per hour in our human DS patient and lasted on average 10 seconds (n=1 patient). We observed that non-convulsive seizures in *Scn1a* DS mice and DS patients exhibit similar spectral EEG signatures with fundamental frequencies ranging between 5 and 7 Hz (Figure 4a-e). To our knowledge, this study is the first to compare DS seizures between the *Scn1a* mouse model and human patients.

Optogenetic toggling of thalamic bursting bi-directionally modulates seizures in *SCN1A*-deficient mice

We next asked whether the high frequency burst firing that we observed *in vitro* also occurs during spontaneous seizures in freely behaving mice. Optrode recordings in nRT (Figure 7) and VB (Figure 4e) TC neurons showed high frequency burst firing phase locked with spontaneously occurring non-convulsive seizures.

Notably, nRT does not project directly onto the cortex and thus exerts its effects on cortical rhythms through its TC targets. To test the causality of the nRT-VB pathway in non-convulsive seizures, which predominate in the S1 ECoG, we used a recently-developed strategy to perturb VB

firing using Stable Step Function Opsin (SSFO). SSFO is a bistable opsin (Yizhar et al., 2011) whose activation in TC cells was recently shown to cause depolarization and a switch from bursting to tonic firing (Sorokin et al., 2017).

We unilaterally activated SSFO in VB following seizure-detection. SSFO activation reliably and rapidly eliminated TC bursts, toggled tonic firing, and stopped ongoing seizures (Figure 4g-j). This result suggests that phasic TC VB output is required for the maintenance of non-convulsive seizures in DS.

We then tested more clinically-tractable strategies for interrupting hyperthermia-triggered GTCS in DS patients using electrical stimulation. The spectrogram of these seizures showed a pronounced increase in broad gamma-band (30-100-Hz) power (Figure 8b). Since we had pinpointed the thalamus as a potential choke point for DS seizure control, we employed unilateral electrical stimulation manipulation of VB (Figure 8c, d) and the anterior thalamic nuclei AN (Andrade et al., 2010), (Figure 8e, f) upon the start of temperature-induced GTCS in our *Scn1a* DS model. Moreover, we also attempted to stop these GTCS by stimulating the medial and interposed cerebellar nuclei (Figure 4g, h), which divergently connect throughout the thalamic complex and thereby could modulate various cerebral cortical regions (Kros et al., 2015, TiNS). No clear anti-epileptic effects were observed when electrically stimulating these nuclei once the GTCS had started (Figure 8). These data indicate that the temperature-induced GTCS in our *Scn1a* DS model engulf not only thalamo-cortical networks, but also other parts of the brain, and that *ad hoc* electrical stimulation of thalamic or cerebellar nuclei is ineffective in disrupting the seizure-related activity.

Having shown that stopping phasic firing of TC cells stops non-convulsive seizures, we next asked: is mimicking the rhythmic hyperpolarizations in nRT->VB pathway sufficient to cause seizures during normal baseline behavior? We expressed halorhodopsin (eNpHR) in TC neurons as described in Sorokin et al., 2017 and showed that unilaterally driving TC phasic firing causes GTCS in *Scn1a* DS mice (Figure 9). This is a striking result given that TC neurons of primary thalamic nuclei project exclusively to ipsilateral cortex (Jones, 2007).

Altogether these results suggest that the nRT-VB pathway is both *sufficient* to initiate and *necessary* to maintain seizures in *Scn1a* DS mice.

SK enhancement treats seizures in *SCN1A*-deficient mice

Given that the SK agonist EBIO restored the burst firing in nRT neurons to WT levels (see Figure 2e), and that SK current reduction underlies hyperexcitability in nRT-VB microcircuit (Figure 3), we asked whether pharmacological boosting of SK channels could rescue seizures in *Scn1a* DS mice. Acute injection of EBIO systemically or locally in nRT reduced the number of spontaneously occurring non-convulsive seizures in *Scn1a* DS mice (Figure 4k-n). These results support SK channel dysfunction as a cellular mechanism for the behavioral epileptic seizures.

Discussion

Using a well-established model of DS with *Scn1a* haploinsufficiency, we uncover a novel and unexpected framework to explain intractable seizure pathology in DS whereby *Scn1a* reduction, together with reduced SK current in nRT, drive thalamic hyperexcitability to promote cortical seizures.

In contrast with previous work showing that dissociated cells from the GABAergic nRT of *Scn1a*-deficient mice are *hypoexcitable* and fire less APs, (Kalume et al., 2015), we find in the intact thalamic circuit in a comparable *Scn1a*-deficient model of DS that nRT neurons are *hyperexcitable* in that they fire more likely to fire bursts of APs. We show that this paradoxical increase in cell firing results from a compensatory decrease in SK2 channel expression and membrane conductance in nRT neurons. Our findings are distinct from previous work on DS, which has suggested that sodium channel deficits in inhibitory neurons result in *reduced* firing and thus reduced network inhibition in neocortex and hippocampus to promote seizures (Cheah et al., 2012; Dutton et al., 2013; Ogiwara et al., 2007; Tai et al., 2014; Yu et al., 2006). Moreover, our results contrast with another study in which a missense mutation in *Scn1a* associated with genetic epilepsy with febrile seizures resulted in a reduced firing in nRT neurons (Hedrich et al., 2014). Thus, thalamic circuit dysfunction and seizure pathology in DS involve complex interactions with *Scn1a*, its particular mutation, and the respective brain circuits in which *Scn1a* is found. Our results buoy the recently emerging view the DS pathology is driven by more than inhibitory neuron hypoexcitability (De Stasi et al., 2016; Hull and Isom, 2016) by defining a novel role for *Scn1a* in the thalamus.

The identification of SK2 as a modifier of DS seizures is novel and expands upon the growing list of modifiers of *SCN1A*-epilepsies (Calhoun et al., 2017; Hawkins and Kearney, 2016; Hawkins et al., 2016; Martin et al., 2007). Additionally, our findings complement existing literature on SK2 function in thalamic circuitry and other symptoms associated with DS. Notably, mice lacking SK2 show fragmented sleep patterns and reduced sleep spindles (Cueni et al., 2008) similar to DS mice (Kalume et al., 2015), supporting that reductions in SK2 underlie thalamic circuit dysfunction and its associated sleep impairments in DS.

Interestingly, overexpression of SK2 increases sleep spindles and reduces sleep fragmentation (Wimmer et al., 2012), further supporting that enhancement of SK2 function in DS might restore sleep impairments, in addition to treating intractable seizures.

To our knowledge, we are also the first to describe and define a mechanism for non-convulsive seizures in DS and compare this phenomenon with human patients. Although currently understudied, non-convulsive seizures are intractable and often co-occur with other pathology such as cognitive and social deficits – which notably are also not well-treated in DS. Indeed, non-convulsive seizures, in particular atypical absence seizures, are co-morbid with autism spectrum disorders in multiple mouse models (Holder and Quach, 2016; Jung et al., 2013). By identifying the SK current as a novel therapeutic target for the non-convulsive seizures in DS, we also posit that enhancing SK function might treat deficits in cognition and social interaction in DS.

Given the recently uncovered framework of nRT organization and function (Clemente-Perez et al., 2017), we hypothesize that the nRT is a key brain substrate responsible for the co-morbidity between neurological (seizure) and psychiatric (autism) components in DS. Within this framework, we propose that the nRT, through its respective projections on sensory and limbic thalamocortical nuclei, underlies the complex intractable seizures and autism, respectively, in DS that can act as a choke point to treat the multi-faceted DS.

Experimental Procedures

Scn1a DS mice

We performed all experiments per protocols approved by the Institutional Animal Care and Use Committee at the University of California, San Francisco and Gladstone Institutes. Precautions were taken to minimize stress and the number of animals used in each set of experiments. Mice were separately housed after surgical implants. Mice modeling Dravet syndrome, *Scn1a*$^{R1407X+/-}$ mice (Ogiwara et al., 2007), hereafter referred to as *Scn1a* DS mice, and wild-type (WT) littermates were used in this study and maintained on a mixed background (~80-88% C57BL6J (Jax 000664) / ~12-20% C3HeB/FeJ (Jax 000658). *Scn1a* Both male and female mice were used for these experiments and ages ranged between p18 to p300.

Viral injections

Stereotaxic viral injections were carried out as described (Paz et al., 2011, 2013). Briefly, in WT or *Scn1a* DS mice, adeno-associated virus carrying genes for halorhodopsin (rAAV5/CamkIIa-eNphR3.0-eYFP-WPRE-Pa (6x10^{12} genome copies per ml)) or eYFP alone (rAAV5/CamkIIa-eYFP-WPRE-Pa (7.4 x10^{12} genome copies per ml)) or Stable Step Function Opsin (SSFO; rAAV5/CamkIIa-hChR2(C128S;D156A)-eYFP (5.2x10^{12} genome copies per ml)) was injected into the ventral basal nucleus of the thalamus (VB) using the following coordinates: 1.6 mm posterior to Bregma, 1.6 lateral relative to midline, and two separate injections of 400 nl of virus at 3.2 and 3.5 mm ventral to the cortical surface (total injected volume, 800nl). Viruses were acquired from (UNC Vector Laboratories SCR_002448). We allowed the viruses to express for anywhere between 3 weeks and 6 months, depending on the nature of the experiment.

Immunostaining, microscopy, and image analysis

Mice were anesthetized with a lethal dose of ketamine (300 mg/kg) and xylazine (30 mg/kg) and perfused with 4% paraformaldehyde in 1X PBS. Serial coronal sections (50 μm thick) were cut on a Leica SM2000R Sliding Microtome. Sections were mounted in an antifade medium (Vectashield) and imaged using a Biorevo BZ-9000 Keyence microscope at 10x-20x. The expression of the viral constructs in different brain regions was confirmed using the mouse brain atlas (Franklin and Paxinos, 2007).

Slice preparation

Mice were euthanized with 4% isoflurane, perfused with ice-cold sucrose cutting solution containing 234 mM sucrose, 2.5 mM KCl, 1.25 mM NaH_2PO_4, 10 mM $MgSO_4$, 0.5 mM CaCl2, 26 mM $NaHCO_3$, and 11 mM glucose, equilibrated with 95% O_2 and 5% CO_2, pH 7.4, and decapitated. We prepared 250 μm (for patch-clamp electrophysiology) or 400 μm (for thalamic microcircuit studies) - thick horizontal thalamic slices containing VB thalamus and nRT with a Leica VT1200 microtome (Leica Microsystems). We incubated the slices, initially at 32 °C for 1 h and then at 24–26 °C, in artificial cerebro-spinal fluid (aCSF) containing 126 mM NaCl, 2.5 mM KCl, 1.25 mM NaH_2PO_4, 1 mM $MgCl_2$, 2 mM $CaCl_2$, 26 mM $NaHCO_3$, and 10 mM glucose, equilibrated with 95% O_2 and 5% CO_2, pH 7.4 The thalamic slice preparation was performed as described (Paz et al., 2011, 2013).

Patch-clamp electrophysiology from thalamic slices

Recordings were performed as previously described (Paz et al., 2011, Paz et al. 2013). We visually identified nRT and thalamocortical neurons by differential contrast optics with a Zeiss (Oberkochen) Axioskop microscope and an infrared video camera. Recording electrodes made of borosilicate glass had a resistance of 2.5–4 MΩ when filled with intracellular solution. Access resistance was monitored in all the recordings, and cells were included for analysis only if the access resistance was <25 MΩ. We corrected the potentials for -15 mV liquid junction potential. Intrinsic and bursting properties were recorded in the

presence of kynurenic acid (2 mM, Sigma), the internal solution contained 67 mM potassium gluconate, 67 mM KCl, 1 mM $MgCl_2$, 0.1 mM $CaCl_2$, 10 mM HEPES, and 1.1 mM EGTA, 4mM ATP, 6mM phosphocreatine, pH adjusted to 7.4 with KOH (290 mOsm). For EPSCs and voltage-clamp recordings, the internal solution contained 120 mM potassium gluconate, 11 mM KCl, 1 mM $MgCl_2$, 1 mM $CaCl_2$, 10 mM HEPES, and 1 mM EGTA, pH adjusted to 7.4 with KOH (290 mOsm) recorded in the presence of picrotoxin (50 µM, Tocris). For EBIO recordings, 0.4 M EBIO was initially dissolved in DMSO and then diluted to 100 µM in aCSF containing kynurenic acid (2 mM) and picrotoxin (50 µM, Tocris). Recordings with EBIO were done 5-10 minutes after drug application. T-current measurements were conducted as described in (Clemente-Perez et al., 2017). For SK current recordings, apamin (100 nm final concentration) was diluted in aCSF containing the synaptic blockers kynurenic acid (2mM, Sigma) and picrotoxin (50 µM, Tocris) Recordings for SK current measurements were done 5-10 minutes after drug application. SK current was calculated by digitally subtracting T-current using measured in aCSF with and without apamin as has been done in (Cueni et al., 2008; Wells et al., 2016). Currents were subtracted using Clampfit 10.5 (Molecular Devices, SCR_011323).

Extracellular thalamic oscillations

We placed horizontal slices (400 µm) containing somatosensory thalamus in an interface chamber at 34 °C and superfused them at a rate of 2 ml min^{-1} with oxygenated aCSF (same as recipe used for patch-clamp electrophysiology, except supplemented with 0.3 mM glutamine for cellular metabolic support). Extracellular multi-unit activity (MU) recordings were obtained with a linear 16-channel multi-electrode array (Neuronexus) that spanned the nRT and VB. MUA signals were amplified 10,000 times and band-pass filtered between 100 Hz and 6 kHz using the RZ5 from Tucker-Davis Technologies (TDT, SCR_006495). Position of recording array was visually checked for each recording to confirm position of electrodes in nRT and VB. We delivered electrical stimuli to the internal capsule with a pair of tungsten

microelectrodes (50–100 kΩ, FHC). The stimuli were 100 μs in duration, 50 V in amplitude, and delivered once every 30 s.

We then used custom Matlab software to analyze thalamic MUA recordings.

Detection of *Kcnn2* mRNA in brain tissue

Scn1a DS mice and WT-littermate control mice (age 3 to 5 months) were euthanized with Fatal Plus and then S1 cortex, hippocampus, and nRT were microdissected in ice-cold sucrose cutting solution. Tissue was immediately flash-frozen and then RNA was isolated using Qiagen RNeasy kits with on-column DNAse digest. Superscript First-Strand cDNA synthesis kits were used to convert RNA into cDNA. qRT-PCR experiments were performed using the following primers for mouse *Kcnn2S* (short transcript variant, NM_080465.2): F- 5' AGT GGT CTG GAG GAA GAG GA 3' and R- 5' CAT TTG CAC GTT CTC CCG AA 3' and mouse *Kccn2L* (long transcript variant, NM_001312905.1): F-5' TGG TTA CAG ACT GAG ACT CTT GT 3' and R- 5' TCC TCT TCC TCC AGA CCA CT 3' and the mouse house-keeping gene *Gapdh* (NM_001289726.1 and NM_008084.3): F- 5' GGTCGGTGTGAACGGATTTG 3' and R- 5' GCAACAATCTCCACTTTGCC 3'. Reactions were performed using Sybr Green Master Mix (Applied Biosystems) on a 7900HT Fast Thermal Cycler (Applied Biosystems) and levels of *Kcnn2* mRNA were determined using the $\Delta\Delta C_T$ method.

Surgical implantation of devices for simultaneous recording of seizure activity and manipulation of brain regions

For optogenetic and stimulation studies, we designed devices containing multiple screws for acquisition of electrocorticogram (ECoG) signal, along with local field potential (LFP) and MUA signal recoded from tungsten electrode wires that were positioned approximately 250 and 500 μm from the tip of an optic fiber (200 μm core, ThorLabs) (Paz et al., 2013). Cortical screws were implanted bilaterally in S1 (-0.5 mm posterior from Bregma, ± 3.25 mm lateral), and bilaterally in V1 (-2.9 mm posterior from Bregma, ± 3.25

mm lateral). The following coordinates were used for both optogenetic and electrical stimulation of targeted brain regions: For manipulation of nRT, optrodes were implanted at -1.3 mm posterior from Bregma, 2.1 mm lateral, and 2.75 mm deep. For manipulation of VB, optrodes were implanted at -1.5 posterior from Bregma, 1.5 mm lateral, and 3.0 mm deep. For manipulation of AN, optrodes were implanted at 0.8 mm posterior from Bregma, 0.75 mm lateral, and 2.75 mm deep. For manipulation of CN and MCN, optrodes were implanted at 2.5 mm posterior from lamda, 2.0 - 2.2 mm lateral, and 2.2 mm deep and 2.5 mm posterior from lamda, 1.2-1.5 mm lateral, and 2.0 mm deep, respectively.

Mice were also instrumented for local infusion of drug into nRT using cannulas (Plastics One). Briefly, we made custom-built devices in which a guide cannula was attached to our devices for recording ECoG. Tungsten wires were glued to the guide cannula, so that they protruded 250 and 400 um from the tip of the insert cannula (500 µM protrusion from tip of guide cannula). To target nRT, guide cannulas were implanted at -1.3 mm posterior from Bregma, 2 mm lateral, and 2.5 mm deep.

Mice were allowed to recover for at least one week before recording. ECoG and thalamic LFP signals were recorded using RZ5 (TDT) and sampled at 1221 Hz, with thalamic MUA signals sampled at 24 kHz. A video camera that was synchronized to the signal acquisition was used to continuously monitor the animals. Animals were briefly anesthetized with ~2% isoflurane at the start of each recording to connect for recording. Each recording trial lasted 30–180 min. To control for circadian rhythms, we housed our animals using a regular light/dark cycle, and performed recordings between roughly 11:00 AM and 6:00 PM.

In vivo optogenetics during free behavior

We simultaneously passed a fiber optic with an inline rotating joint (Doric) through a concentric channel in the electrical commutator, and connected it to the 200 µm core fiber optic in each animal's headpiece while recording ECoG/MU. The fiber optic was connected to 450 nm and 532 nm wavelength laser control boxes, which were triggered externally using the RZ5 (TDT). The tip of the optical fiber rested 100-500

μm from the most ventral tungsten electrode on each optrode to allow maximal activation of the desired brain region. We used 5–35 mW of laser power, measured at the end of the optical fiber before connecting to the animals.

Electrical stimulation of targeted brain regions during free behavior

We connected two leads to the implanted tungsten electrodes in desired brain regions that were attached to a biphasic stimulator. Electrical stimulation conditions were selected based on those that were 80% of the current amplitude necessary to a motor response in the case of the cerebellar-targeted mice or a current amplitude of ~200 uA was used in the case of the thalamus-targeted mice. For cerebellar stimulation reaching a motor response current amplitude ranged between 50 and 500 μA using a 1 second 8 or 100 Hz pulse train with 400 μsec pulse width. Sham stimulation involved the delivery of 0.5 uA of current which did not evoke any change in behavior.

Hyperthermia-triggered seizure paradigm

We subjected *Scn1a* DS mice between ages p45 and p300 to the hyperthermia-triggered seizure paradigm to evoke GTCS activity and correlate firing of brain regions. Briefly, a rectal probe was used to monitor internal body temperature, while a heat lamp (Physitemp) was used to raise the mouse body temperature by 0.5 degrees per minute. Note this protocol in which rodent body temperature was raised at a faster rate than previous studies (Cheah et al., 2012) reliably elicited seizures in all ages of *Scn1a* DS mice tested, without going over the 42.5ºC set-point. After the first evoked seizure ended, mice were immediately cooled and recorded until they resumed normal behavior. In some cases, optogenetic or electrical stimulation manipulations of targeted brain regions were performed during the hyperthermia-triggered seizure paradigm.

Pharmacological manipulations during free behavior

All animals were habituated to the recording chamber prior to drug studies. To determine the effects of systemic EBIO administration on non-convulsive seizure frequency in *Scn1a* DS mice, we used a randomized-block design to record half of mice on test Day 1 with vehicle (s.c. 250 µl of 10% DMSO/90% saline) and half of the mice with EBIO (s.c. 25 mg/kg, dissolved in 10% DMSO and 90% saline) (Wells et al., 2016). We then reversed the drug condition for test day 2 (which was 48 hours later). Non-convulsive seizures were manually scored off-line by an experienced user during the first 30 minutes of vehicle or EBIO application. Note, as EBIO also changed the brain state (more time spent in stage II sleep), the user could not be blinded to the experimental condition.

To determine the effects of local infusion of EBIO into the nRT, we implanted mice with cannulas (Plastics One) targeting the right nRT. Following recovery from surgery, 800 nl of vehicle (0.25% DMSO in saline) was infused into the right nRT at a rate of 200 nl per minute using a syringe pump. ECoG and thalamic LFP/MUA was then recorded for 1-hour post drug administration. EBIO (400 uM, 0.0015% DMSO in saline) was then infused into the right nRT and the ECoG and thalamic LFP/MUA was recorded for an additional hour. Non-convulsive seizures were manually scored off-line by an experienced user during the first 60 minutes of vehicle or EBIO application.

Human Seizure Recordings

All procedures were approved by the Regional and Institutional Committee of Science and Research Ethics of Scientific Council of Health. Per institutional guideline, this clinical case study was exempted from IRB approval. The original video-EEG recording of a 7 years-old patient with Dravet syndrome associated with *SCN1A* pathogenic variant was reviewed by an experienced pediatric neurophysiologist (M.R.C). The international 10–20 system was used for electrode placement. The recording lasted for a total of 19 hours 45 minutes (8 hours 49 minutes awake). Atypical absences where defined as discharge of irregular high voltage spikes and slow waves accompanied by decrease awareness and at time eyelids and/or upper limb slight myoclonic jerks.

QUANTIFICATION AND STATISTICAL ANALYSIS

All numerical values are given as means and error bars are Standard Error of the Mean (SEM) unless stated otherwise. Data analysis was performed with MATLAB (SCR_001622), Origin 9.0 (Microcal Software, SCR_002815), GraphPad Prism 6 (SCR_002798), and SigmaPlot (SCR_003210).

Comparison of thalamic circuit oscillations in thalamic slices

We used custom Matlab software to detect extracellular spikes based on taking the first derivative of the MU signal and thresholding over background. Spikes were excluded if their waveform last 2 ms longer. An experienced user confirmed parameter settings to optimize for all recordings. Bursts were defined as three or more spikes per burst, with the max interburst interval as 1.2 s. We quantified the number of total evoked bursts and oscillation duration recorded in the most active VB channels using on average 10-20 sweeps per recording. All data were compared using a Mann-Whitney test, with alpha = 0.05. (*$p<0.05$, **$p<0.01$, ***$p<0.001$).

Analysis of electrophysiological properties

Data for T-current half-maximal voltage (V50%) was taken from the Boltzmann function calculated using Origin 9.0 (Microcal Software, SCR_002815). Most data were compared using a Mann-Whitney test, with alpha=0.05 (*$p<0.05$, **$p<0.01$, ***$p<0.001$). Number of APs on 1^{st} burst measured against hyperpolarization step was compared through individual unpaired t-tests not corrected for multiple comparisons, with alpha=0.05, (*$p<0.05$, **$p<0.01$, ***$p<0.001$). Mann-Whitney tests and individual unpaired t-tests were done using GraphPad Prism 6 (SCR_002798).

Analysis of cortical rhythm modulation by selective optical activation of thalamic neurons during free behavior

ECoG spectral analysis: Spectrogram images in Figure 4 were generated for frequencies between 0 and 25 Hz using the short-time Fourier transform with 0.5 s Hamming windows and 98% overlap between segments. The power spectral density estimates were plotted as the mean values of the spectrogram at each point between 0-25 Hz during the seizure event.

Optogenetic seizure interruption analysis: To compare the effects of light on EcoG power, we calculated relative changes in averaged band power between pre-stimulus (PreStim, 2 s before light pulse) and post-stimulus (PostStim, 2 s after end of light pulse) periods across multiple recording trials (Figure 4). Average power between 1-25 Hz was calculated using a modified periodogram. The difference between groups was analyzed using a Mann-Whitney rank sum test ($p<0.005$).

Computational modeling: Methods summary

A minimal computational model of the negative feedback loop between thalamocortical (TC) neurons and thalamic reticular nucleus (nRT) neurons was built to assess the oscillatory response of thalamic slices. A Hodgkin-Huxley model described TC and nRT neurons excitability, with parameters fitted from whole-cell recordings, in wild type and Dravet syndrome conditions. The behavior of the TC–nRT circuit was explored parametrically.

Computational modeling

A computational model of the negative feedback loop between thalamocortical (TC) neurons and thalamic reticular nucleus (nRT) neurons was built to assess the oscillatory response of thalamic slices in wild type (WT) and Dravet syndrome (DS) mice. TC and nRT neurons' excitability was described using the Hodgkin-Huxley formalism, based on previous modelling (Destexhe et al., 1994; Paz et al., 2013; Traub et al., 1991), with some parameters fitted from present intracellular recordings. The nRT model included the leak, fast

sodium, delayed rectifier potassium, low-threshold calcium (CaT), calcium-activated potassium (SK) and calcium-activated non-specific cationic (CAN) currents, while the TC model incorporated the leak, fast sodium, delayed rectifier potassium, low-threshold calcium (CaT) and hyperpolarization-activated (H) currents. Both neuron models included first-order calcium dynamics. The negative feedback loop between TC and nRT neurons was implemented with AMPA and NMDA currents at TC→ nRT synapses and GABA–A and GABA–B currents at nRT→TC synapses. A noise current with zero mean was introduced in both nRT and TC neurons to account for the stochasticity observed experimentally in the thalamic circuit. The WT domain was defined, in the space of CaT and SK maximal conductances of the nRT neuron, as the parameter region yielding realistic nRT action potential firing frequencies and circuit oscillations with burst numbers and durations consistent with those obtained in slices. The DS domain was defined as the region with a similar CaT maximal conductance range but with lower SK maximal conductance, consistent with the smaller SK current found in intracellular nRT recordings in DS mice. Details of the model can be found in the *Methods* section of the supplementary material.

References

Andrade, D.M., Hamani, C., Lozano, A.M., and Wennberg, R.A. (2010). Dravet syndrome and deep brain stimulation: Seizure control after 10 years of treatment. Epilepsia *51*, 1314–1316.

Auerbach, D.S., Jones, J., Clawson, B.C., Offord, J., Lenk, G.M., Ogiwara, I., Yamakawa, K., Meisler, M.H., Parent, J.M., and Isom, L.L. (2013). Altered Cardiac Electrophysiology and SUDEP in a Model of Dravet Syndrome. PLoS ONE *8*, e77843.

Barthó, P., Slézia, A., Mátyás, F., Faradzs-Zade, L., Ulbert, I., Harris, K.D., and Acsády, L. (2014). Ongoing Network State Controls the Length of Sleep Spindles via Inhibitory Activity. Neuron *82*, 1367–1379.

Bazhenov, M., Timofeev, I., Steriade, M., and Sejnowski, T. (2000). Spiking-Bursting Activity in the Thalamic Reticular Nucleus Initiates Sequences of Spindle Oscillations in Thalamic Networks. J. Neurophysiol. *84*, 1076.

Beenhakker, M.P., and Huguenard, J.R. (2009). Neurons that Fire Together Also Conspire Together: Is Normal Sleep Circuitry Hijacked to Generate Epilepsy? Neuron *62*, 612–632.

Calhoun, J.D., Hawkins, N.A., Zachwieja, N.J., and Kearney, J.A. (2017). Cacna1g is a genetic modifier of epilepsy in a mouse model of Dravet syndrome. Epilepsia *58*, e111–e115.

Cheah, C.S., Yu, F.H., Westenbroek, R.E., Kalume, F.K., Oakley, J.C., Potter, G.B., Rubenstein, J.L., and Catterall, W.A. (2012). Specific deletion of NaV1.1 sodium channels in inhibitory interneurons causes seizures and premature death in a mouse model of Dravet syndrome. Proc. Natl. Acad. Sci. *109*, 14646–14651.

Claes, L., Del-Favero, J., Ceulemans, B., Lagae, L., Van Broeckhoven, C., and De Jonghe, P. (2001). De Novo Mutations in the Sodium-Channel Gene SCN1A Cause Severe Myoclonic Epilepsy of Infancy. Am. J. Hum. Genet. *68*, 1327–1332.

Claes, L.R., Deprez, L., Suls, A., Baets, J., Smets, K., Van Dyck, T., Deconinck, T., Jordanova, A., and De Jonghe, P. (2009). The SCN1A variant database: a novel research and diagnostic tool. Hum. Mutat. *30*, E904–E920.

Clemente-Perez, A., Makinson, S.R., Higashikubo, B., Brovarney, S., Cho, F.S., Urry, A., Holden, S.S., Wimer, M., Dávid, C., Fenno, L.E., et al. (2017). Distinct Thalamic Reticular Cell Types Differentially Modulate Normal and Pathological Cortical Rhythms. Cell Rep. *19*, 2130–2142.

Crick, F. (1984). Function of the thalamic reticular complex: the searchlight hypothesis. Proc. Natl. Acad. Sci. *81*, 4586–4590.

Cueni, L., Canepari, M., Lujan, R., Emmenegger, Y., Watanabe, M., Bond, C.T., Franken, P., Adelman, J.P., and Luthi, A. (2008). T-type Ca2+ channels, SK2 channels and SERCAs gate sleep-related oscillations in thalamic dendrites. Nat Neurosci *11*, 683–692.

Dang-Vu, T.T., McKinney, S.M., Buxton, O.M., Solet, J.M., and Ellenbogen, J.M. (2010). Spontaneous brain rhythms predict sleep stability in the face of noise. Curr. Biol. *20*, R626–R627.

De Stasi, A.M., Farisello, P., Marcon, I., Cavallari, S., Forli, A., Vecchia, D., Losi, G., Mantegazza, M., Panzeri, S., Carmignoto, G., et al. (2016). Unaltered Network Activity and Interneuronal Firing During Spontaneous Cortical Dynamics In Vivo in a Mouse Model of Severe Myoclonic Epilepsy of Infancy. Cereb. Cortex N. Y. NY *26*, 1778–1794.

Deschenes, M., Paradis, M., Roy, J.P., and Steriade, M. (1984). Electrophysiology of neurons of lateral thalamic nuclei in cat: resting properties and burst discharges. J. Neurophysiol. *51*, 1196.

Dravet, C. (2011). The core Dravet syndrome phenotype. Epilepsia *52*, 3–9.

Dutton, S.B., Makinson, C.D., Papale, L.A., Shankar, A., Balakrishnan, B., Nakazawa, K., and Escayg, A. (2013). Preferential inactivation of Scn1a in parvalbumin interneurons increases seizure susceptibility. Neurobiol. Dis. *49*, 211–220.

Ferrarelli, F., and Tononi, G. (2011). The Thalamic Reticular Nucleus and Schizophrenia. Schizophr. Bull. *37*, 306–315.

Gentet, L.J., and Ulrich, D. (2003). Strong, reliable and precise synaptic connections between thalamic relay cells and neurones of the nucleus reticularis in juvenile rats. J. Physiol. *546*, 801–811.

Halassa, M.M., and Acsády, L. (2016). Thalamic Inhibition: Diverse Sources, Diverse Scales. Trends Neurosci. *39*, 680–693.

Hawkins, N.A., and Kearney, J.A. (2016). Hlf is a genetic modifier of epilepsy caused by voltage-gated sodium channel mutations. Epilepsy Res. *119*, 20–23.

Hawkins, N.A., Zachwieja, N.J., Miller, A.R., Anderson, L.L., and Kearney, J.A. (2016). Fine Mapping of a Dravet Syndrome Modifier Locus on Mouse Chromosome 5 and Candidate Gene Analysis by RNA-Seq. PLoS Genet. *12*, e1006398.

Hedrich, U.B.S., Liautard, C., Kirschenbaum, D., Pofahl, M., Lavigne, J., Liu, Y., Theiss, S., Slotta, J., Escayg, A., Dihné, M., et al. (2014). Impaired Action Potential Initiation in GABAergic Interneurons Causes Hyperexcitable Networks in an Epileptic Mouse Model Carrying a Human $Na_V1.1$ Mutation. J. Neurosci. *34*, 14874.

Holder, J.L., and Quach, M.M. (2016). The spectrum of epilepsy and electroencephalographic abnormalities due to SHANK3 loss-of-function mutations. Epilepsia *57*, 1651–1659.

Houser, C.R., Vaughn, J.E., Barber, R.P., and Roberts, E. (1980). GABA neurons are the major cell type of the nucleus reticularis thalami. Brain Res. *200*, 341–354.

Hull, J.M., and Isom, L.L. (2016). Expecting the Unexpected: Lack of In Vivo Network Defects in an Scn1a Model of Dravet Syndrome. Epilepsy Curr. *16*, 408–410.

Huntsman, M.M., Porcello, D.M., Homanics, G.E., DeLorey, T.M., and Huguenard, J.R. (1999). Reciprocal Inhibitory Connections and Network Synchrony in the Mammalian Thalamus. Science *283*, 541.

Jahnsen, H., and Llinás, R. (1984). Electrophysiological properties of guinea-pig thalamic neurones: an in vitro study. J. Physiol. *349*, 205–226.

Jones, E.G. (2007). The Thalamus. History *326*, 419–442.

Jung, S., Seo, J.S., Kim, B.S., Lee, D., Jung, K.-H., Chu, K., Lee, S.K., and Jeon, D. (2013). Social deficits in the AY-9944 mouse model of atypical absence epilepsy. Behav. Brain Res. *236*, 23–29.

Kalume, F., Westenbroek, R.E., Cheah, C.S., Yu, F.H., Oakley, J.C., Scheuer, T., and Catterall, W.A. (2013). Sudden unexpected death in a mouse model of Dravet syndrome. J. Clin. Invest. *123*, 1798–1808.

Kalume, F., Oakley, J.C., Westenbroek, R.E., Gile, J., de la Iglesia, H.O., Scheuer, T., and Catterall, W.A. (2015). Sleep impairment and reduced interneuron excitability in a mouse model of Dravet Syndrome. Neurobiol. Dis. *77*, 141–154.

Makinson, C.D., Tanaka, B.S., Sorokin, J.M., Wong, J.C., Christian, C.A., Goldin, A.L., Escayg, A., and Huguenard, J.R. (2017). Regulation of Thalamic and Cortical Network Synchrony by Scn8a. Neuron *93*, 1165–1179.e6.

Martin, M.S., Tang, B., Papale, L.A., Yu, F.H., Catterall, W.A., and Escayg, A. (2007). The voltage-gated sodium channel Scn8a is a genetic modifier of severe myoclonic epilepsy of infancy. Hum. Mol. Genet. *16*, 2892–2899.

Ogiwara, I., Miyamoto, H., Morita, N., Atapour, N., Mazaki, E., Inoue, I., Takeuchi, T., Itohara, S., Yanagawa, Y., Obata, K., et al. (2007). $Na_v1.1$ Localizes to Axons of Parvalbumin-Positive Inhibitory Interneurons: A Circuit Basis for Epileptic Seizures in Mice Carrying an Scn1a Gene Mutation. J. Neurosci. *27*, 5903.

Papale, L.A., Makinson, C.D., Christopher Ehlen, J., Tufik, S., Decker, M.J., Paul, K.N., and Escayg, A. (2013). Altered sleep regulation in a mouse model of SCN1A-derived genetic epilepsy with febrile seizures plus (GEFS+). Epilepsia *54*, 625–634.

Paz, J.T., Christian, C.A., Parada, I., Prince, D.A., and Huguenard, J.R. (2010). Focal Cortical Infarcts Alter Intrinsic Excitability and Synaptic Excitation in the Reticular Thalamic Nucleus. J. Neurosci. *30*, 5465.

Paz, J.T., Bryant, A.S., Peng, K., Fenno, L., Yizhar, O., Frankel, W.N., Deisseroth, K., and Huguenard, J.R. (2011). A new mode of corticothalamic transmission revealed in the Gria4-/- model of absence epilepsy. Nat Neurosci *14*, 1167–1173.

Paz, J.T., Davidson, T., Freschette, E., Delord, B., Prada, I., Peng, K., Deisseroth, K., and Huguenard, J.R. (2013). Closed-loop optogenetic control of thalamus as a new tool to interrupt seizures after cortical injury. Nat. Neurosci. *16*, 64–70.

Rubinstein, M., Han, S., Tai, C., Westenbroek, R.E., Hunker, A., Scheuer, T., and Catterall, W.A. (2015). Dissecting the phenotypes of Dravet syndrome by gene deletion. Brain *138*, 2219–2233.

Sherman, S.M. (2001a). A wake-up call from the thalamus. Nat Neurosci *4*, 344–346.

Sherman, S.M. (2001b). Tonic and burst firing: dual modes of thalamocortical relay. Trends Neurosci. *24*, 122–126.

Slaght, S.J., Leresche, N., Deniau, J.-M., Crunelli, V., and Charpier, S. (2002). Activity of Thalamic Reticular Neurons during Spontaneous Genetically Determined Spike and Wave Discharges. J. Neurosci. *22*, 2323.

Sorokin, J.M., Davidson, T.J., Frechette, E., Abramian, A.M., Deisseroth, K., Huguenard, J.R., and Paz, J.T. (2017). Bidirectional Control of Generalized Epilepsy Networks via Rapid Real-Time Switching of Firing Mode. Neuron *93*, 194–210.

Steriade, M., Domich, L., Oakson, G., and Deschenes, M. (1987). The deafferented reticular thalamic nucleus generates spindle rhythmicity. J. Neurophysiol. *57*, 260.

Tai, C., Abe, Y., Westenbroek, R.E., Scheuer, T., and Catterall, W.A. (2014). Impaired excitability of somatostatin- and parvalbumin-expressing cortical interneurons in a mouse model of Dravet syndrome. Proc. Natl. Acad. Sci. *111*, E3139–E3148.

Traub, R.D., Wong, R.K., Miles, R., and Michelson, H. (1991). A model of a CA3 hippocampal pyramidal neuron incorporating voltage-clamp data on intrinsic conductances. J. Neurophysiol. *66*, 635.

Wimmer, R.D., Astori, S., Bond, C.T., Rovó, Z., Chatton, J.-Y., Adelman, J.P., Franken, P., and Lüthi, A. (2012). Sustaining Sleep Spindles through Enhanced SK2-Channel Activity Consolidates Sleep and Elevates Arousal Threshold. J. Neurosci. *32*, 13917.

Yizhar, O., Fenno, L.E., Prigge, M., Schneider, F., Davidson, T.J., O'Shea, D.J., Sohal, V.S., Goshen, I., Finkelstein, J., Paz, J.T., et al. (2011). Neocortical excitation/inhibition balance in information processing and social dysfunction. Nature *477*, 171–178.

Yu, F.H., Mantegazza, M., Westenbroek, R.E., Robbins, C.A., Kalume, F., Burton, K.A., Spain, W.J., McKnight, G.S., Scheuer, T., and Catterall, W.A. (2006). Reduced sodium current in GABAergic interneurons in a mouse model of severe myoclonic epilepsy in infancy. Nat Neurosci *9*, 1142–1149.

Zhang, Z.-W., Zak, J.D., and Liu, H. (2010). MeCP2 Is Required for Normal Development of GABAergic Circuits in the Thalamus. J. Neurophysiol. *103*, 2470.

Figures

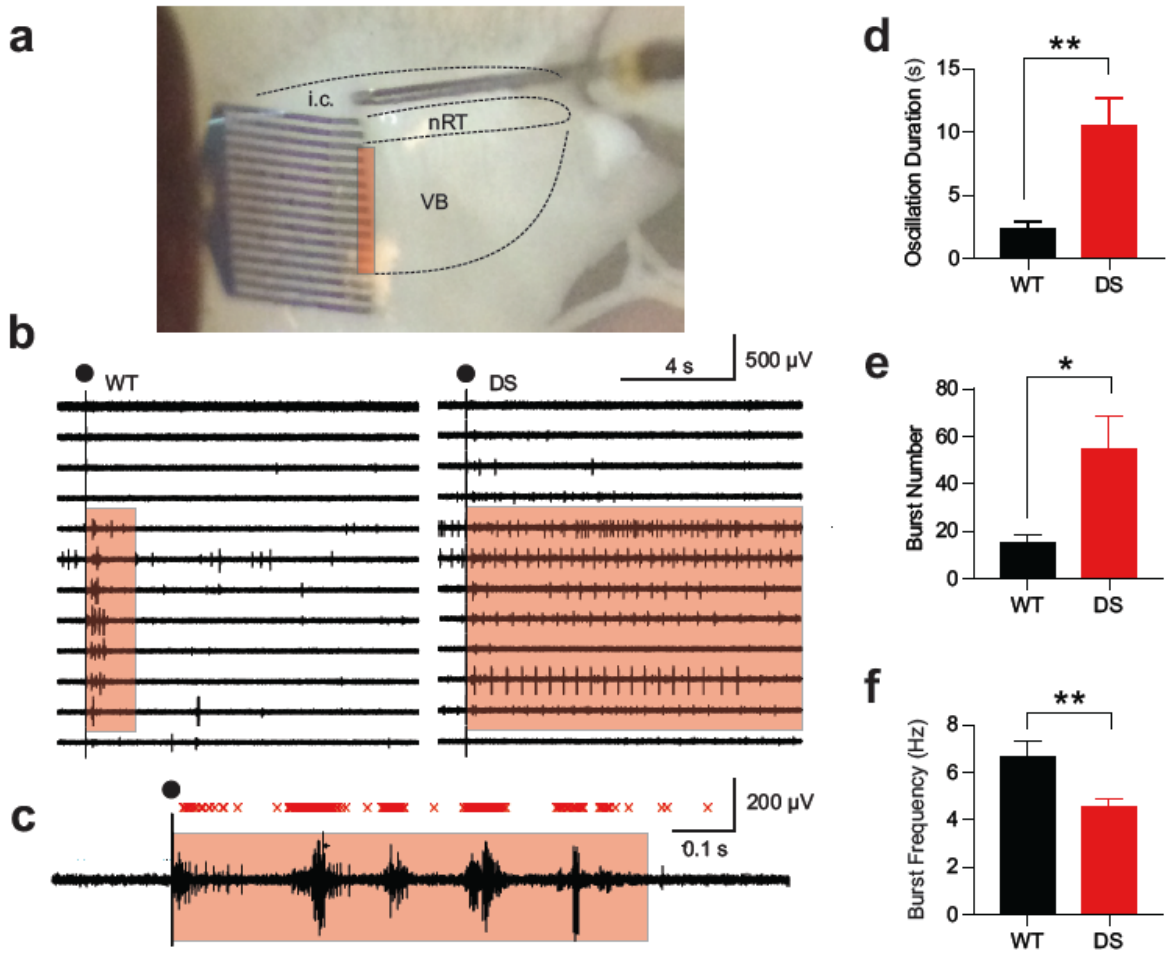

Figure 3.1 *Scn1a* deficiency in nRT neurons enhances intra-thalamic circuit oscillations.

a) Horizontal slice preparation to study intra-thalamic circuit oscillations. Position of 16-channel linear array silicon probe showing the region of the ventral basal thalamus studied. Evoked oscillations were elicited via stimulation of the internal capsule.

b) Representative example of evoked intra-thalamic circuit oscillations in slices prepared from WT and *Scn1a* DS mice. Black circles indicate stimulation artifact. Orange box indicates region of analysis in which evoked oscillations were observed.

c) Detection of extracellular multiunit spikes (red "X") and bursts that comprise a thalamic oscillation. Oscillation example taken from a slice prepared from a WT mouse.

d) Duration of evoked oscillation. Mann-Whitney U test. WT: n = 9 mice, *Scn1a* DS: n = 12 mice. ** $p < 0.01$.

e) Number of bursts within the evoked oscillation. Mann-Whitney U test. WT: n = 9 mice, *Scn1a* DS: n = 12 mice. ** $p < 0.01$.

f) Interburst interval within the evoked oscillation. Mann-Whitney U test. WT, n = 9 mice, DS, n = 12 mice. ** $p < 0.01$.

Abbreviations: i.c., internal capsule; nRT, thalamic reticular nucleus; VB, ventral basal nucleus of the thalamus; WT, wild-type; DS, *Scn1a* Dravet syndrome.

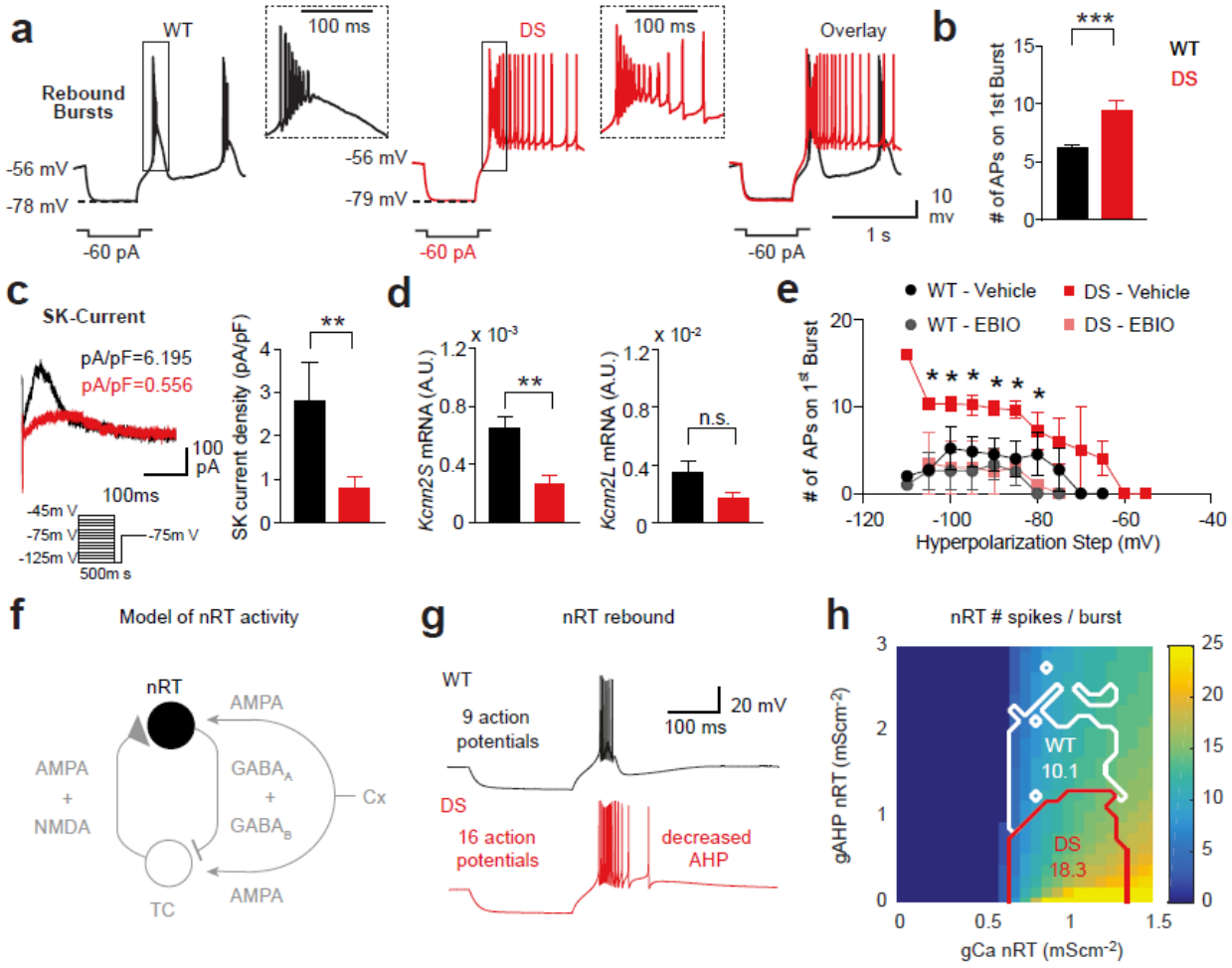

Figure 3.2. SK current deficiency in nRT neurons underlies the enhanced cellular bursting in *Scn1a* DS mice.

a)Representative traces showing that *Scn1a* DS neurons (red trace) exhibit enhanced post-inhibitory rebound burst firing upon hyperpolarization induced by −60 pA current pulses in comparison to WT neurons (black trace). Insets show zoom of APs on first rebound burst.

b) Number of APs on first rebound burst (WT: n = 30 cells, 4 mice; *Scn1a* DS, n = 43 cells, 6 mice). Data are represented as mean ± SEM, compared with parametric t-test with Welch's Correction and $\alpha = 0.05$, *** $p < 0.001$.

c)*Left*, Representative SK current traces obtained by digital subtraction in nRT neurons from WT (black trace) and *Scn1a* DS mutant (red trace) mice with respective current density. *Right*, Quantification of

SK current density defined as the maximal current divided by individual cell capacitance. Data are represented as mean ± SEM, compared with Mann-Whitney U test (** p = 0.0085). WT: n = 8 cells, 3 mice; *Scn1a* DS: n = 10 cells, 3 mice.

d) SK2 relative mRNA expression levels (encoded by the gene *Kcnn2,* short and long transcript variants) normalized to Gapdh mRNA, in nRT. Expression levels were calculated using the $\Delta\Delta C_T$ method and are expressed as arbitrary units. Mann-Whitney U test, ** $p < 0.01$.

e)Number of APs on the first rebound burst, plotted against hyperpolarization step (mV) with vehicle or 100 µM EBIO treatment. WT: n = 6 neurons, 3 mice; *Scn1a* DS: n = 6 neurons, 3 mice. Data represented as mean ± SEM. Data points compared through individual unpaired t-test, not corrected for multiple comparisons, * $p < 0.03$.

f) Schematic of the minimal thalamic circuit used for computational modeling, including a thalamocortical (TC) and a thalamic reticular nucleus (nRT) neuron, TC→nRT AMPA and NMDA excitatory synapses and nRT→TC GABA–A and GABA–B inhibitory synapses. Synaptic currents, are absent in the simulations of the nRT neuron mimicking intracellular recordings (Figure 2G-H).

g) Voltage traces of a nRT neuron in the WT parameter domain (black trace; $\overline{g}_{CaT}^{nRT} = 0.85 mScm^{-2}$ and $\overline{g}_{SK}^{nRT} = 2 mScm^{-2}$) and of a neuron in the DS domain with decreased calcium–activated SK maximum conductance (red trace; $\overline{g}_{CaT}^{nRT} = 0.85 mScm^{-2}$ and $\overline{g}_{SK}^{nRT} = 0.1 mScm^{-2}$), in response to a an hyperpolarizing injected current $I_{Inj}^{nRT} = -0.5 mAcm^{-2}$ for 500 ms.

h) Map of the average number of action potentials in the rebound burst in the nRT neuron model as a function of $\left\{\overline{g}_{CaT}^{nRT}, \overline{g}_{SK}^{nRT}\right\}$ maximal conductance parameters. Action potential numbers are computed over 30 simulations with different real izations of the stochastic current present to mimick the noise present in thalamic circuits. The mean of these average numbers of action potentials are indicated in the WT (white) and DS (red) domains. See *Methods* for the definition of WT and DS domains.

Abbreviations: WT, wild-type; DS, *Scn1a* Dravet syndrome; APs, action potentials; nRT, thalamic reticular nucleus; TC, thalamocortical; Cx, cortex.

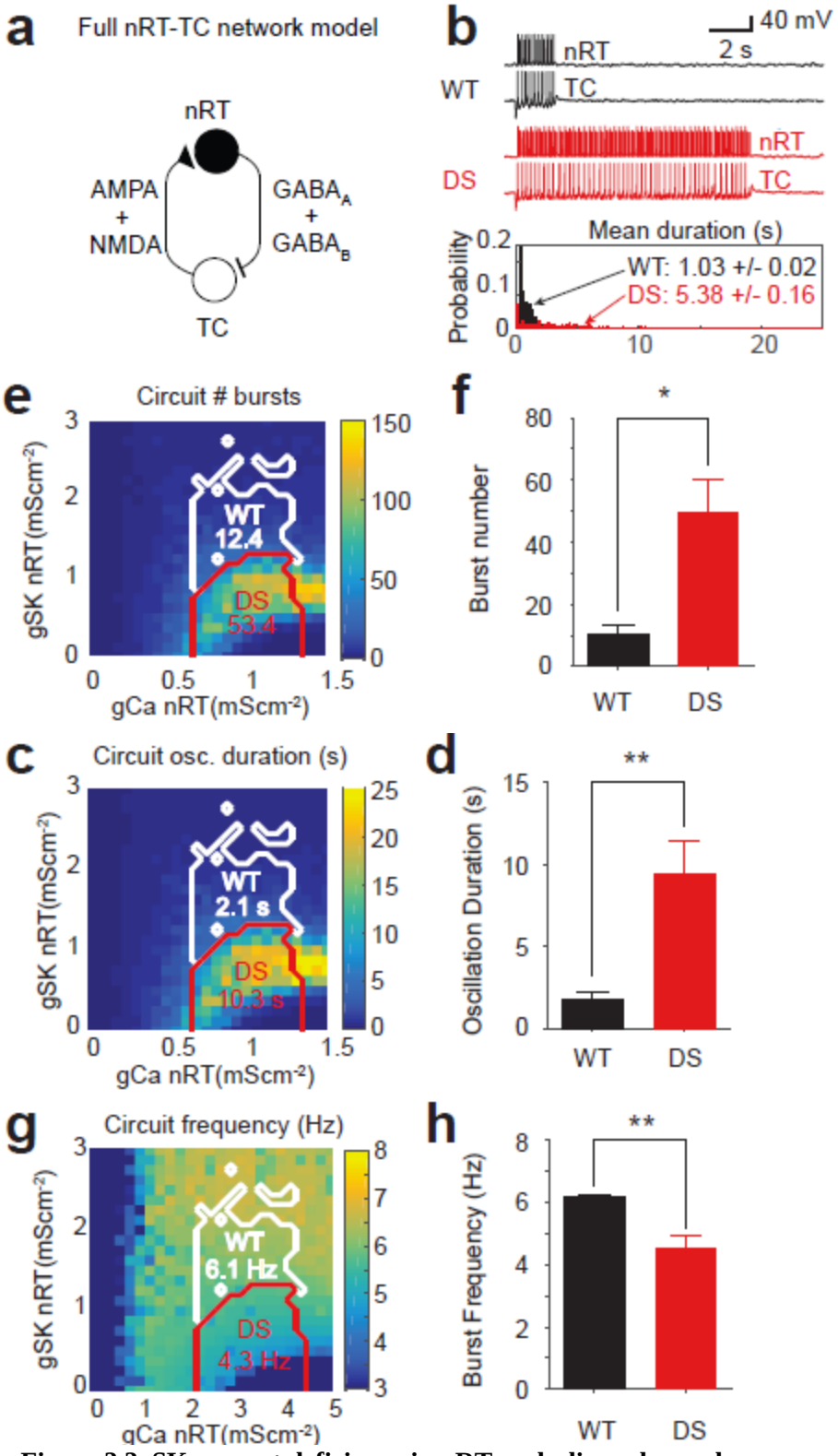

Figure 3.3. SK current deficiency in nRT underlies enhanced micro-circuit rhythmogenesis in *SCN1A* DS mice.

a) Schematic of the full nRT-TC circuit used for the computational modeling of thalamic oscillations in the WT and DS conditions.

b) The mean oscillation duration in the TC–nRT circuit model in the DS condition was ~5 times that in the WT condition. Example voltage traces of nRT and TC neurons in the model in WT and DS conditions (above). Probability distributions of the duration of oscillations in the thalamic circuit over 10^3 simulations with different realizations of the noisy background cortical input current. $\bar{g}_{CaT}^{nRT}$ and $\bar{g}_{SK}^{nRT}$ as in Figure 2G.

c) Map of the average oscillation duration of the TC–nRT circuit model as a function of $\left\{\bar{g}_{CaT}^{nRT}, \bar{g}_{SK}^{nRT}\right\}$ maximal conductance parameters, computed over 30 simulations with different realizations of the stochastic current. The mean of these averages in the WT and DS domains (white and red boundaries, respectively) are indicated.

d) Distributions of the oscillation duration of the TC–nRT circuit model of 9 samples from the WT region and 12 samples from the DS domain. The difference of the means of these samples is statistically significant (Mann–Whitney U test, WT: n = 9 mice, *Scn1a* DS: n = 12 mice. ** p = 0.0062).

e) Same as in (c) for the average number of bursts of the oscillation.

f) Same as in (d) for the average number of bursts of the oscillation. The difference of the means of these samples is statistically significant (Mann–Whitney U test, WT: n = 9 mice, *Scn1a* DS: n = 12 mice. * p = 0.0208)

g) Same as in (c) for the average frequency of the oscillation.

h) Same as in (d) for the average frequency of the oscillation. The difference of the means of these samples is statistically significant (Mann–Whitney U test, WT: n = 9 mice, *Scn1a* DS: n = 12 mice. ** p < 0.0002)

Abbreviations : WT, wild-type; DS, *Scn1a* Dravet syndrome; nRT, thalamic reticular nucleus; TC, thalamocortical; Cx, cortex.

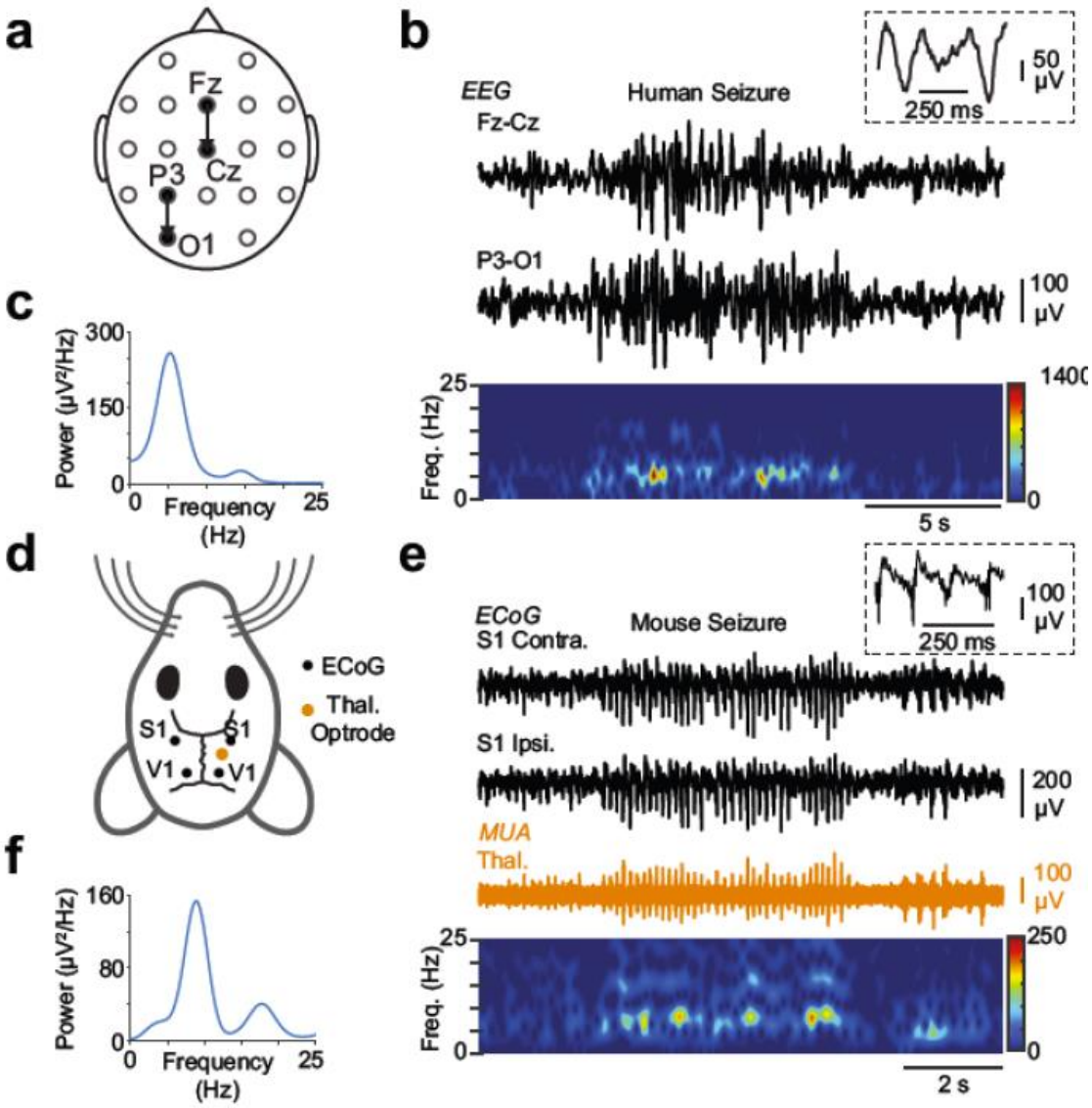
a
Fz
P3
Cz
O1
b
EEG
Human Seizure
Fz-Cz
P3-O1
50 µV
250 ms
100 µV
Freq. (Hz)
25
0
1400
0
5 s
c
Power (µV²/Hz)
300
150
0
0
Frequency (Hz)
25
d
ECoG
Thal. Optrode
S1
S1
V1
V1
e
ECoG
S1 Contra.
Mouse Seizure
100 µV
250 ms
S1 Ipsi.
200 µV
MUA
Thal.
100 µV
Freq. (Hz)
25
0
250
0
2 s
f
Power (µV²/Hz)
160
80
0
0
Frequency (Hz)
25

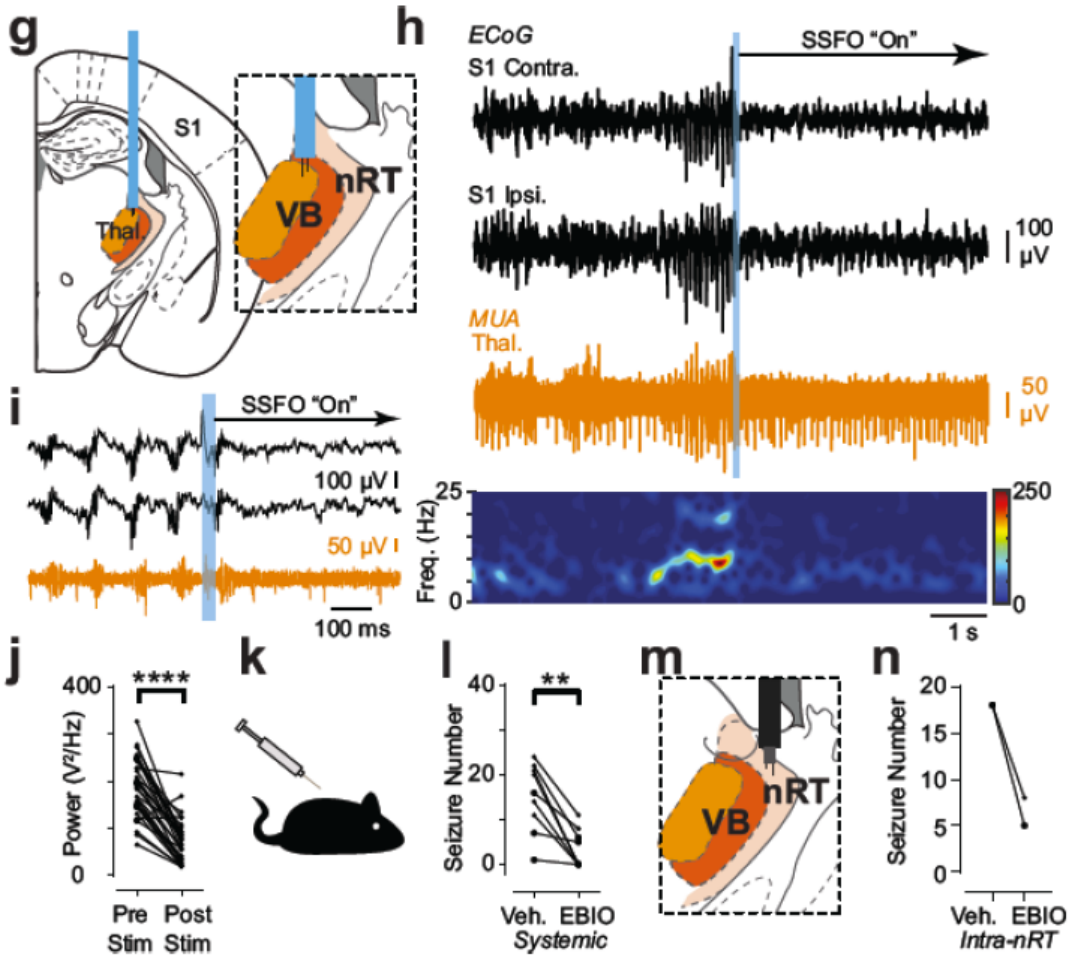

Figure 3.4. Dual strategy for seizure control in Dravet patients converge on the thalamus.

a) Diagram of human EEG recording montage.

b) *Top:* Example of the EEG signature of a typical non-convulsive seizure in a patient with DS recorded in two different locations on the scalp. *Inset*, Note the spikes are not typical spike-and-wave discharges and have a higher frequency component in addition to the slower oscillation. *Bottom:* Spectrogram showing frequency components of the recorded seizure.

c) Power spectral density of the seizure shown in b. Note the peak fundamental frequency is ~5 Hz.

d) Diagram of the mouse ECoG and thalamic depth electrode recording montage. ECoG was recorded from somatosensory (S1) and visual (V1) cortices, with a depth electrodes implanted in the thalamus.

e) *Top:* Example of an ECoG signature of a typical non-convulsive seizure in *Scn1a* DS mice recorded from S1 (black), along with simultaneous multi-unit (MU) recordings in the thalamus (orange). *Inset*, Note the spikes are not typical spike-and-wave discharges and have a higher frequency component in addition to the slower oscillation. *Bottom:* Spectrogram showing frequency components of the recorded seizure.

f) Power spectral density of the seizure shown in e. Note the peak fundamental frequency is ~6-7 Hz.

g) Diagram of optogenetic targeting of the thalamus. Inset, depth electrodes were positioned in VB thalamus.

h) *Top:* Example of optogenetic seizure interruption of an ongoing non-convulsive seizure in a *Scn1a* DS mouse. The blue bar corresponds to a brief ("50" ms) pulse of blue light to activate SSFO-expressing thalamocortical neurons. Unilateral activation of SSFO in the thalamus immediately interrupts an ongoing seizure. *Bottom:* Spectrogram showing frequency components of the recorded seizure and decrease in power after SSFO activation.

i) Magnification of the seizure interruption shown in (h). Activation of SSFO switches rebound burst firing in the thalamus to tonic firing.

j) Quantification of 1-25 Hz broadband power 2 s before and after optogenetic manipulation. Data are from 32 trials across 4 mice. **** $p < 0.0001$ Mann-Whitney test.

k) Diagram of systemic administration of EBIO (s.c. 25 mg/kg).

l) Quantification of effects of systemic administration of EBIO on non-convulsive seizure frequency. Data are from n = 9 *Scn1a* DS mice. ** $p = 0.0012$ Mann-Whitney test.

m) Diagram of unilateral intra-nRT infusion of EBIO in conjunction with simultaneous multiunit recordings.

n) Quantification of effects of intra-nRT administration of EBIO (800 nl of 0.4 mM) on non-convulsive seizure frequency. Data are from n = 2 *Scn1a* DS mice.

Abbreviations: EEG, electroencephalogram; S1, somatosensory cortex; V1, visual cortex; ECoG, electrocorticogram; Thal., thalamus; Ipsi., ipsilateral; Contra., contralateral; MUA, multiunit activity; VB, ventral basal thalamus; nRT, thalamic reticular nucleus; SSFO, Stable Step-Function Opsin.

Supplemental Figures

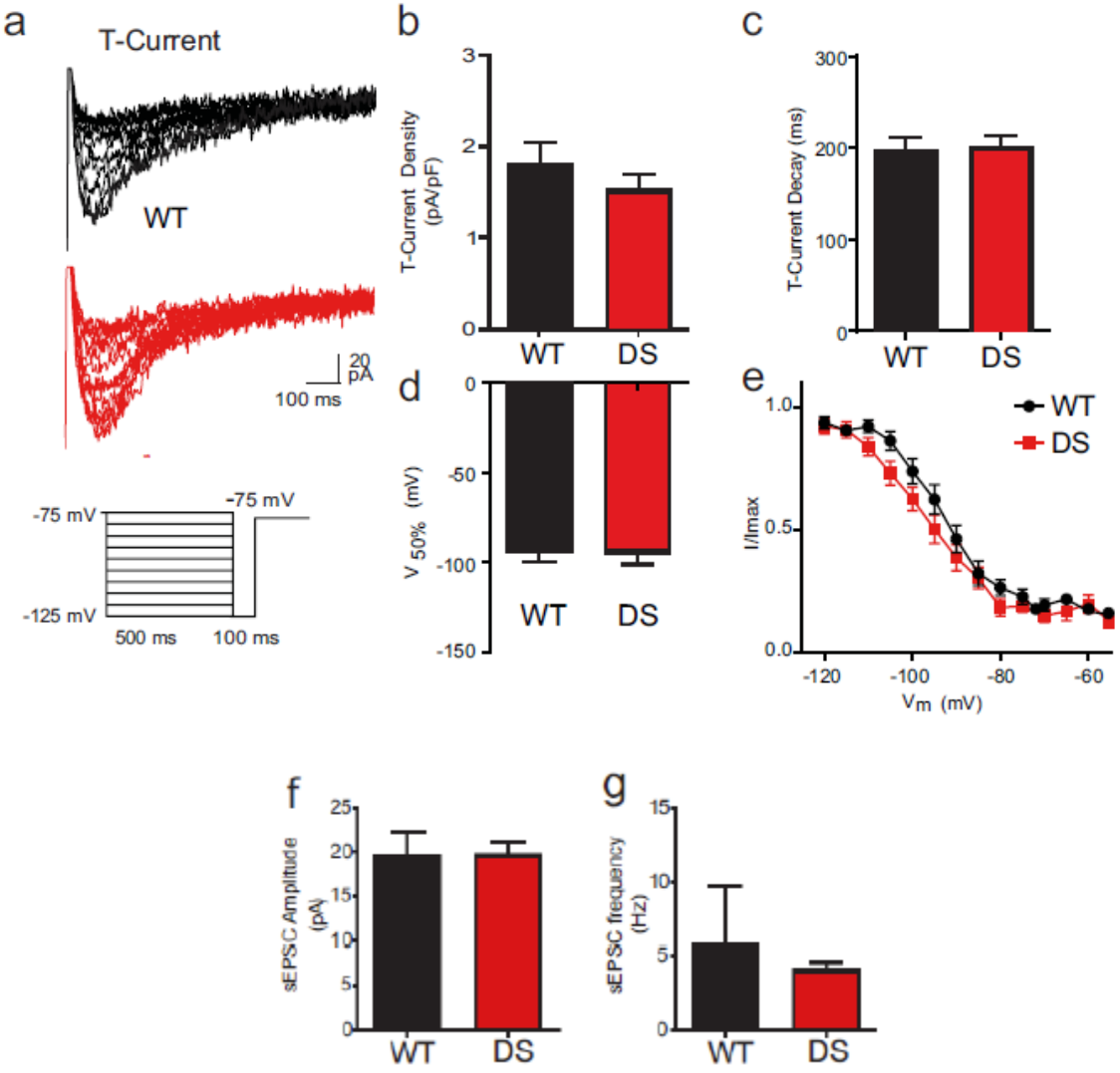

Figure 3.5. T-type Calcium current is similar in nRT neurons from Scn1a DS mice and WT littermates.

a) Representative traces showing T-type calcium current for cells from *Scn1a* DS animals and WT littermates (*Scn1a* DS: n = 26 neurons, 6 mice; WT littermates: n = 14 neurons, 4 mice).

b) T-type current density, the maximal amplitude divided by the individual cell capacitance.

c) T-current decay time constant.

d) Half-maximal voltage (*V50%*) taken from Boltzmann function.

e) Normalized current amplitude plotted as a function of the pre-pulse membrane potential best-fitted with a Boltzmann function (R^2 = 0.99 for both fits) (*Scn1a* DS: n = 16 cells, 6 mice; WT littermates: n = 13 cells, 4 mice).

f) Average amplitude and

g) Frequency of spontaneous excitatory postsynaptic current (sEPSCs). (*Scn1a* DS: n = 11 neurons, 2 mice; WT littermates: n = 6 neurons, 2 mice). Data represented as mean±SEM, compared using a Mann-Whitney test, with α=0.05. ns, non-significant, $p>0.05$.

Abbreviations: WT, wild-type; DS, Dravet syndrome; Vm, membrane voltage; sEPSC, spontaneous excitatory post synaptic currents

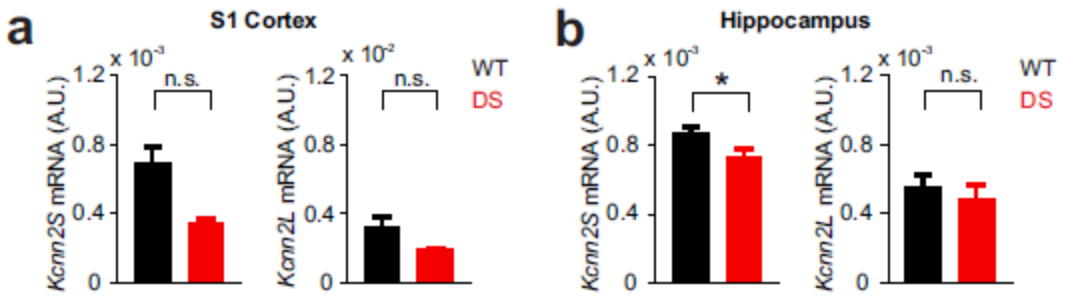

Figure 3.6. Reduction in SK2 expression is restricted to nRT.

a-b) Quantification of SK2 relative mRNA expression levels (encoded by the gene *Kcnn2*, short and long transcript variants) normalized to Gapdh mRNA in S1 cortex (a) and hippocampus (b). Expression levels were calculated using the $\Delta\Delta C_T$ method and are expressed as arbitrary units. Data are from n = 10 - 11 mice (WT) and n = 5 mice (DS). Data represented as mean±SEM, compared using a Mann-Whitney test, * $p < 0.05$, n.s., not significant.

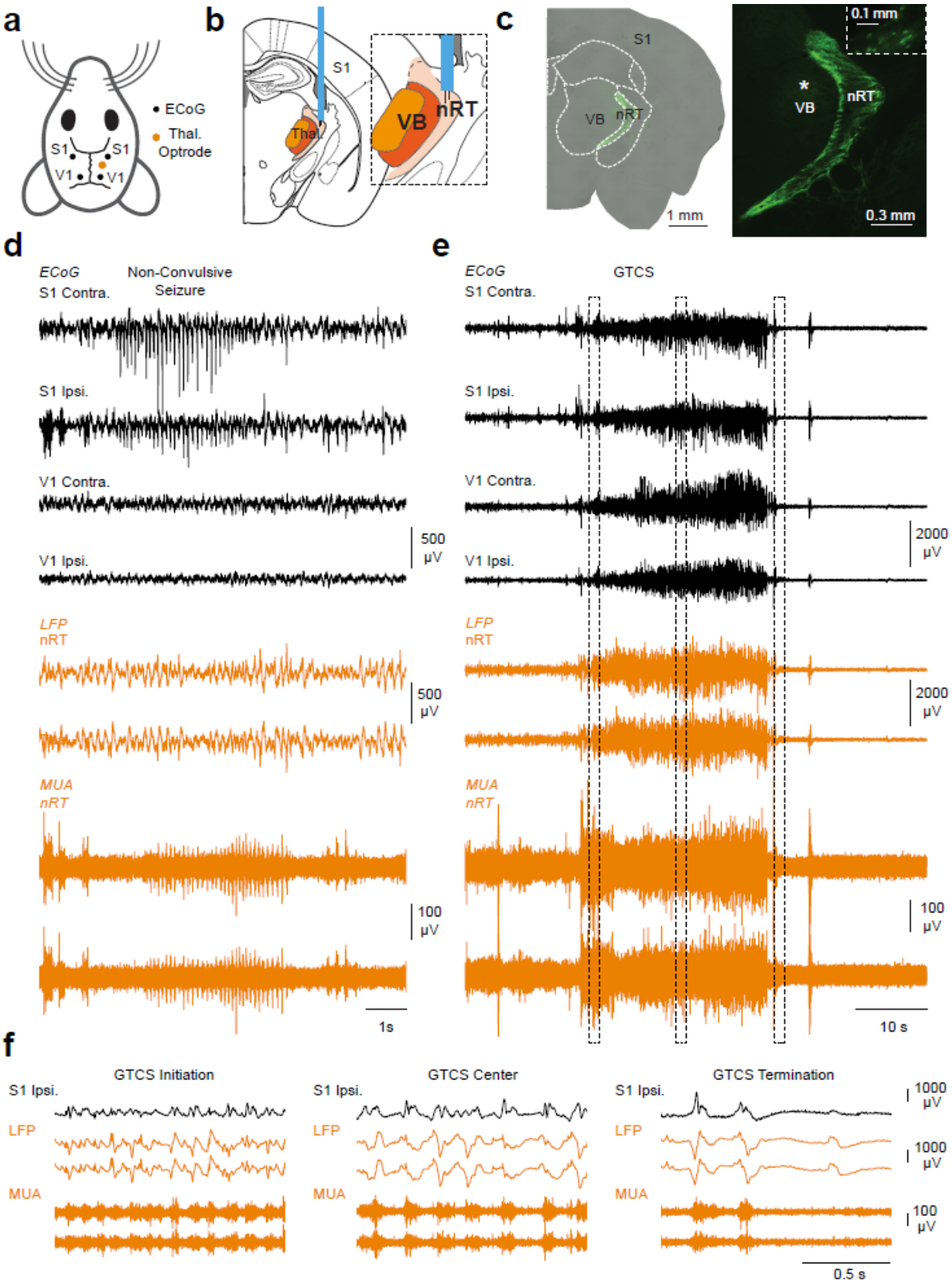

Figure 3.7. nRT bursts during seizures in Scn1a DS mice.

a) Diagram of the mouse ECoG and thalamic depth electrode recording montage. ECoG was recorded from S1 and V1 cortex, with depth electrodes implanted in the thalamus.

b) Positioning of implanted electrodes in a coronal slice. *Inset*, depth electrodes for MUA and LFP were implanted in nRT.

c) Representative example of viral spread of AAVs expressing channelrhodopsin in nRT from *Scn1a* DS Pv-Cre mice. Asterisk denotes minimal expression of virus in parvalbumin-positive VPM/VPL neurons.

d) Example of an ECoG signature of a typical non-convulsive seizure in *Scn1a* DS mice recorded from somatosensory cortex and visual cortex (black), along with simultaneous LFP and MUA recordings in nRT (orange). Note nRT bursts in phase with ECoG spikes during the non-convulsive seizure.

e) Example of an ECoG signature during an evoked hyperthermia-triggered GTCS in *Scn1a* DS mice recorded from somatosensory cortex and visual cortex (black), along with simultaneous LFP and MUA recordings in nRT (orange).

f) Zooms from insets shown in panel (e) showing that nRT bursts throughout different phases of the complex GTCS (*left, middle* panels) and that nRT does not burst during GTCS termination (*right* panel).

Abbreviations: S1, somatosensory cortex; V1, visual cortex; ECoG, electrocorticogram; Thal., thalamus; VB, ventral basal thalamus; nRT, thalamic reticular nucleus; Ipsi., ipsilateral; Contra., contralateral; LFP, local field potential; MUA, multiunit activity.

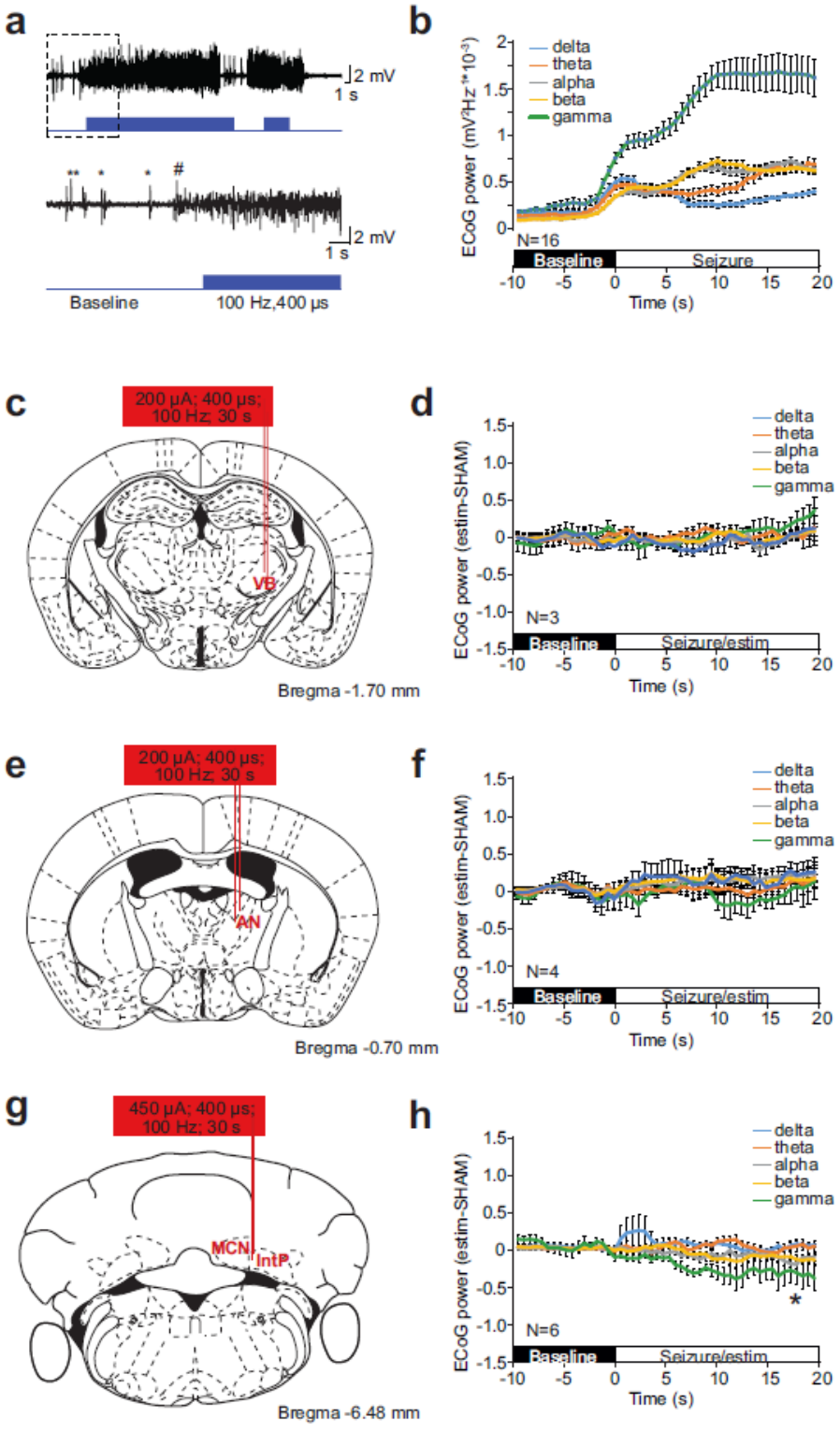

Figure 3.8. Hyperthermia-triggered GTCS cannot be halted by cerebellar or thalamic stimulation.

a) ECoG recorded from S1 electrodes in a freely moving mouse indicates the clear onset of seizure-related activity. Manual electrical stimulation (in this case sham is shown) was triggered after GTCS onset (pound sign). Asterisks indicate myoclonic jerks that precede seizure onset.

b) Using a line length algorithm we determined the onset of the seizures and aligned the recordings of GTCS seizures from 16 mice. Note the steep increase in ECoG power at the gamma band (30-100 Hz) upon seizure onset.

c) Schematic representation of stimulus electrode location in the ventral basal nucleus of the thalamus (VB).

d) Difference in ECoG power at various frequency band between electrical stimulation (estim) and sham stimulation experiments. No consistent effect was observed (Wilcoxon-Signed Rank Test, n = 3 mice, all bands n.s.).

e-h) Similar to (c,d) but for AN and CN stimulation experiments, respectively. Note, * in (h) corresponds to $p = 0.046$ for significant reduction in gamma power between 5 s of seizure (sham) versus 5 s of stimulation (estim) using a Wilcoxon-Signed Rank Test (AN, n = 4 DS mice, all bands n.s.; CN n = 6 DS mice, all bands except gamma n.s.).

Stereotactic atlas panels were adapted from Paxinos atlas for mouse brain (3rd edition). Error bars indicate SEM.

Abbreviations: ECoG, electrocorticogram; S1, somatosensory cortex; GTCS, generalized tonic-clonic seizure; VB, ventral basal thalamus; AN, anterior nuclei of the thalamus; CN; cerebellar nuclei; MCN; medial cerebellar nucleus; IntP, interposed cerebellar nucleus.

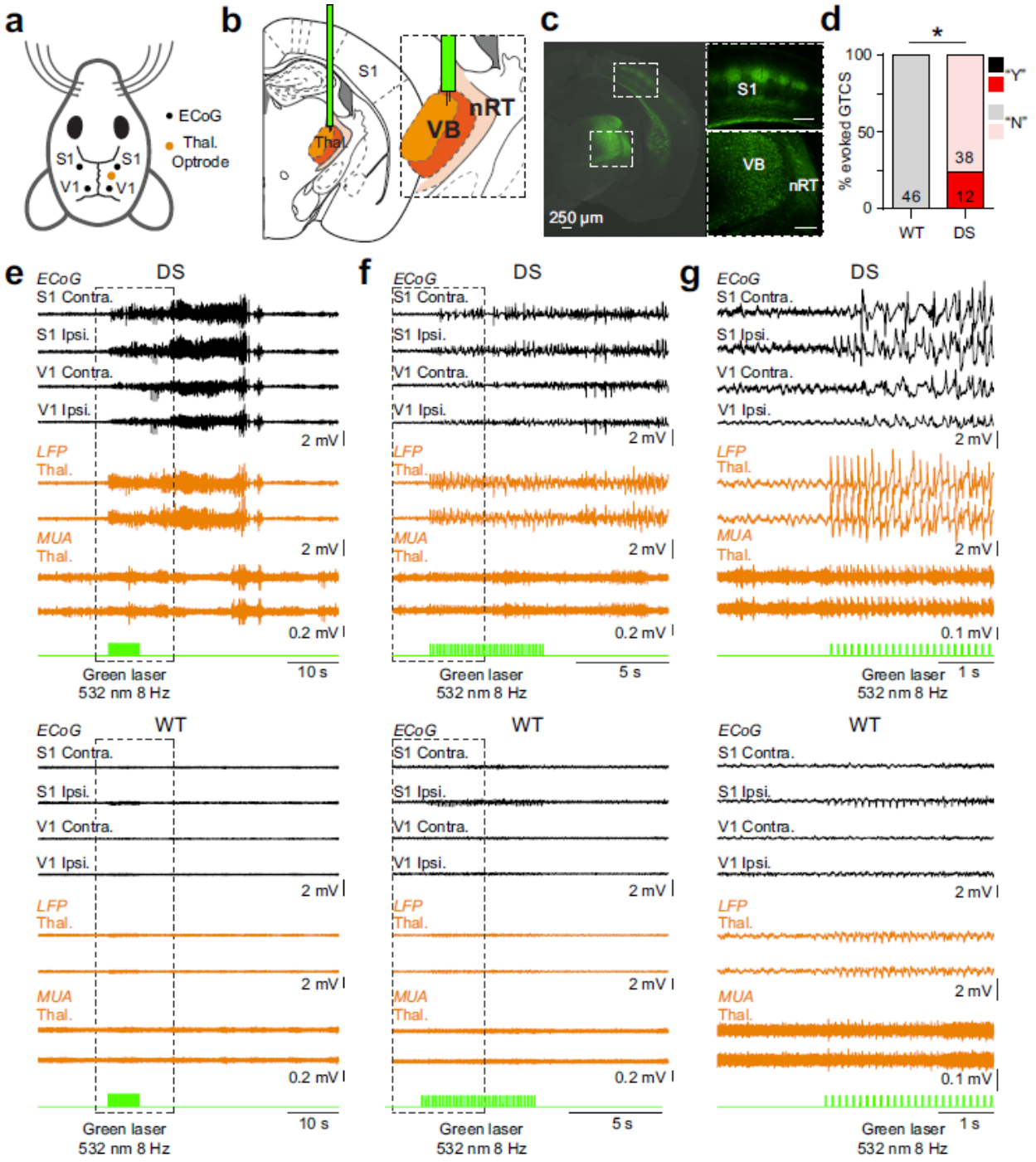

Figure 3.9. Optogenetically driving unilateral rhythmic bursting in the thalamus evokes generalized tonic-clonic seizures in Scn1a DS mice.

a) Diagram of the mouse ECoG and thalamic depth electrode recording montage. ECoG was recorded from S1 and V1 cortex, with depth electrodes implanted in the thalamus.

b) Positioning of implanted electrodes in a coronal section. *Inset*, depth electrodes for MUA and LFP were implanted in VB.

c) Representative example of viral spread of AAVs expressing halorhodopsin in VB (*inset*, bottom right) and labeling of thalamocortical fibers projecting onto S1 (*inset*, top right). Note, AAV expressing eYFP alone was used to demonstrate specificity of thalamic targeting and projections onto the cortex. Scale bar, 250 μm.

d) Percent of trials in which unilateral optogenetic stimulation of VB evoked GTCS activity in WT and DS mice (successful "Y" (black/red); unsuccessful "N" (grey, pink)). Data are from n = 3 DS and n = 5 WT mice; trial numbers are listed on the histograms. * $p < 0.05$, Fisher exact test statistic is 0.000257.

e) Representative example of ECoG and thalamic LFP/MUA from a DS (top) or WT (bottom) during unilateral optogenetic manipulation of VB. Green light (532 nm, 20 - 35 mW of power) was delivered into VB (25 ms pulse duration, 8 Hz, 50 pulses) to activate halorhodopsin and drive rebound bursting in the thalamus. This stimulation evoked GTCS in DS but not WT mice.

f) Zoom from area selected in (e) showing that evoked GTCS activity in DS mice (top) outlasted the pulse train, whereas evoked activity in WT mice (bottom) did not continue after the stimulation train ended. Note the thalamus continues to burst throughout the GTCS and is often in phase with cortical spikes.

g) Zoom from area selected in (f) showing that activation of halorhodopsin evoked rebound bursting in both DS (top) and WT (bottom) mice. Note, the seizure initiated in the cortex ipsilateral to the optogenetic stimulation.

Abbreviations: ECoG, electrocorticogram; Thal., thalamus; S1, somatosensory cortex; V1, visual cortex; VB, ventral basal thalamus; nRT, thalamic reticular nucleus; GTCS, generalized tonic-clonic seizure;

WT, wild-type mice; DS, *Scn1a* Dravet syndrome mice; Ipsi., ipsilateral; Contra., contralateral; LFP, local field potential; MUA, multiunit activity.

Table 3.1. Passive and active electric membrane properties of nRT cells from *SCN1A* DS mice and WT littermates

	Passive Properties			
Summary Table	**Cm (pF)**	**Vm (mV)**	**Rin (MΩ)**	**tau (ms)**
WT (n=21)	63.09 ± 4.61	-73.67 ± 1.61	354.23 ± 27.38	33.56 ± 2.96
DS (n=20)	51.75 ± 4.14	-71.60 ± 1.68	505.14 ± 46.36	38.49 ± 3.75
Significance	ns	ns	p<0.05	ns

	Action Potential Properties			
Summary Table	**Threshold (mV)**	**Amplitude (mV)**	**Half-Duration (ms)**	**Full-Duration (ms)**
WT (n=21)	-52.90 ± 1.01	45.15 ± 1.27	0.61 ± 0.02	1.36 ± 0.06
DS (n=20)	-49.41 ± 1.13	44.65 ± 1.91	0.77 ± 0.05	1.65 ± 0.09
Significance	p<0.05	ns	p<0.001	p<0.005

Data represented as mean±SEM, compared using a Mann-Whitney test, with α=0.05. ns, non significant, p>0.05.

Chapter 4 : Concluding Remarks

"Every illness is not a set of pathologies but a personal story"

- The Spirit Catches You and You Fall Down; Anne Fadiman

"There is whatever it is you're calling to. There is however it is you call."

- Grand Mal Seizure; The Virginia State Colony for Epileptics and Feebleminded: Poems, Molly McCully Brown

The work presented here looks to shed light on the roles of the *nucleus Reticularis Thalami* (nRT). My original interest in studying the nRT stems from its unique position as guardian of the gateway to higher processing, and in a sense, what makes us uniquely human. If we were to understand just even a little more about its unique properties and functions, we can come one incremental step closer to understanding how the brain works. Both of the quotes presented encompass my guiding principles for my graduate work: what are the functional pieces of the nRT that can be varied in each individual so that it changes the way we call to whatever it is we're calling to.

To understand the roles of the nRT, we have looked to dissect it in different planes: 1. By studying the properties of the neurons that make up the nRT, as done in Chapter 2, 2. By studying changes seen in nRT activity under pathological conditions, as done in Chapter 3. The experimental and interpretational caveats of the work presented here were discussed more at length in the Discussion sections of both Chapter 2 and Chapter 3. In this chapter, I will discuss general conclusions, future work, as well as unifying themes for these studies.

In Chapter 2, we discussed how the nRT can be divided into PV-expressing and SOM-expressing neurons. We found that PV-expressing neurons have a bursting phenotype and anatomical connections within the somatosensory circuit that enable them to modulate somatosensory behavior as well as seizure activity. We discovered that SOM-expressing cells have diminished bursting capabilities and form a

previously undescribed subcortical limbic-loop. Our assays showed that SOM-expressing neurons could increase ongoing seizure activity, but were unable to alter somatosensory behavior. The hope is that this work provides a strategy to selectively probe different functions of the nRT: those associated with epilepsy, somatosensation, and limbic behaviors. A major question that remains to be answered is how nRT cells interact with each other and what the implications of such feed-forward inhibition could be in the corticothalamic circuit. The existence on intra-nRT connections has been heavily debated and is highly controversial (Hou et al., 2016; Huntsman et al., 1999; Reinhold et al., 2015; Sohal et al., 2000). Our presynaptic rabies study suggests that these connections do indeed exist, and that SOM-expressing neurons might be the class that is most heavily connected. There is still much anatomical, physiological, and functional work to determine the existence of these connections, what rules they are governed by, and what are their implications. It is possible to hypothesize that the nRT is the anatomical location where sensation and emotion meet. This would further refine Crick's searchlight hypothesis (Crick, 1984). This hypothesis proposes that in the brain there exists this internal attentional searchlight and that there are physiological and anatomical reasons the nRT is primed to serve this role. The possibility of the nRT being able to concatenate internal emotional processing through limbic circuits, top-down cortical control, and bottom-up external sensory information on a cellular and synaptic level further supports this hypothesis. Much work is needed to make headway in answering this question.

In Chapter 3, we focus on the role of the nRT in a genetic epilepsy model. We have focused on studying the PV-expressing neurons, as it seems that the bursting phenotype is important in the modulation of seizure activity. We have found that in Dravets Syndrome (DS), this cellular bursting activity is hijacked through diminished expression and functional activity of the small conductance calcium activated potassium channel (SK). By increasing the activity of the SK channels present, we were able to restore the excessive bursting, which reduced the seizure activity. Future studies will investigate whether targeting SK channels can also treat the autism-type behavior in DS and prevent the sudden death which can occur in DS. In this study, we have not discussed what, if any, the role of SOM-expressing nRT neurons could be

in the development of DS. We know that the hippocampus, part of the limbic pathway thought not mono-synaptically connected to SOM-expressing nRT cells, is altered in DS and known to be involved in seizure generation (Liautard et al., 2013). We also know that SOM-expressing neurons are altered in other neuropsychiatric disorders, such as schizophrenia (Ahrens et al., 2015) and Attention Deficit and Hyperactivity Disorder (Wells et al., 2016). Are SOM-expressing cells involved in the development of epilepsy, the development of neuropsychiatric symptoms, neither or both?

By breaking something down into its component parts, we have a better understanding of how those parts usually work together. Knowing what these parts usually do gives us insight into what to target when what we are studying is not performing as it usually does.

References

Ahrens, S., Jaramillo, S., Yu, K., Ghosh, S., Hwang, G.-R., Paik, R., Lai, C., He, M., Huang, Z.J., and Li, B. (2015). ErbB4 regulation of a thalamic reticular nucleus circuit for sensory selection. Nat Neurosci *18*, 104–111.

Bouet, V., Boulouard, M., Toutain, J., Divoux, D., Bernaudin, M., Schumann-Bard, P., and Freret, T. (2009). The adhesive removal test: a sensitive method to assess sensorimotor deficits in mice. Nat Protoc. *4*, 1560–1564.

Crick, F. (1984). Function of the thalamic reticular complex: the searchlight hypothesis. Proc. Natl. Acad. Sci. *81*, 4586–4590.

Horikawa, K., and Armstrong, W.E. (1988). A versatile means of intracellular labeling: injection of biocytin and its detection with avidin conjugates. J. Neurosci. Methods *25*, 1–11.

Huntsman, M.M., Porcello, D.M., Homanics, G.E., DeLorey, T.M., and Huguenard, J.R. (1999). Reciprocal Inhibitory Connections and Network Synchrony in the Mammalian Thalamus. Science *283*, 541.

Liautard, C., Scalmani, P., Carriero, G., de Curtis, M., Franceschetti, S., and Mantegazza, M. (2013). Hippocampal hyperexcitability and specific epileptiform activity in a mouse model of Dravet syndrome. Epilepsia *54*, 1251–1261.

Mishra, A.M., Ellens, D.J., Schridde, U., Motelow, J.E., Purcaro, M.J., DeSalvo, M.N., Enev, M., Sanganahalli, B.G., Hyder, F., and Blumenfeld, H. (2011). Where fMRI and Electrophysiology Agree to Disagree: Corticothalamic and Striatal Activity Patterns in the WAG/Rij Rat. J. Neurosci. *31*, 15053–15064.

Paz, J.T., Bryant, A.S., Peng, K., Fenno, L., Yizhar, O., Frankel, W.N., Deisseroth, K., and Huguenard, J.R. (2011). A new mode of corticothalamic transmission revealed in the Gria4(-/-) model of absence epilepsy. Nat. Neurosci. *14*, 1167–1173.

Paz, J.T., Davidson, T., Freschette, E., Delord, B., Prada, I., Peng, K., Deisseroth, K., and Huguenard, J.R. (2013). Closed-loop optogenetic control of thalamus as a new tool to interrupt seizures after cortical injury. Nat. Neurosci. *16*, 64–70.

Reinhold, K., Lien, A.D., and Scanziani, M. (2015). Distinct recurrent versus afferent dynamics in cortical visual processing. Nat Neurosci *18*, 1789–1797.

Sohal, V.S., Huntsman, M.M., and Huguenard, J.R. (2000). Reciprocal Inhibitory Connections Regulate the Spatiotemporal Properties of Intrathalamic Oscillations. J. Neurosci. *20*, 1735.

Wells, M.F., Wimmer, R.D., Schmitt, L.I., Feng, G., and Halassa, M.M. (2016). Thalamic reticular impairment underlies attention deficit in Ptchd1Y/− mice. Nature *532*, 58–63.

Publishing Agreement

It is the policy of the University to encourage the distribution of all theses, dissertations, and manuscripts. Copies of all UCSF theses, dissertations, and manuscripts will be routed to the library via the Graduate Division. The library will make all theses, dissertations, and manuscripts accessible to the public and will preserve these to the best of their abilities, in perpetuity.

Please sign the following statement:

I hereby grant permission to the Graduate Division of the University of California, San Francisco to release copies of my thesis, dissertation, or manuscript to the Campus Library to provide access and preservation, in whole or in part, in perpetuity.

Author Signature

10/5/2017

Date